A STUDY OF SINGLE-LAP JOINTS

By

Matthew Paul Lempke

A THESIS

Submitted to
Michigan State University
in partial fulfillment of the requirements
for the degree of

Mechanical Engineering – Master of Science

2013

ABSTRACT

A STUDY OF SINGLE-LAP JOINTS

By

Matthew Paul Lempke

Single-lap joints are a widely-used and relatively strong and simple way joining two materials via an overlapping bond. With the growing use of composite materials in modern design practices, the need to join increasingly dissimilar materials has arisen. As such, knowledge concerning the behavior of single-lap joints with dissimilar adherends is essential.

To investigate the behavior of single-lap joints as material and geometric properties are varied under tensile loading, an analytically verified finite element parametric study was conducted on both ideally and adhesively bonded single-lap joints, measuring the changes in stress value at points of critical stress concentrations. In order to correlate the finite element analysis with real-world lap joint behavior, digital image correlation was used to record the deformation of lap joint specimens under a tensile load. A finite element model was then developed, and compared, to the experimental results.

With the results of the parametric study and experimental comparison, trends in stress changes were identified and explained, and design suggestions were made based on these trends. The results of the experimental finite element model were reasonably correlated, and several suggestions for improvements were made.

ACKNOWLEDGEMENTS

I would like to thank Dr. Dahsin Liu for allowing me the opportunity and guiding me through the research and thesis writing process. I would also like to thank the US Army Research Laboratory for funding this research, and Dr. Mahmood Haq and Dr. Xinran Xiao for serving on my thesis defense committee, and helping me finalize my thesis. Lastly, I would like to thank my uncle William Janis for always believing in me and making a college education possible, Alexis Palmquist, for always standing with me and being there whenever I needed her, and the rest of my friends and family for being the best support structure anyone could want.

TABLE OF CONTENTS

LIST OF TABLES v

LIST OF FIGURES vii

KEY TO SYMBOLS x

1 Introduction 1
REFERENCES 5

2 Brief Overview of the Single-lap Joint 7
REFERENCES 10

3 Theoretical Analysis 12
REFERENCES 18

4 Finite element analysis of the Single-Lap Joint 20
REFERENCES 35

5 Results of the FEA Based Parametric Study 37
5.1 Varied Adherend Thickness Under Ideal Bonding and a Tensile Load 37
5.2 Varied Adherend Thickness Under Ideal Bonding and a Tensile Load 43
5.3 Varied Free Adherend Length Under Ideal Bonding and a Tensile Load 47
5.4 Varied Bonding Length Under Ideal Bonding and a Tensile Load 51
5.5 Varied Young's Modulus Under Ideal Bonding and a Three-Point Bending Load 55
5.6 Varied Adherend Thickness Under Ideal Bonding and a Three-Point-Bending Load 59
5.7 Varied Free Adherend Length Under Ideal Bonding and a Three-Point-Bending Load 63
5.8 Varied Bonding Length Under Ideal Bonding and a Three-Point-Bending Load 66
5.9 Varied Adhesive Thickness Under Adhesive Bonding and a Tensile Load 69
5.10 Varied Young's Modulus Under Adhesive Bonding and a Tensile Load 73
5.11 Varied Adherend Thickness Under Adhesive Bonding and a Tensile Load 78
5.12 Varied Adhesive Young's Modulus Under Adhesive Bonding and a Tensile Load 81
5.13 Design Recommendations via Parametric Study 84

6 Experimental Validation 86
REFERENCES 101

7 Conclusions 103

8 Suggestions for Future Research 107

LIST OF TABLES

Table 4.1 Tensile basic case stress values at points *A* and *B*...................................... 25

Table 4.2 Tensile basic case stress values at points *A* and *B*...................................... 30

Table 5.1 Reference stress values and SCFs at point *A* with varying E/E_0............... 38

Table 5.2 Reference stress values and SCFs at point *B* with varying E/E_0............... 38

Table 5.3 Reference stress values and SCFs at point *A* with varying t/t_0.................. 43

Table 5.4 Reference stress values and SCFs at point *B* with varying t/t_0.................. 44

Table 5.5 Reference stress values and SCFs at point *A* with varying L/L_0 47

Table 5.6 Reference stress values and SCFs at point *B* with varying L/L_0 48

Table 5.7 Reference stress values and SCFs at point *A* with varying c/c_0................. 51

Table 5.8 Reference stress values and SCFs at point *B* with varying c/c_0................. 52

Table 5.9 Reference stress values and SCFs at point *A* with varying E/E_0............... 55

Table 5.10 Reference stress values and SCFs at point *B* with varying E/E_0............. 56

Table 5.11 Reference stress values and SCFs at point *A* with varying t/t_0................ 59

Table 5.12 Reference stress values and SCFs at point *B* with varying t/t_0................ 60

Table 5.13 Reference stress values and SCFs at point *A* with varying L/L_0 63

Table 5.14 Reference stress values and SCFs at point *B* with varying L/L_0 64

Table 5.15 Reference stress values and SCFs at point *A* with varying c/c_0 66

Table 5.16 Reference stress values and SCFs at point *B* with varying c/c_0 67

Table 5.17 Stress values and SCFs as η/η_0 varies at point A_1 70

Table 5.18 Stress values and SCFs as η/η_0 varies at point B_2 70

Table 5.19 Stress values of the basic model without any adhesive 73

Table 5.20 Stress values of the basic model with adhesive, SCFs compared to table 1 74

Table 5.21 Stresses and SCFS at point A_1 as E/E_0 varies 75

Table 5.22 Stresses and SCFS at point B_2 as E/E_0 varies 75

Table 5.23 Stresses and SCFS at point A_1 as t/t_0 varies 78

Table 5.24 Stresses and SCFS at point B_2 as t/t_0 varies 78

Table 5.25 Stresses and SCFS at point A_1 as E_c/E_{c0} varies 81

Table 5.26 Stresses and SCFS at point B_2 as E_c/E_{c0} varies 81

Table 6.1 Dimensions of specimen 1 88

Table 6.2 Dimensions of specimen 2 89

Table 6.3 Comparison of displacements for specimen 1 91

Table 6.4 Comparison of displacements for specimen 2 92

Table 6.5 Failure stress predictions for specimen 1 100

Table 6.6 Failure stress predictions for specimen 2 100

LIST OF FIGURES

Figure 2.1 A single-lap joint 7

Figure 2.2 A double-lap joint 8

Figure 2.3 A step-lap joint 8

Figure 3.1 Analytical solution geometry and boundary conditions 13

Figure 3.2 Analytical solution 15

Figure 3.3 Analytical solution and FE solution 17

Figure 4.1 Analytical solution and FE solution 22

Figure 4.2 Finite element boundary conditions in tension 23

Figure 4.3 Finite element boundary conditions in three point bending 23

Figure 4.4 Von-Mises stress contour map under unit tensile loading 26

Figure 4.5 X direction stress contour map under unit tensile loading 27

Figure 4.6 Y direction stress contour map under unit tensile loading 28

Figure 4.7 XY shear stress contour map under unit tensile loading 29

Figure 4.8 Von-Mises stress contour map under three point bending load 31

Figure 4.9 X direction stress contour map under three point bending load 32

Figure 4.10 Y direction stress contour map under three point bending load 33

Figure 4.11 XY shear stress contour map under three point bending load 34

Figure 5.1 Ideally bonded Young's Modulus variation critical points 38

Figure 5.2 SCFs as E/E_0 varies at point A 39

Figure 5.3 SCFs as E/E_0 varies at point B 40

Figure 5.4 Ideally bonded thickness variation critical points 43

Figure 5.5 SCFs as t/t_0 varies at point *A* 44

Figure 5.6 SCFs as t/t_0 varies at point *B* 45

Figure 5.7 Ideally bonded free adherend length variation critical points 47

Figure 5.8 SCFs as L/L_0 varies at point *A* 48

Figure 5.9 SCFs as L/L_0 varies at point *B* 49

Figure 5.10 Ideally bonded bonding length variation critical points 51

Figure 5.11 SCFs as c/c_0 varies at point *A* 52

Figure 5.12 SCFs as c/c_0 varies at point *B* 53

Figure 5.13 Ideally bonded Young's Modulus variation critical points 55

Figure 5.14 SCFs as E/E_0 varies at point *A* 56

Figure 5.15 SCFs as E/E_0 varies at point *B* 57

Figure 5.16 Ideally bonded thickness variation critical points 59

Figure 5.17 SCFs as t/t_0 varies at point *A* 60

Figure 5.18 SCFs as t/t_0 varies at point *B* 61

Figure 5.19 Ideally bonded free adherend length variation critical points 63

Figure 5.20 SCFs as L/L_0 varies at point *A* 64

Figure 5.21 SCFs as L/L_0 varies at point *B* 65

Figure 5.22 Ideally bonded bonding length variation critical points 66

Figure 5.23 SCFs as c/c_0 varies at point *A* 67

Figure 5.24 SCFs as c/c_0 varies at point *B* 68

Figure 5.25 Finite element boundary conditions and parameters 69

Figure 5.26 Adhesively bonded adhesive thickness variation critical points 70

Figure 5.27 SCFs as η/η_0 varies at point A_1 71

Figure 5.28 SCFs as η/η_0 varies at point B_2 72

Figure 5.29 Adhesively bonded Young's Modulus variation critical points 74

Figure 5.30 SCF at point A_1 as E/E_0 varies 76

Figure 5.31 SCF at point B_2 as E/E_0 varies 77

Figure 5.32 Adhesively bonded adherend thickness variation critical points 78

Figure 5.33 SCF at point A_1 as t/t_0 varies 79

Figure 5.34 SCF at point B_2 as t/t_0 varies 80

Figure 5.35 Adhesively bonded adhesive Young's Modulus variation critical points 81

Figure 5.36 SCF at point A_1 as E_c/E_{c0} varies 82

Figure 5.37 SCF at point B_2 as E_c/E_{c0} varies 83

Figure 6.1 Diagram of the dimensions and shapes of the experimental specimens .. 87

Figure 6.2 Finite element (left) and DIC (right) displacement magnitude specimen 1 92

Figure 6.3 Finite element (left) and DIC (right) X direction displacement specimen 1 93

Figure 6.4 Finite element (left) and DIC (right) Y direction displacement specimen 1 94

Figure 6.5 Finite element (left) and DIC (right) displacement magnitude specimen 2 96

Figure 6.6 Finite element (left) and DIC (right) X direction displacement specimen 2 97

Figure 6.7 Finite element (left) and DIC (right) Y direction displacement specimen 2 98

KEY TO SYMBOLS

c	Half bonding length
c_0	Half base bonding length
E	Adherend Young's Modulus
E_0	Base Young's Modulus
E_c	Adhesive Young's Modulus
E_{c0}	Base adhesive Young's Modulus
k	Edge moment factor
L	Free adherend length
L_0	Base free adherend length
M_0	Edge moment
P	Applied three-point bending load
T	Applied tensile load
t	Adherend thickness
t_0	Base adherend thickness
w_1	Adherend transverse axis
w_2	Adhesive transverse axis
x_1	Adherend normal axis
x_2	Adhesive normal axis
α_n	Eccentric loading angle
η	Adhesive thickness
σ_0	Applied tensile pressure

σ_{vm}	Von-Mises stress
σ_{xx}	X direction stress
σ_{yy}	Y direction stress
τ_{xy}	Shear stress
v	Adherend Poisson's Ratio
v_c	Adhesive Poisson's Ratio

1 Introduction

As composite materials become more prevalent in modern design, many situations arise in which they are needed in conjunction with traditional homogeneous materials. Namely, in vehicles and many other applications, metal to composite joining is necessary to increase the strength to weight ratio in modern structures. However, some difficulties arise in the joining of these dissimilar materials. Where one could presumably weld two metals together, or mix ceramic powders into the complicated shape desired, one cannot join polymeric composites to metal in such a strong manner. Other methods of joining are possible, such as mechanical fastening, or adhesive joining. The focus of this thesis is to investigate how the variation of dominant joint material and geometric parameters independently affect the critical stresses in adhesive single-lap joints as predicted by finite element analysis, and verify this analysis both analytically and experimentally.

Lap joints, specifically the adhesive single-lap joint, have been studied thoroughly throughout the years. Analytic solutions date back as far as Volkerson [1] and his simplified solution in 1938 that is still more accurate than the current ASTM standards D1002-10 and D3983-98 used to determine shear strength and shear modulus, respectively. Goland and Reissner [2] built upon his solution, adding the influence of the eccentric loading angle and thus introducing the important influence of the edge moment by adding the bending moment factor, k. This factor is related to the bending moment M_0, the adherend thickness t, and the load applied to the adherends T by equation 1.1.

$$k = \frac{2M_0}{Tt} \tag{1.1}$$

This bending moment factor is unity for small loadings for which no rotation of the joint itself results, and less than unity for higher loads. They found that maximum stresses occur at the ends of the overlap, which is to be expected. However, according to Adams [3], Goland and Reissner's solution is not applicable to most practical joints, or joints including adherends of differing materials, as they neglect adherend shear strains He found that a geometrically non-linear finite element analysis is applicable to a wider range of lap joints. Tsai and Morton [4] performed an in depth comparison of the available analytic solutions in 1992, and found Hart-Smith's [5] model the most accurate for determining the edge moment in short joints, and Oplinger's [6] model the most valid for determining the edge moment in long joints. Goland and Reissner's solution predicted a global sense of the adhesive stress distributions for both lengths most effectively, and was altogether more accurate than the other solutions for adherends of intermediate length. Tsai and Morton [4] defined long lap joints as those with a free adherend length to bonding length ratio of greater than 5 and short joints as those with a ratio of less than 0.75. They also found that geometrically non-linear finite element analysis was still the most effective and accurate method of single-lap joint modeling.

Carpenter [7] explored the effects of various mathematical assumptions on the adhesive stresses in single-lap joints, and found the predicted maximum adhesive shear and peel stresses were mostly unaffected by most assumptions, but neglecting shear deformation of the adherends affects peel stress significantly. He again found that finite element methods yield results very close to those from lap joint theories such as Goland and Reissner [2] and Delale and Erdogan [13]. Cooper and Sawyer [8] further explored finite element analysis, comparing geometrically linear results to non-linear results. The results were then compared to Goland and Reissner's analytical solution and photoelastic experiments, and it was shown that the geometrically non-linear Finite Element Analysis was accurate, and the non-linearity had a large effect on the stresses in the adhesive. Goland and Reissner's solution was found to be sufficient for the prediction of stresses along the midline of the adhesive bond.

Lap joints have also been thoroughly experimentally and numerically analyzed in a variety of forms and methods. Crocombe and Adams [9] explored the influence of a spew fillet on the stress distributions in a single-lap joint, and found that maximum adhesive stresses are usually much lower with the addition of the spew fillet rather than a square termination of the adhesive. Spew fillets are triangular adhesive fillets at the termination of the bond. More recently, Shin, Lee, and Lee [10] studied shear strength of co-cured single-lap joints subjected to tensile loads, and found that in most cases, the failure mechanism was partially cohesive failure, and the shear strength is significantly impacted by bond length and stacking sequence. Elaborating, the stacking sequence of the composite adherend greatly affects the shear strength of the joint due to the fact that the stacking sequence determines the difference in stiffness between adherends. Also, as bond length increases, so does the shear strength of the lap joint. Maglahaes, de Moura, and Gonclaves [11] explored the stress concentration effects in laminate composite single-lap joints through two-dimensional Finite Element Analysis, and found critical stress locations near the ends of the overlap and discussed their role in damage initiation in composite lap joints. Grant, Adams, and de Silva [12] investigated experimental and numerical analysis of single-lap joints for the automotive industry, including tension, four-point, and three-point bending tests varying other parameters as well. They found three-point bending and tension tests yielded similar results in the adhesive, as they both induce a large bending moment and both initiate failure in the adhesive, while four-point bending did not cause any adhesive failure. The adherend material (steel) yielded before the adhesive, and they proposed a failure criterion.

This work will first define lap joints and present an overview of several of the various lap joint geometries. Analytical derivation and verification is then presented, followed by a description and in-depth example of the parametric study conducted. The results are then presented, and discussed, followed by experimental work and validation, and both a conclusions and suggestions section.

REFERENCES

REFERENCES

[1] Volkerson, O. “Die Niektraftverteiling in Zugbeanspruchten mit Konstanten Laschquershritten.” *Luftfahrforschung.* 48. (1938)

[2] Goland, M., Reissner, E. “The stresses in cemented joints.” *J. Appl. Mech.* 11. (1944)

[3] Adams, R. D. “Strength Predictions for Lap Joints, Especially with Composite Adherends. A Review.” *J. of Adhesion.* 30. (1989)

[4] Tsai, M. Y., Morton, J. “An Evaluation of Analytical and Numerical Solutions to the Single-Lap Joint.” *Int. J. Solids Structures.* 31. (1994)

[5] Hart–Smith, L. J. “Adhesive-bonded single-lap joints.” *NASA.* CR-112236. (1973)

[6] Oplinger, D. W. “A layered beam theory for single lap joints.” *Army Materials Technology Laboratory Report*. MTL TR91-23. (1991)

[7] Carpenter, W. “A comparison of numerous lap joint theories for adhesively bonded joints” *J. of Adhesion.* 35. (1991)

[8] Cooper, P. A., Sawyer, J. W. “A Critical Examination of Stresses in an Elastic Single Lap Joint.” *NASA.* TR1507. (1979)

[9] Crocombe, A. D., Adams, R. D. “Influence of the Spew Fillet and other Parameters on the Stress Distribution in the Single-Lap Joint.” *J. of Adhesion.* 13. (1981)

[10] Shin, K. C., Lee, J. J., Lee, D. G. “A study on the lap shear strength of a co-cured single lap joint.” *J. of Adhesion Science and Technology.* 14. (2012)

[11] Maglahaes, A. G., de Moura, M. F. S. F., Gonclaves, J. P. M. “Evaluation of stress concentration effects in single-lap bonded joints of laminate composite materials.” *International Journal of Adhesion and Adhesives*. 25. (2005)

[12] Grant, L. D. R., Adams, R. D., de Silva, L. F. M. “Experimental and numerical analysis of single-lap joints for the automotive industry.” *International Journal of Adhesion and Adhesive.* 29. (2009)

[13] F. Delale, F. Erdogan. “Stresses in Adhesively Bonded Joints: A Closed-Form Solution.” *Journal of Composite Materials*. 15. (1981)

2 Brief Overview of the Single-lap Joint

A full single-lap joint is simply an anti-symmetric structure of two materials, known as adherends, bonded via an overlap, usually with adhesive, bolts, or both, where no material is removed at the bond. In other words, a full lap is like Figure 2.1, a simple single-lap joint. There is a full overlap with no adherend material altered at the joint.

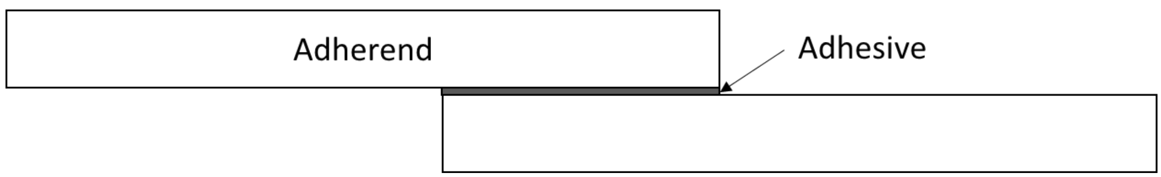

Figure 2.1 A single-lap joint

Half lap joints can have material removed at the bond for symmetry, or to keep the surface smooth and without overlap. Double-lap joints are a full lap joint that simply has an additional adherend, as illustrated in Figure 2.2. A step lap is a half lap joint with a step-like interface, shown in Figure 2.3. There are many types of lap joints, such as but in this thesis, only ideally bonded, a theoretical ideal in which no adhesive is used, and adhesively bonded single-lap joints with square adhesive termination are investigated. Square adhesive termination refers to the fact that there is no fillet at the edge of the adhesive. Fillets have been shown to increase failure stress in lap joints, as shown in the literature survey in chapter 1.

Figure 2.2 A double-lap joint

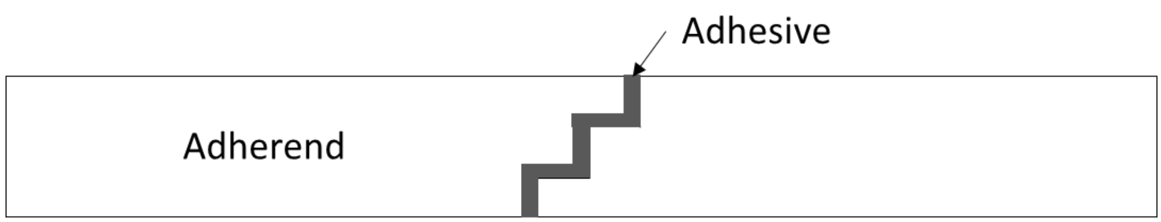

Figure 2.3 A step-lap joint

Several parameters influence the stress distributions and strength of single-lap joints. Important material properties include the various moduli and Poisson's Ratios of each adherend and the adhesive. Geometrically, both the free length and bond length of each adherend, their thickness and the thickness of the adhesive also impact the stress distributions and overall displacement of the structure. The effects of these parameters is investigated and explained in chapter 5.

Dissimilar joining, or joining two adherends of differing material property or geometry, is difficult. For instance, joining a composite adherend to a metal adherend presents several issues, as the adhesive may not bond to the dissimilar surfaces equally as well, and any holes drilled in the composite for mechanical fastening creates stress concentrations that may initiate damage in the composite due to its non-homogeneous Young's Modulus. The differing properties between the two materials could influence the stress distributions to be more intense than a homogeneous single-lap joint. Therefore, this thesis investigates the important parameters' impact on the critical stress points in the adherends of single-lap joints.

REFERENCES

REFERENCES

[1] Budynas, Richard G., and Nisbett, Kieth J. *Shigley's Mechanical Engineering Design*. 9th ed. New York: McGraw Hill, 2011. Print.

3 Theoretical Analysis

In order to confirm the validity and accuracy of the finite element analysis presented later in this work, it was necessary to explore analytical solutions for the displacements in a single lap joint. While several were presented, Goland and Reissner's [1] equations were found to be the most accurate for the parametric study conducted, and others, like Tsai and Morton [2], used this solution to validate their finite element analysis.

The several other solutions mentioned include Volkerson's [3] famous equation presented in 1938, which was an improvement on the ASTM standard for shear strength determination (ASTM D1002-10) and modulus determination (ASTM D3983-98) for adhesives, still used today. In Tsai and Morton's review, Volkerson's solution was found to be inferior to the other solutions reviewed, and the solution itself can be found in his publication. Goland and Reissner's [1] solution was the first to include the influence of the edge moment, the moment that arises at the edge of the overlap, which was an important step towards an accurate single lap joint model. Goland and Reissner found that this edge moment is the dominant factor in the stress development throughout the joint geometry, and its inclusion made their solution a leap ahead of Volkerson's. Hart-Smith [4] and Oplinger [5] also presented different models. Tsai and Morton found that Hart-Smith's model was the most accurate in predicting the stresses in short single-lap joints, while Oplinger's solution was found to be more accurate for long single-lap joints. Long and short joint cases are defined by Tsai and Morton as joints in which the ratio of l/c is greater than or equal to 10 or less than or equal to 1.25, respectfully. Joints falling between these bounds are considered adhesive joints of intermediate length. However, Goland and Reissner's solution was still found to be accurate in its prediction of deflection, and thus it is used for the validation of the following work.

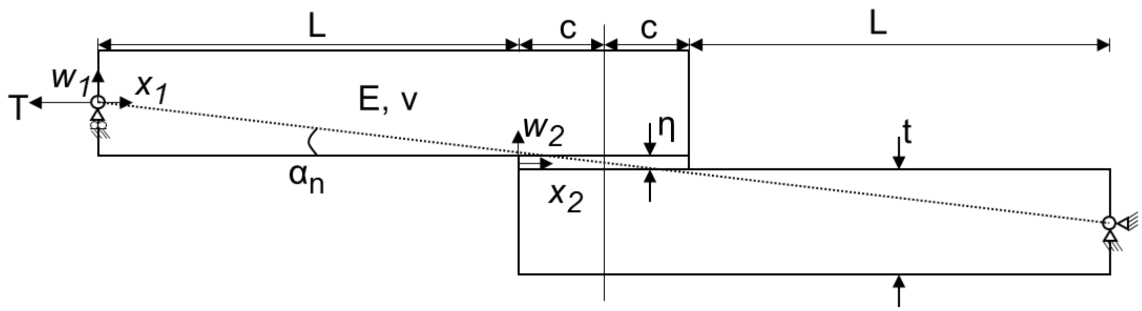

Figure 3.1 Analytical solution geometry and boundary conditions

With reference to Figure 3.1, x_1 being the region in the adherend bounded by zero and L, and x_2 being the region in the adhesive bounded by zero and $2c$, Goland and Reissner present the following general solution and boundary conditions:

$$\frac{d^2 w_1}{dx_1{}^2} + \frac{T}{D_1}\left[\alpha_n x_1 - w_1\right] = 0, \quad 0 \le x_1 \le L, \quad D_1 = \frac{Et^3}{12\left(1-\upsilon^2\right)} \tag{3.1}$$

$$\frac{d^2 w_2}{dx_2^2} + \frac{T}{D_2}\left[\alpha_n\left(L + x_2\right) - w_2 - \frac{t}{2}\right] = 0, \quad 0 \le x_2 \le 2c, \quad D_2 = \frac{2Et^3}{3\left(1-\upsilon^2\right)} \tag{3.2}$$

Subject to simple support external boundary conditions and the internal boundary conditions including the continuous displacements and rotation angles and zero displacement at the anti-symmetric point:

$$w_1(0) = 0, \quad w_2(c) = 0, \quad w_1(L) = w_2(0), \quad \frac{dw_1}{dx_1}(x_1 = L) = \frac{dw_2}{dx_2}\left(x_2 = 0\right) \tag{3.3}$$

The general solution to each equation is of the form:

$$w_1 = A_1 \cosh(u_1 x_1) + B_1 \sinh(u_1 x_1) + \alpha_n x_1, \quad 0 \le x_1 \le L \tag{3.4}$$

$$w_2 = A_2 \cosh(u_2 x_2) + B_2 \sinh(u_2 x_2) + \alpha_n \left(1 + x_2 - \frac{t}{2\alpha_n}\right), \quad 0 \le x_2 \le 2c \tag{3.5}$$

$$where\ u_1 = \sqrt{\frac{T}{D_1}}\ and\ u_2 = \sqrt{\frac{T}{D_2}} \tag{3.6}$$

Applying the boundary conditions and solving, the constants can then be found to be:

$$A_1 = 0 \tag{3.7}$$

$$B_1 = \frac{-u_2(u_1 \cosh(u_1 L)\sinh(u_2 c) + u_2 \cosh(u_2 c)\sinh(u_1 L))}{4\alpha_n(1+c) - 2t + \cosh(u_2 c)(2t + \alpha_n(4L-4))} \tag{3.8}$$

$$A_2 = \frac{u_1 \cosh(u_1 L)\sinh(u_2 c)\alpha_n\left(L - 1 + \frac{t}{2\alpha_n}\right) - \alpha_n u_2 \sinh(u_1 L)\left(c + 1 - \frac{t}{2\alpha_n}\right)}{u_1 \cosh(u_1 L)\sinh(u_2 c) + u_2 \cosh(u_2 c)\sinh(u_1 L)} \tag{3.9}$$

$$B_2 = \frac{-u_1 \cosh(u_1 L)\{\alpha_n(2+2c) + \cosh(u_2 c)[t + \alpha_n(2L-2)] - t\}}{2(u_1 \cosh(u_1 L)\sinh(u_2 c) + u_2 \cosh(u_2 c)\sinh(u_1 L))} \tag{3.10}$$

Due to homogeneity of materials and boundary conditions, one can plot the region from –*L* to *0*, and *0* to *2c*, obtaining the analytic solution plot in Figure 2, below.

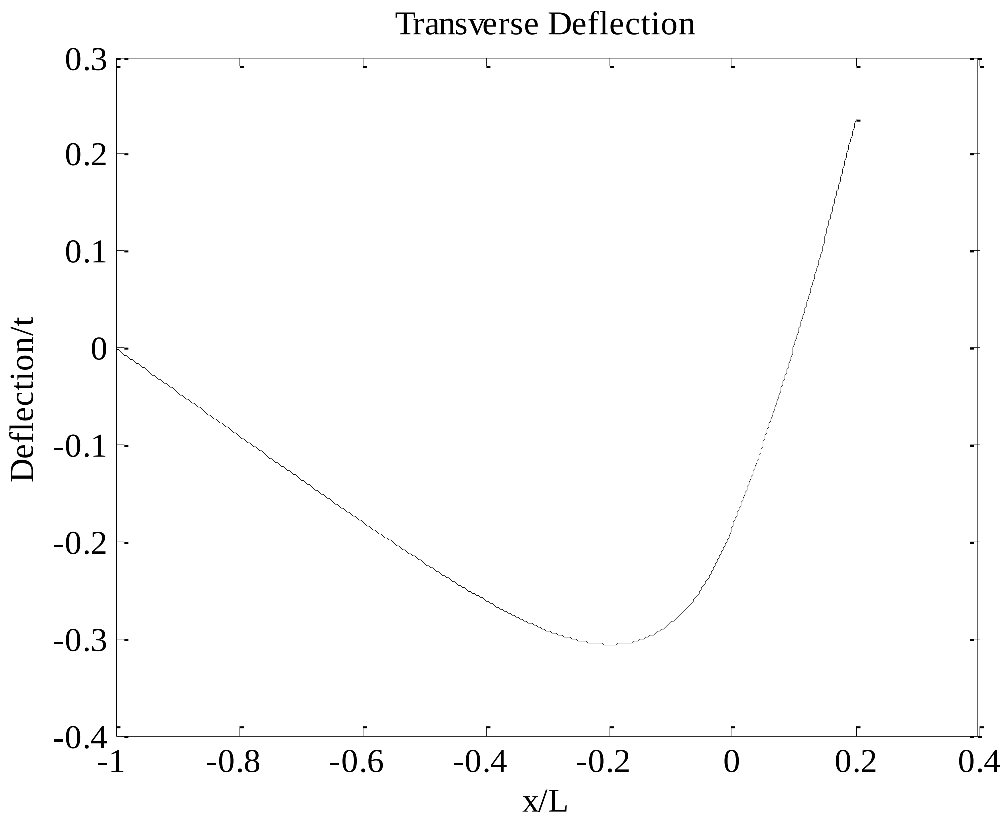

Figure 3.2 Analytical solution

Of particular note in this analysis is the eccentric angle of loading, α_n. Because of this, as loading increases, non-linear geometric effects occur. Therefore, any finite element analysis performed needs to include considerations for high nodal rotations and a sufficiently small (5-10% of the total simulation time) timestep.

Performing a geometrically non-linear finite element analysis with ABAQUS and constraining the adherends with the same boundary conditions as Goland and Reissner's problem statement for zero adhesive thickness, the appropriate displacements were obtained, and Figure 3.3 was plotted, which compares Figure 3.2 and the finite element transverse deflection results, measured along the centerline of the adherend as defined by the x_1, w_1 coordinate system, and the centerline of the adhesive as defined by the x_2, w_2 coordinate system. The finite element analysis was performed on a typical short joint as dictated by Tsai and Morton, and a load of T = 400 N was applied as shown in Figure 3.1. It is immediately obvious that ABAQUS accurately solves the model, with FE displacements extremely similar to analytical displacements, using an adequately fine mesh.

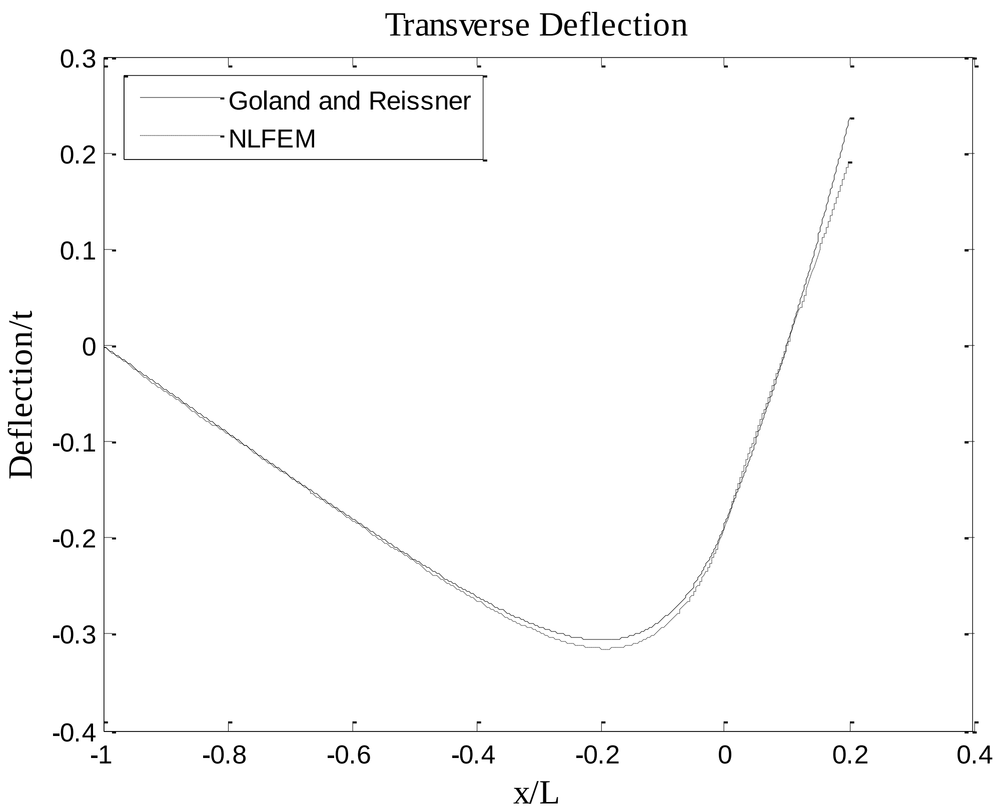

Figure 3.3 Analytical solution and FE solution

REFERENCES

REFERENCES

[1] Volkerson, O. “Die Niektraftverteiling in Zugbeanspruchten mit Konstanten Laschquershritten.” *Luftfahrforschung.* 48. (1938)

[2] Goland, M., Reissner, E. “The stresses in cemented joints.” *J. Appl. Mech.* 11. (1944)

[3] Tsai, M. Y., Morton, J. “An Evaluation of Analytical and Numerical Solutions to the Single-Lap Joint.” *Int. J. Solids Structures.* 31. (1994)

[4] Hart–Smith, L. J. “Adhesive-bonded single-lap joints.” *NASA*. CR-112236 (1973)

[5] Oplinger, D. W. “A layered beam theory for single lap joints.” *Army Materials Technology Laboratory Report.* MTL TR91-23. (1991)

4 Finite element analysis of the Single-Lap Joint

Due to the relative difficulty in obtaining analytical solutions for single-lap joints subject to various loading conditions, many instead use finite element analysis to study their stresses. For example, Tsai and Morton [1] evaluated analytical and finite element analysis solutions to single-lap joints. While several solutions were investigated, as presented in chapter three of this thesis, none were universally valid for all single-lap joints. They found that Hart-Smith's [2] solution was most accurate in predicting stresses in short single-lap joints, and Oplinger's [3] solution was the most accurate for long single-lap joints. However, Finite element analysis with non-linear geometrical effects included in the analysis is universally applicable to single-lap joints. Tsai and Morton performed two-dimensional plane-strain finite element analysis with material linearity and geometric nonlinearity in order to investigate the edge moment, analyze the state of stress in the adhesive layer, and evaluate the analytical solutions of Goland and Reisner [4], Hart-Smith [2], and Oplinger [3], reaching the conclusions listed above.

Grant, Adams, and de Silva [5] experimentally and numerically studied single-lap joints in context of the automotive industry, and regarding finite element analysis, used a two-dimensional plane-strain model with isoparametric elements. They found that the finite element results were very sensitive to mesh size, as mathematical singularities exist at the ends of the overlap at the adherend-adhesive interface. In order to combat this, they simply conducted comparisons through similar meshes. Adams [6] utilized finite element analysis in order to predict single-lap joint strength, and found that finite element analysis was the most efficient method for analyzing single-lap joints with their geometric nonlinearity and possible corner rounding or complicated adhesive termination, like spew fillets. He commented that analytical techniques cannot be used to predict the strength of adhesively-bonded lap joints without an uncertainty factor, as they cannot adequately describe the real stress and strain conditions at the ends of the joint, where failure initiates.

In order to adequately model single-lap joints and how their important parameters affect the stresses in the adherends and adhesive, two-dimensional plane-strain analysis with a consistent isoparametric mesh was conducted across all cases presented. [1] and [5] both encountered the issue of stress singularity at the sharp corners of a single-lap joint, and both combatted the issue with a consistent mesh; a mesh that measures stress from the same distance from the singularity. In the case of this thesis, stress was always measured at the same point across cases, and it was always measured at the centroid of the element, with 40 elements per basic case adherend thickness. This allowed for a comparison of stresses across cases, without danger of influence from the singularity. The good correlation between analytical deflection and finite element deflection in Figure 4.1, re-presented below, verifies this mesh scheme.

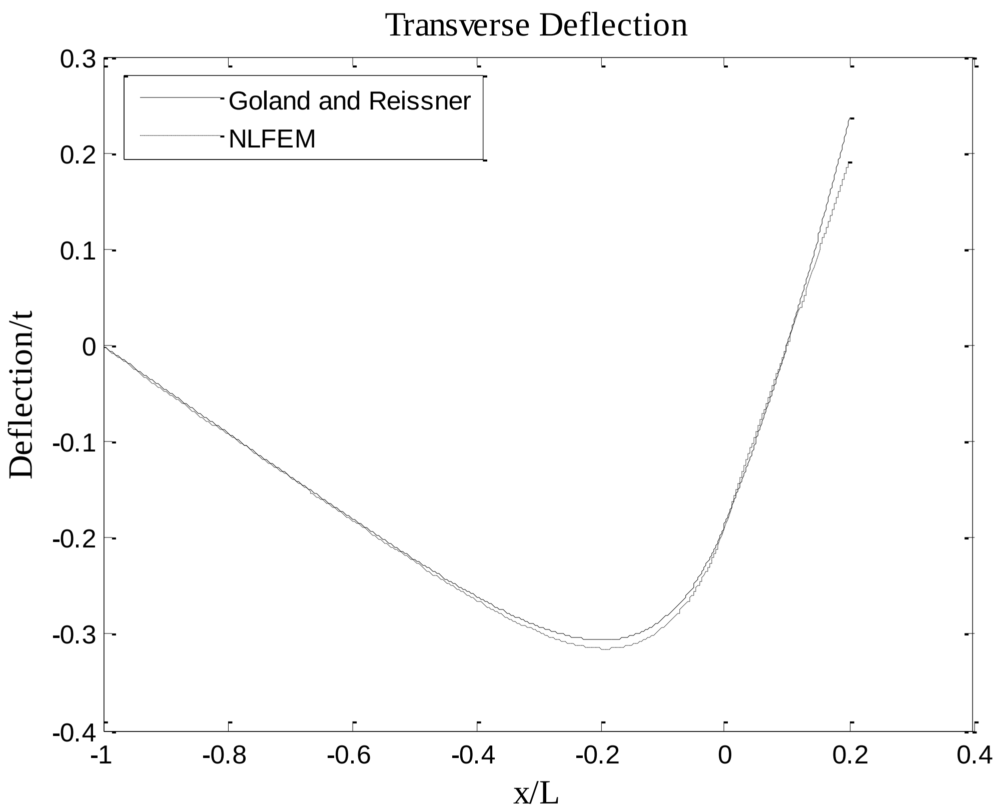

Figure 4.1 Analytical solution and FE solution

Differing adherend Young's Modulus, *E*, thickness, *t*, length, *L*, bond length, *2c*, and adhesive thickness, η, were all investigated. All but the case of varying adhesive thickness were conducted with a zero adhesive thickness, to study the effects of dissimilar adherends on the adherends themselves. Both tensile loading and three-point bending simulations were performed, and diagrams of each setup can be seen in Figures 4.2 and 4.3.

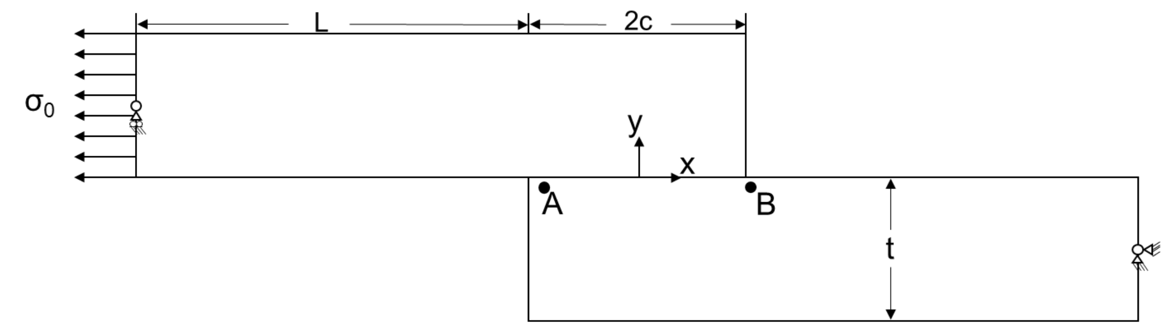

Figure 4.2 Finite element boundary conditions in tension

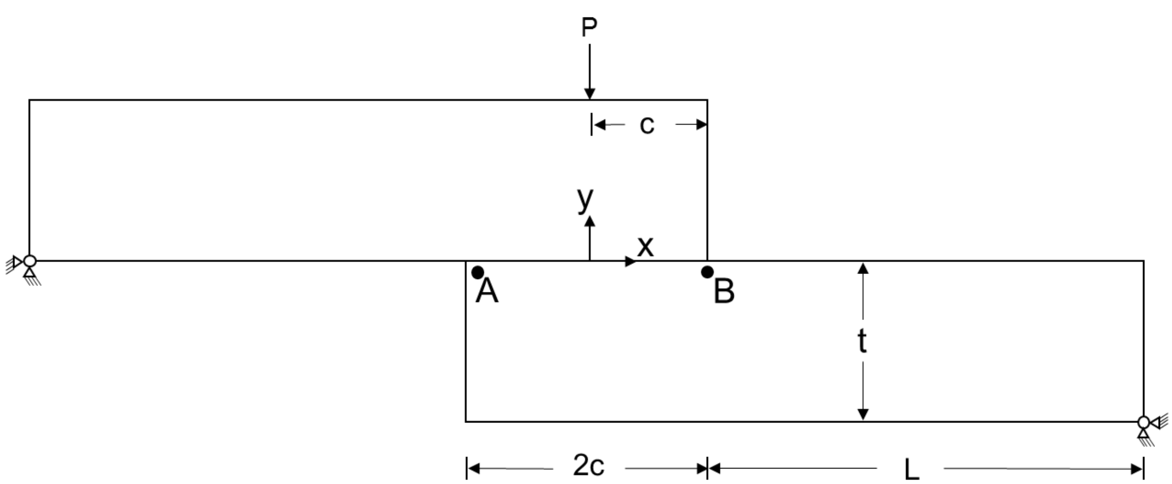

Figure 4.3 Finite element boundary conditions in three point bending

Figure 4.2 outlines the dimensional symbols of the model, with *L* being adherend length beyond the overlap, *c* being half of the overlap length keeping with Goland and Reissner's [1] convention, and *t* being thickness of the adherend. Points *A* and *B* were found to be the points of critical stress concentration, and subsequently all instances of the parametric study had stresses measured at these points and compared to the stresses measured in the "basic case," a homogeneous single-lap joint with zero adhesive thickness.

Regarding the basic cases, the input stress in the tension case, σ_0, was unity, in order to make all results normalized with respect to this input stress. The input load, for the three-point bending basic case, was unity as well, for the same reason. In both basic cases, L was 15 m, c was 1.5 m, and t was 1 m. Young's Modulus and Poisson's Ratio in each case was set to near that of aluminum, 70 GPa and 0.33 respectively. The mesh size used was the same uniform, isoparametric mesh used in the verification case, in order to hold the basic cases and parametric study cases to follow to that verification. As is illustrated in Figure 4.2, the far positive x face of the lower adherend was pinned at its midpoint, and the far negative x face, where the input stress was applied, was assigned a roller condition at its midpoint, again catering to the conditions in [1]. Contour maps of the critical region and tables of stress values at points A and B for these basic cases are shown below. Countour maps are rotated 90 degrees clockwise in order to maximize the size of the map in the allowable space on the page. A rotated coordinate system is transposed over the image for ease of understanding. The Von-Mises stress in ABAQUS is calculated according to equation 4.1, while the other stresses are simply the classic definition.

$$\sigma_{vm}^2 = \sigma_{xx}^2 - \sigma_{xx}\sigma_{yy} + \sigma_{yy}^2 + 3\tau_{xy}^2 \qquad \textbf{(4.1)}$$

Table 4.1 Tensile basic case stress values at points *A* and *B*

	A	*B*
σ_{vm}	4.996	7.317
σ_{xx}	2.379	7.368
σ_{yy}	3.927	1.962
τ_{xy}	-2.099	-1.813

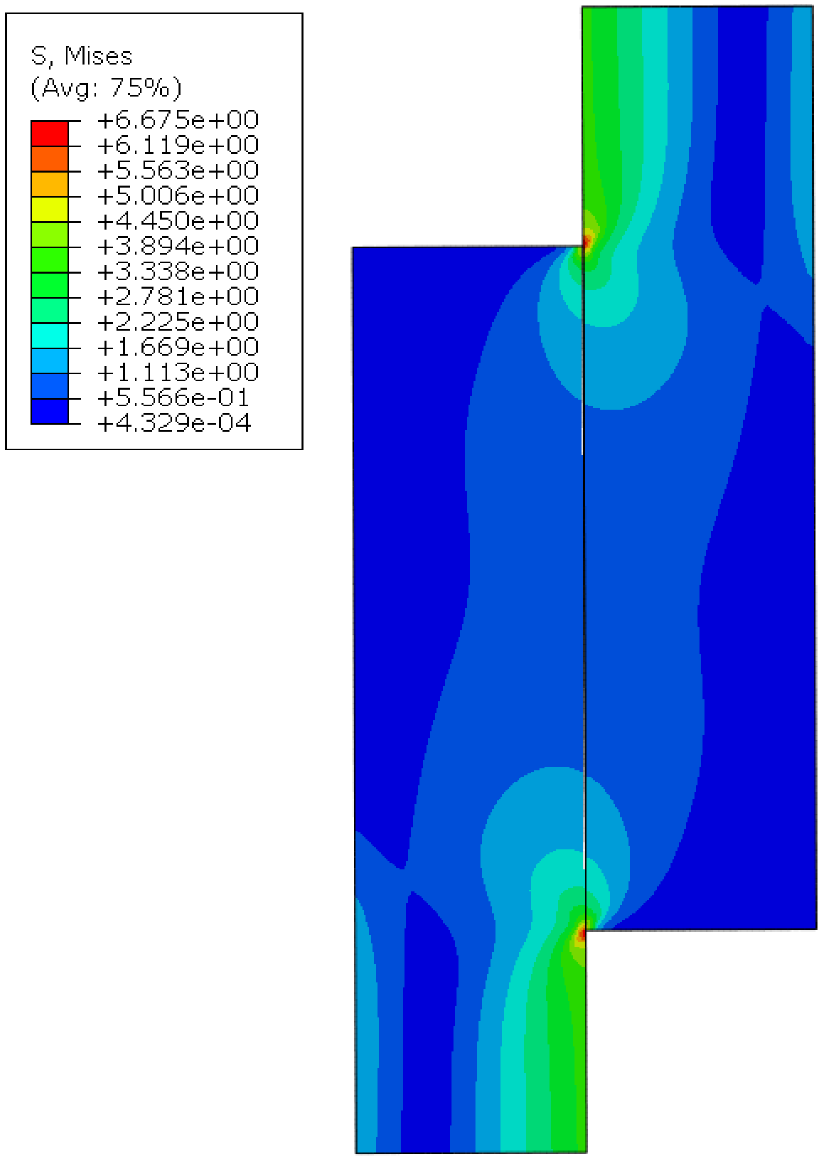

Figure 4.4 Von-Mises stress contour map under unit tensile loading

(For the interpretation of the references to color in this and all other figures, the reader is referred to the electronic version of this thesis)

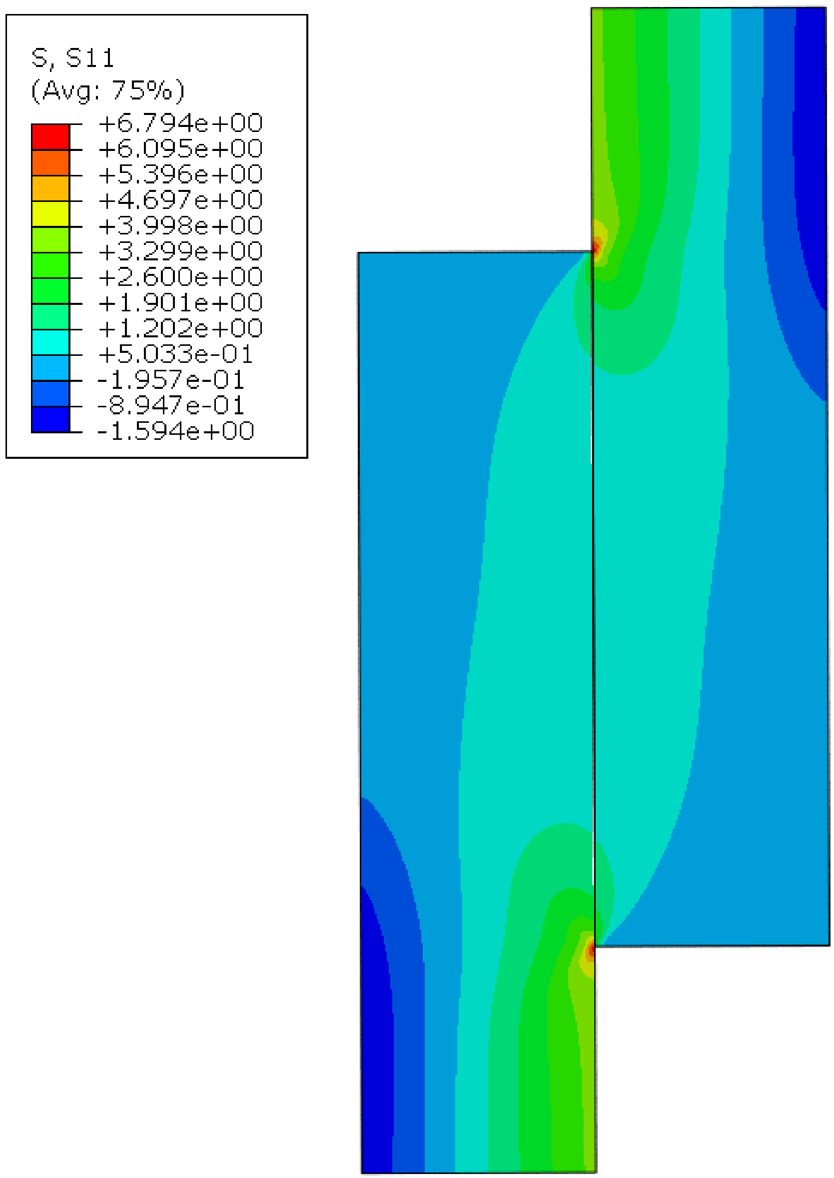

Figure 4.5 X direction stress contour map under unit tensile loading

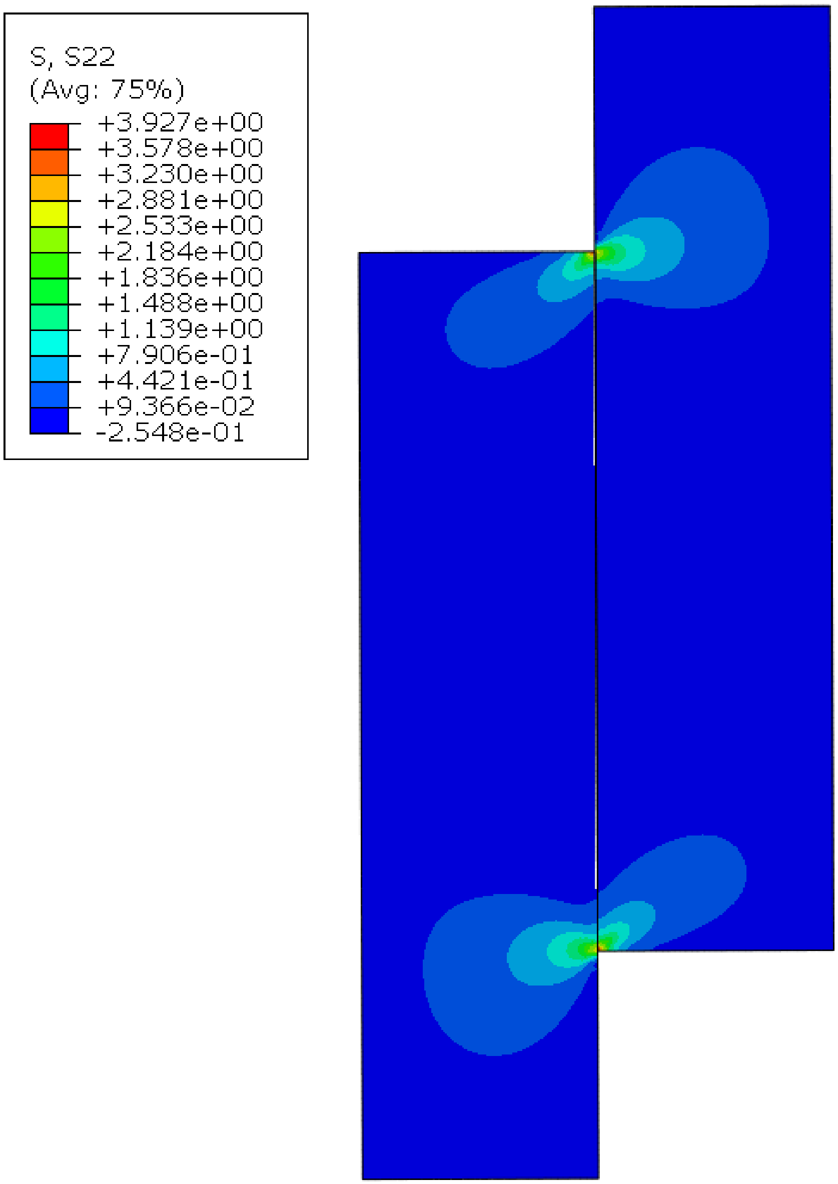

Figure 4.6 Y direction stress contour map under unit tensile loading

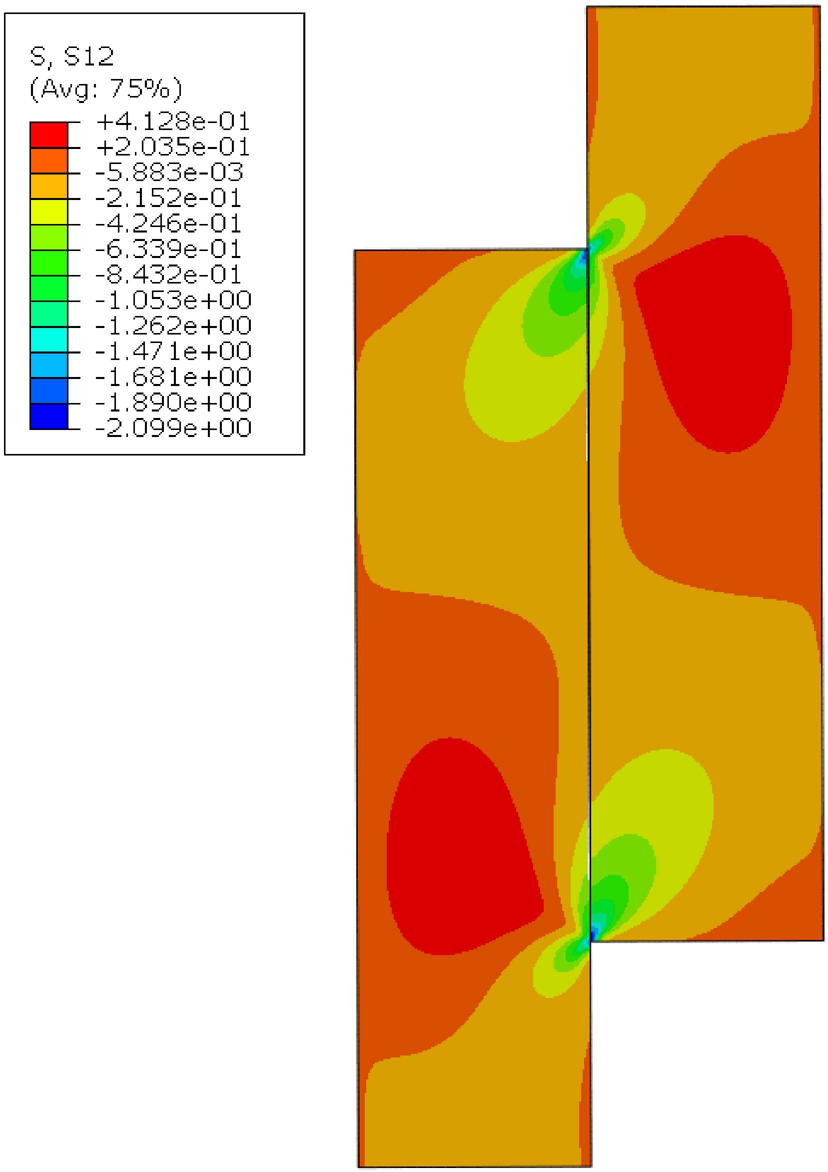

Figure 4.7 XY shear stress contour map under unit tensile loading

Table 4.2 Tensile basic case stress values at points *A* and *B*

	A	*B*
σ_{vm}	31.15	98.10
σ_{xx}	16.25	-98.04
σ_{yy}	27.38	-55.74
τ_{xy}	-11.66	25.64

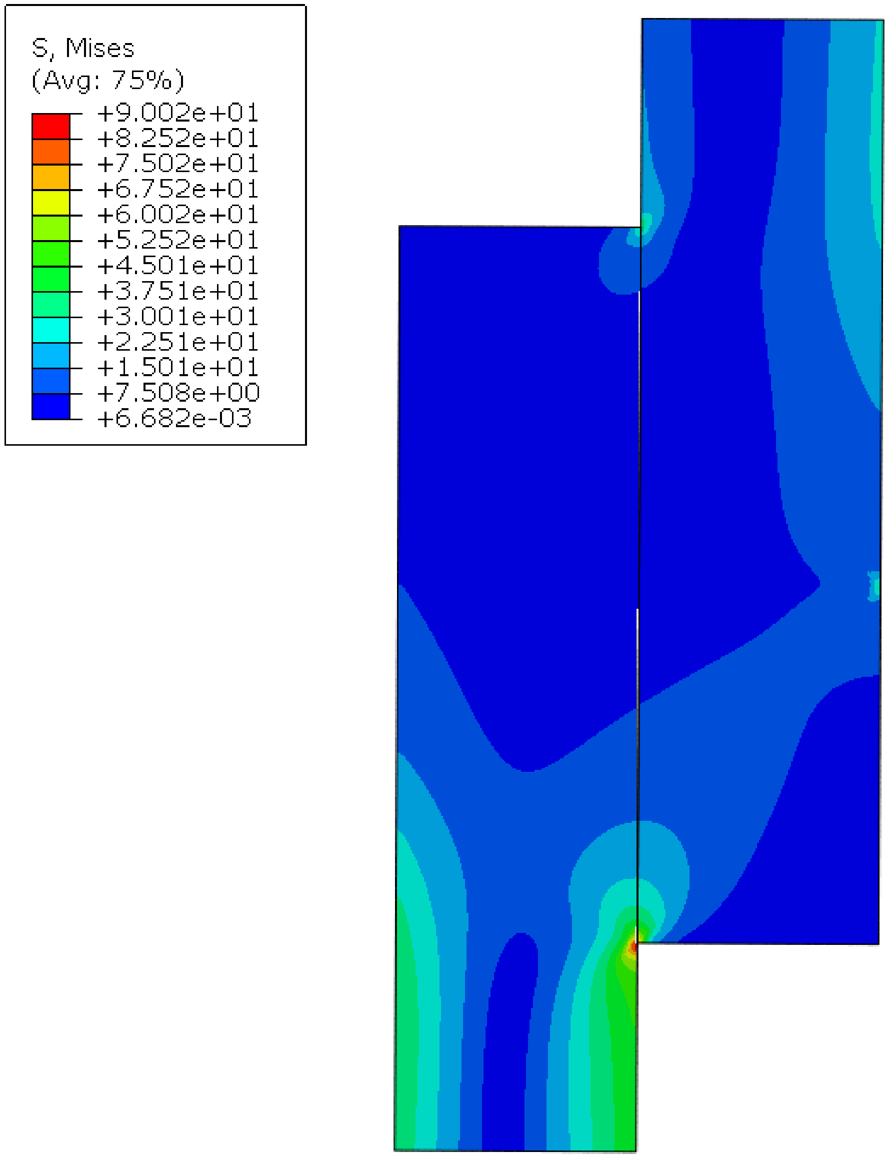

Figure 4.8 Von-Mises stress contour map under three point bending load

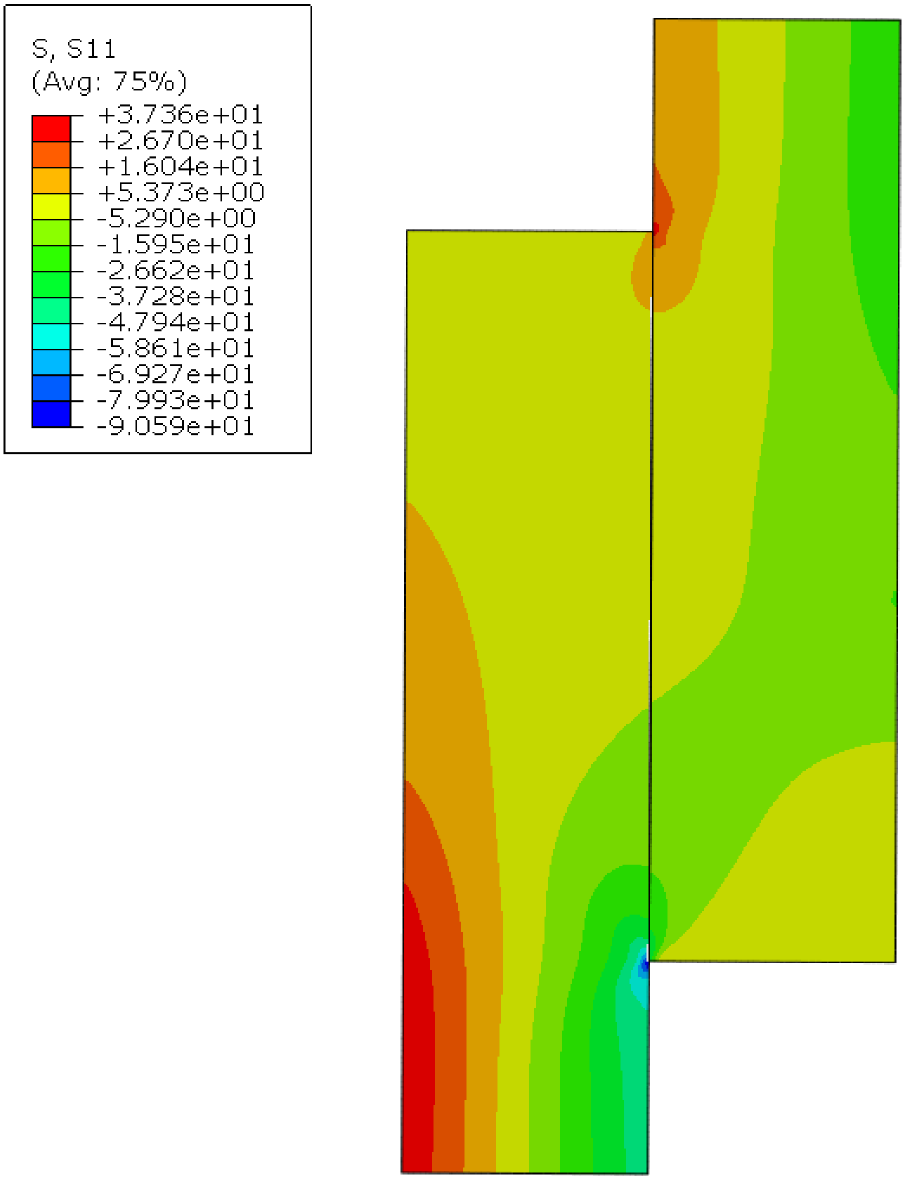

Figure 4.9 X direction stress contour map under three point bending load

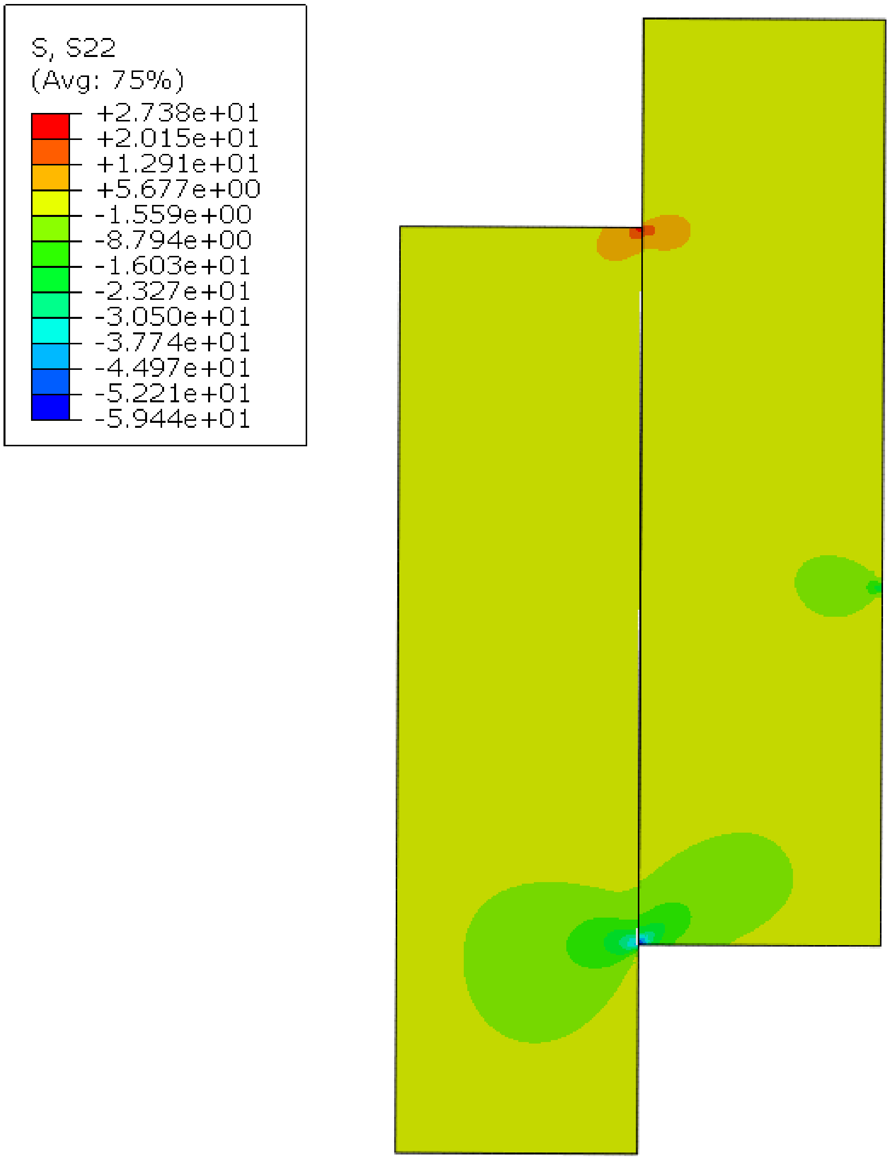

Figure 4.10 Y direction stress contour map under three point bending load

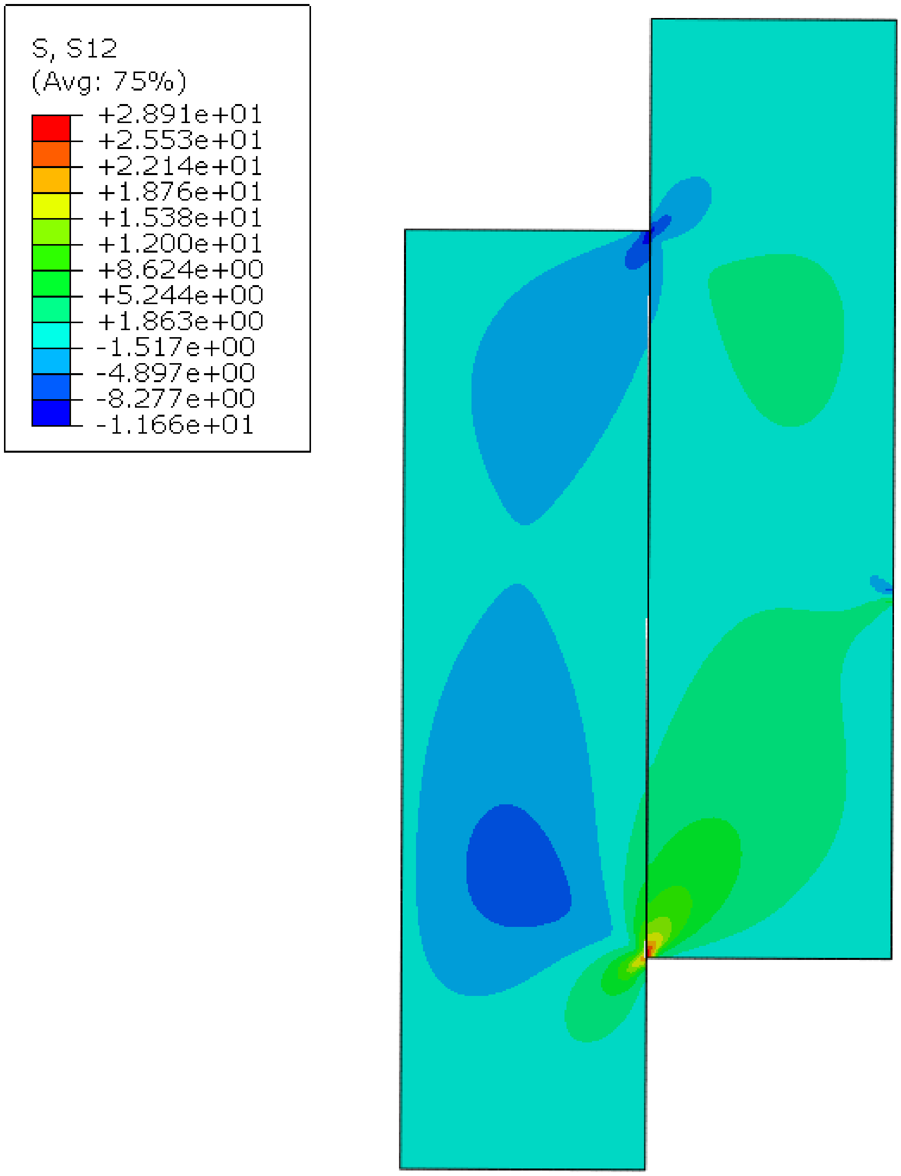

Figure 4.11 XY shear stress contour map under three point bending load

As can be immediately seen from the stress contours, there are two obvious concentration points on each adherend in an ideally bonded single-lap joint. The following chapters explore how these points' stresses vary as various parameters are changed, and discuss why.

REFERENCES

REFERENCES

[1] Tsai, M. Y., Morton, J. "An Evaluation of Analytical and Numerical Solutions to the Single-Lap Joint." *Int. J. Solids Structures.* 31. (1994)

[2] Hart–Smith, L. J. "Adhesive-bonded single-lap joints." *NASA.* CR-112236. (1973)

[3] Oplinger, D. W. "A layered beam theory for single lap joints." *Army Materials Technology Laboratory Report*. MTL TR91-23. (1991)

[4] Goland, M., Reissner, E. "The stresses in cemented joints." *J. Appl. Mech.* 11. (1944)

[5] Grant, L. D. R., Adams, R. D., de Silva, L. F. M. "Experimental and numerical analysis of single-lap joints for the automotive industry." *International Journal of Adhesion and Adhesive.* 29. (2009)

5 Results of the FEA Based Parametric Study

5.1 Varied Adherend Thickness Under Ideal Bonding and a Tensile Load

Several key parameters of the single-lap joint, Young's Modulus, adherend thickness, bond length, free adherend length, and later adhesive thickness and Young's Modulus, were varied in order to ascertain the stresses' sensitivity and general behavior under their variation. The first parameter studied was Young's Modulus, E, under tensile loading. Tables 5.1 and 5.2 display the critical stresses and their stress concentration factor (SCF) with respect to the basic case, outlined in the previous chapter, at points A and B respectively, and Figures 5.2 and 5.3 show each SCF as the ratio of E to the basic case, E_0, varies. In each case, ratios of 0.2, 0.5, 2, and 5 were considered. Figure 5.1 highlights the critical points and the varied parameters. Additional ratios were considered where more data was needed in certain cases. Again, all stresses are normalized with respect to their unit input load, and a uniform isoparametric mesh was used. This mesh has been verified in the previous chapter with reference to the analytical displacement calculated.

Stresses were calculated at the centroid of each quadrilateral element at the critical points A and B. Take note that only the lower adherend's properties were varied, and all stress measurements were taken from this lower adherend, unless otherwise noted. The ratios studied rendered checking both adherends redundant, because as the ratio is increased, the measured adherend played the roll of the fixed parameter adherend.

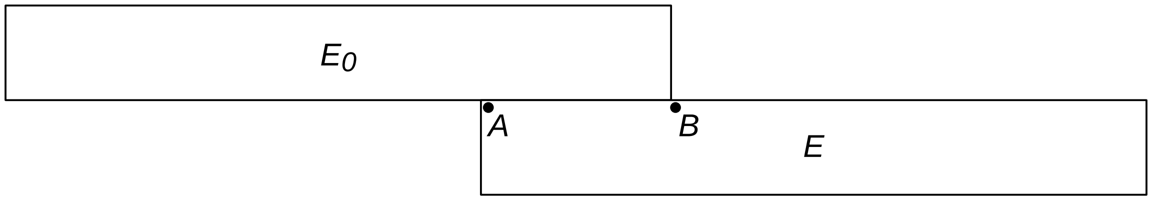

Figure 5.1 Ideally bonded Young's Modulus variation critical points

Table 5.1 Reference stress values and SCFs at point *A* with varying E/E_0

E/E_0	σ_{vm} (SCF)	σ_{xx} (SCF)	σ_{yy} (SCF)	τ_{xy} (SCF)
0.2	2.444 (0.489)	0.964 (0.314)	2.294 (0.584)	-0.837 (0.399)
0.5	3.917 (0.784)	1.943 (0.634)	3.446 (0.878)	-1.457 (0.694)
1.0	4.996 (1.000)	3.066 (1.000)	3.927 (1.000)	-2.099 (1.000)
2.0	5.967 (1.194)	4.512 (1.472)	3.561 (0.907)	-2.697 (1.285)
5.0	8.358 (1.673)	6.780 (2.211)	2.264 (0.577)	-3.372 (1.607)

Table 5.2 Reference stress values and SCFs at point *B* with varying E/E_0

E/E_0	σ_{vm} (SCF)	σ_{xx} (SCF)	σ_{yy} (SCF)	τ_{xy} (SCF)
0.2	9.290 (1.270)	9.214 (1.251)	2.817 (0.747)	-2.755 (1.520)
0.5	8.339 (1.140)	8.306 (1.127)	3.765 (0.999)	-2.189 (1.207)
1.0	7.317 (1.000)	7.368 (1.000)	3.769 (1.000)	-1.813 (1.000)
2.0	6.217 (0.850)	6.355 (0.863)	3.211 (0.852)	-1.340 (0.739)
5.0	5.028 (0.687)	5.206 (0.707)	2.119 (0.562)	-0.776 (0.428)

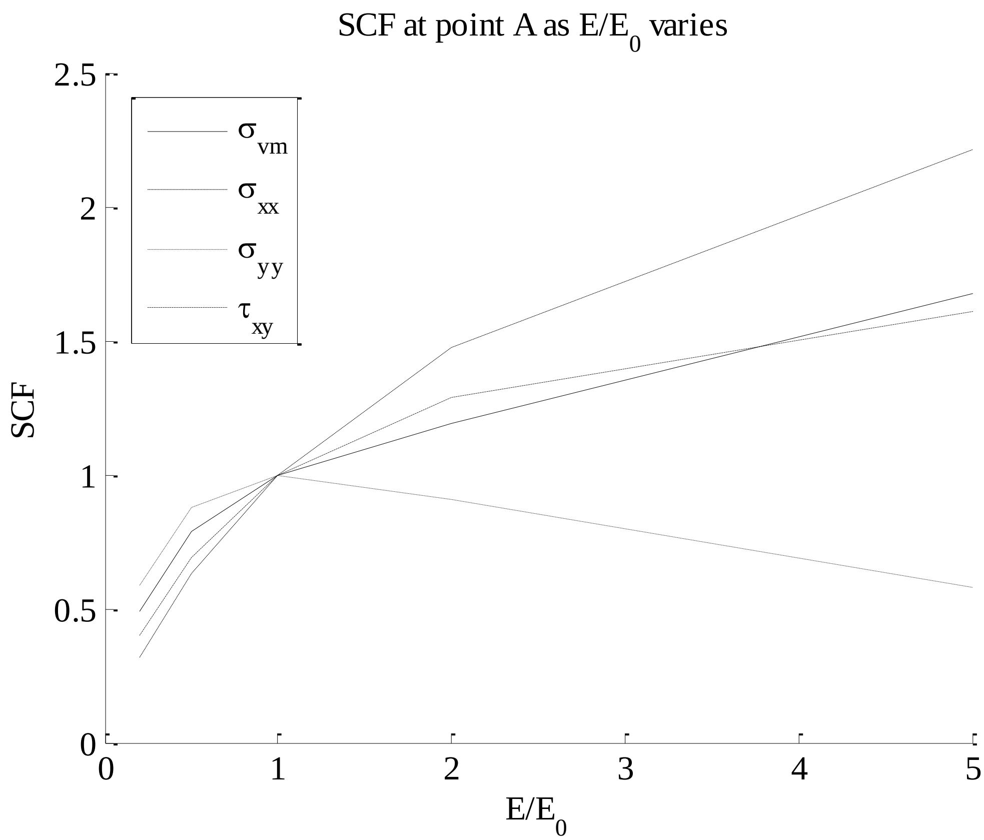

Figure 5.2 SCFs as *E/E_0* varies at point *A*

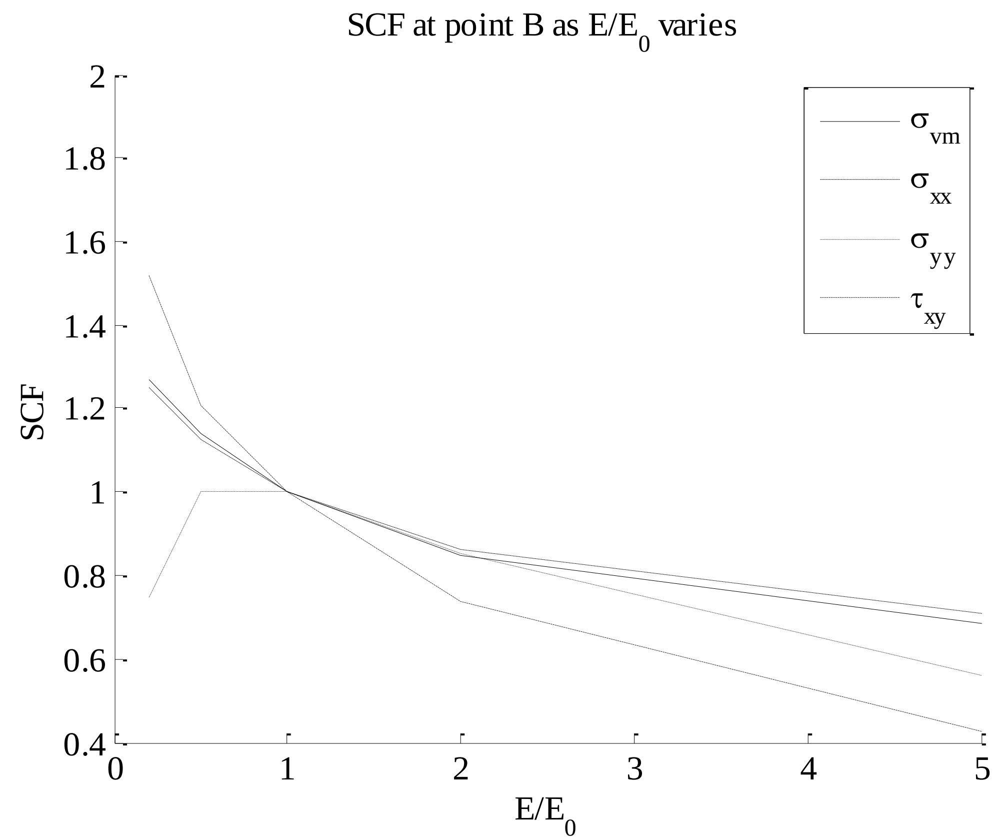

Figure 5.3 SCFs as *E/E_0* varies at point *B*

Observing the SCFs at point *A*, for each type of stress except the Y direction, they increase as the ratio E/E_0 increases. At point *B*, however, the opposite is true. As the ratio increases, the SCFs decrease, although not as drastically. For both points, Y direction SCF increased up to a ratio of unity, and then decreased. X direction stress is the most sensitive to variations in adherend *E* at point *A*, while XY shear stress was the most sensitive at point *B*. Therefore, one should maintain an E/E_0 ratio of unity across both adherends when constructing a single-lap joint for tensile loading.

Before commenting on why the various stresses behave in the manner that they do, one must comment on the definition of SCF in these cases. SCF is simply the ratio of current stress at the point in question to the stress measured in the basic, homogeneous case. Therefore, increasing SCF can be attributed to an increasingly tensile stress if basic case stress is positive, or increasingly compressive stress if basic case stress is negative. One must observe that Von Mises stress is always positive, and therefore is simply a way to visualize stress evolution across X, Y, and XY directions in a single value. In reference to varied Young's Modulus, for Von Mises stress and SCF is always positive as expected. X and Y direction stresses and SCFs are also always positive. XY direction shear stress is always negative, but SCF is always positive, as expected. Therefore, for X and Y direction stresses, increasing SCF means an increasingly tensile stress, and decreasing refers to decreasingly tensile stress, or increasingly compressive stress. In regards to decreasing SCF, the stress is simply becoming less tensile if it approaches zero. If SCF crosses zero, the stresses are shifting from tensile to compressive.

As single-lap joints are loaded according to the boundary conditions displayed in the previous chapter, in tension, the bonded region tends to rotate counter-clockwise due to the eccentric loading angle. Therefore, Y direction stresses at point *A* become increasingly tensile with increased transferred load, and at point *B* become increasingly compressive with increased load. The same holds true for X direction stress, although this is also influenced by the normal load applied to the upper adherend. Shear stress, due to sign convention, increases in negative intensity at point *A*, and decreases in negative intensity at point *B*, due to the direction of the load.

In reference to varied Young's Modulus, all stresses are explained by this logic except for Y direction stress. At both points, it increases up to a Young's Modulus ratio of unity, but then decreases as the ratio increases away from unity. At point *A*, this means it follows the previous logic up to a ratio of unity, and then diverges. At point *B*, this means it diverges from the previous logic up to a ratio of unity, and then converges. For ratios less than unity, the varied adherend, from which the stresses are measured, has a smaller stiffness than the unvaried adherend. This means that it will displace more, and experience less stress. For ratios greater than unity, the opposite is true. However, whether the ratio is less than or greater than unity, there is always one adherend that has a higher Young's Modulus than the other, and therefore it has greater stiffness. This stiffness resists the rotation of the bonded region, and therefore, the moment caused by it, resulting in a lesser Y direction stress regardless of Young's Modulus ratio, and the stresses were instead translated into X direction and XY shear stresses. In other words, Y direction stress is decreased because regardless of the Young's Modulus ratio, except if unity, one adherend is always stiffer than the other. This stiffer adherend dictates the amount of central rotation, and the rotation is translated into axial deformation of the less stiff adherend. A ratio of unity is different, as the body is ideally bonded, and acts as a homogeneous structure.

5.2 Varied Adherend Thickness Under Ideal Bonding and a Tensile Load

Varying adherend thickness was also investigated. Tables 5.3 and 5.4 show reference stress values and SCFs at points *A* and *B* under tensile loading, and Figures 5.5 and 5.6 plot each stress' evolution as the ratio of t/t_0 is varied. Figure 5.4 highlights the critical points and parameter being varied in this case.

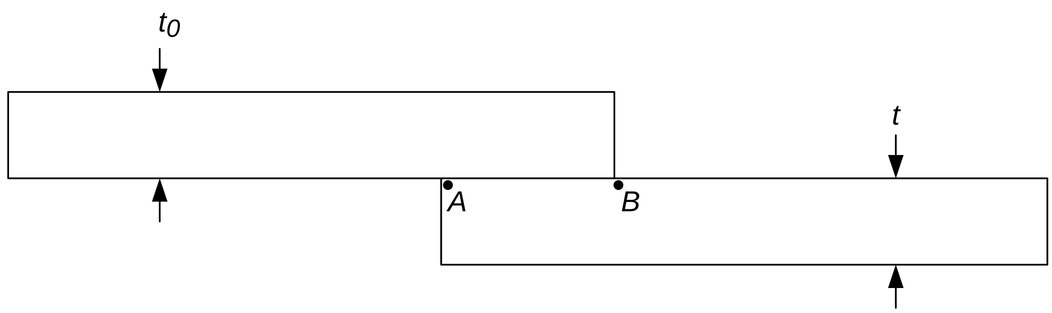

Figure 5.4 Ideally bonded thickness variation critical points

Table 5.3 Reference stress values and SCFs at point *A* with varying t/t_0

t/t_0	σ_{vm} (SCF)	σ_{xx} (SCF)	σ_{yy} (SCF)	τ_{xy} (SCF)
0.2	2.692 (0.539)	1.918 (0.626)	1.645 (0.419)	-1.207 (0.575)
0.5	3.738 (0.748)	2.418 (0.789)	2.780 (0.708)	-1.629 (0.776)
1.0	4.996 (1.000)	3.066 (1.000)	3.927 (1.000)	-2.099 (1.000)
2.0	7.200 (1.441)	4.281 (1.396)	5.825 (1.483)	-2.955 (1.408)
5.0	13.890 (2.780)	7.930 (2.586)	11.610 (2.957)	-5.527 (2.633)

Table 5.4 Reference stress values and SCFs at point *B* with varying t/t_0

t/t_0	σ_{vm} (SCF)	σ_{xx} (SCF)	σ_{yy} (SCF)	τ_{xy} (SCF)
0.2	50.320 (6.877)	52.400 (7.112)	19.79 (5.251)	-9.168 (5.057)
0.5	15.560 (2.127)	15.860 (2.153)	7.285 (1.933)	-3.528 (1.946)
1.0	7.317 (1.000)	7.368 (1.000)	3.769 (1.000)	-1.813 (1.000)
2.0	3.752 (0.513)	3.756 (0.510)	1.991 (0.528)	-0.961 (0.530)
5.0	1.217 (0.166)	1.245 (0.169)	0.420 (0.111)	-0.252 (0.139)

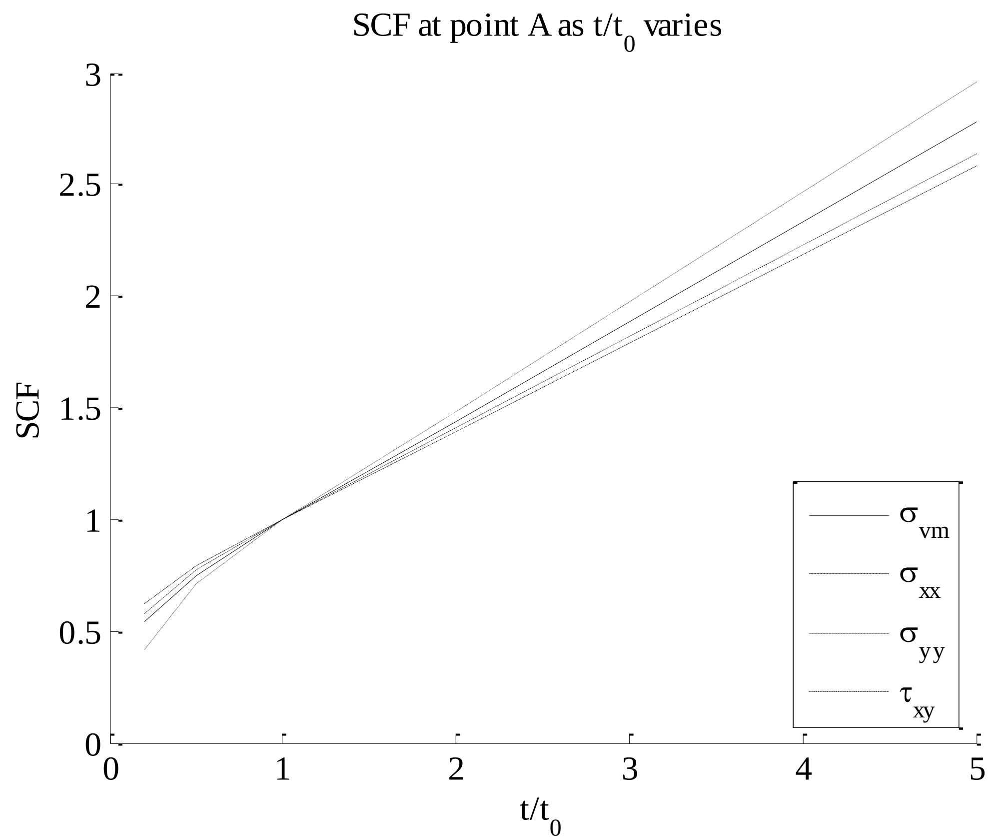

Figure 5.5 SCFs as t/t_0 varies at point *A*

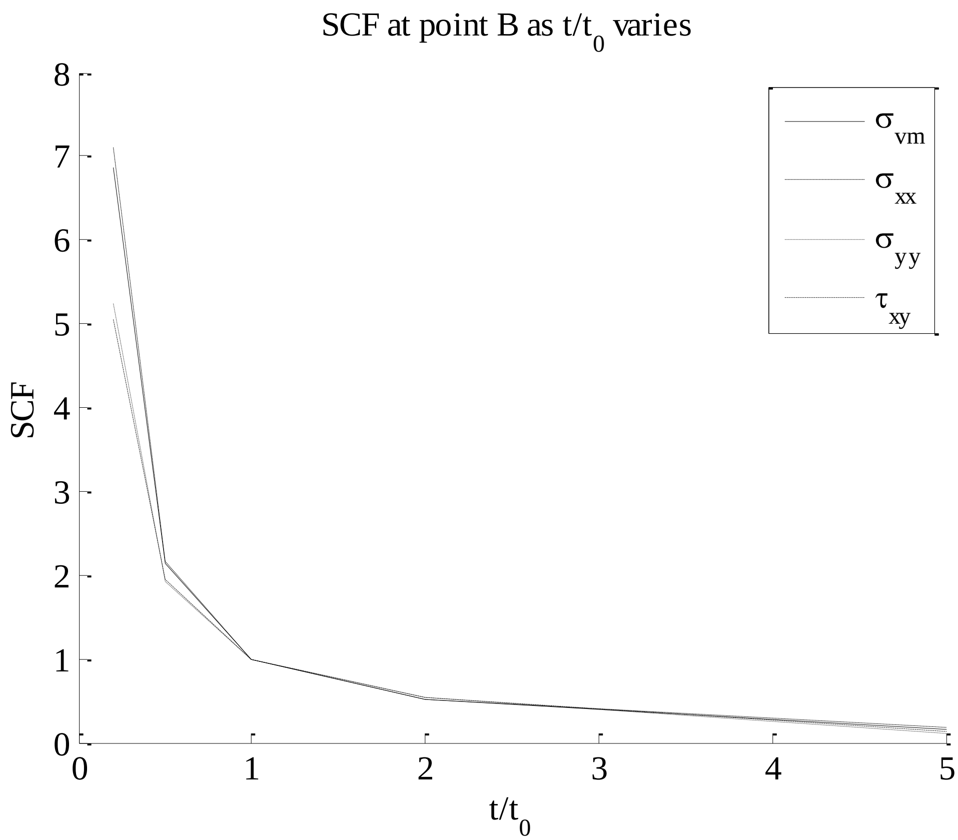

Figure 5.6 SCFs as t/t_0 varies at point *B*

Varied adherend thickness behaved much the same as varied Young's Modulus. An increasing ratio of t/t_0 resulted in increasing SCFs in all stresses at point *A*, and decreasing SCFs in all stresses at point *B*. All stresses at each point behaved roughly the same, however stresses at point *B* were impacted much more by smaller adherend thickness. As with the variation in *E*, a t/t_0 ratio of unity is suggested for construction single-lap joints in tension.

The logic displayed after the case of varied Young's Modulus still holds here, and explains the universal increase in SCF at point *A* and decrease in SCF at point *B*. Regarding Y direction stress, the varied thickness not only impacts adherend stiffness, but effects the moment of inertia on a cubic level, and also increases or decreases the eccentricity of the load, and therefore the moment. Whether the varied adherend is thinner or thicker than the unvaried adherend, the eccentricity of the load is largely affected. This moment causing eccentricity has been shown to largely impact the edge moment in the bonded region, and as this is the dominant stress, it overshadows all other effects thickness may have. As a result, Y direction stress follows the same trends as all other forms of stress measured, and all stresses behave as expected under varied thickness.

5.3 Varied Free Adherend Length Under Ideal Bonding and a Tensile Load

Free adherend length variation was then simulated. Tables 5.5 and 5.6 tabulate reference stress values and their associated SCFs as L/L_0 varies, and Figure 5.8 and 5.9 illustrate the SCFs graphically. Figure 5.7 highlights the parameter under variation and the critical points investigated.

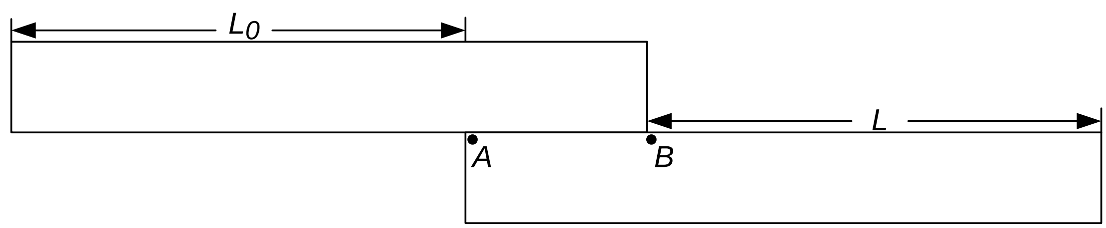

Figure 5.7 Ideally bonded free adherend length variation critical points

Table 5.5 Reference stress values and SCFs at point *A* with varying L/L_0

L/L_0	σ_{vm} (SCF)	σ_{xx} (SCF)	σ_{yy} (SCF)	τ_{xy} (SCF)
0.2	8.530 (1.707)	5.062 (1.651)	6.907 (1.759)	-3.499 (1.667)
0.5	6.973 (1.396)	4.183 (1.364)	5.595 (1.425)	-2.883 (1.374)
1.0	4.996 (1.000)	3.066 (1.000)	3.927 (1.000)	-2.099 (1.000)
2.0	3.868 (0.774)	2.428 (0.792)	2.974 (0.757)	-1.651 (0.787)
5.0	2.327 (0.466)	1.550 (0.506)	1.663 (0.424)	-1.036 (0.494)

Table 5.6 Reference stress values and SCFs at point *B* with varying L/L_0

L/L_0	σ_{vm} (SCF)	σ_{xx} (SCF)	σ_{yy} (SCF)	τ_{xy} (SCF)
0.2	0.692 (0.095)	0.550 (0.075)	-0.291 (-0.077)	-0.050 (0.028)
0.5	4.242 (0.580)	4.287 (0.582)	2.027 (0.538)	-1.016 (0.560)
1.0	7.317 (1.000)	7.368 (1.000)	3.769 (1.000)	-1.813 (1.000)
2.0	9.074 (1.240)	9.128 (1.240)	4.765 (1.264)	-2.268 (1.251)
5.0	11.491 (1.571)	11.548 (1.567)	6.134 (1.628)	-2.894 (1.596)

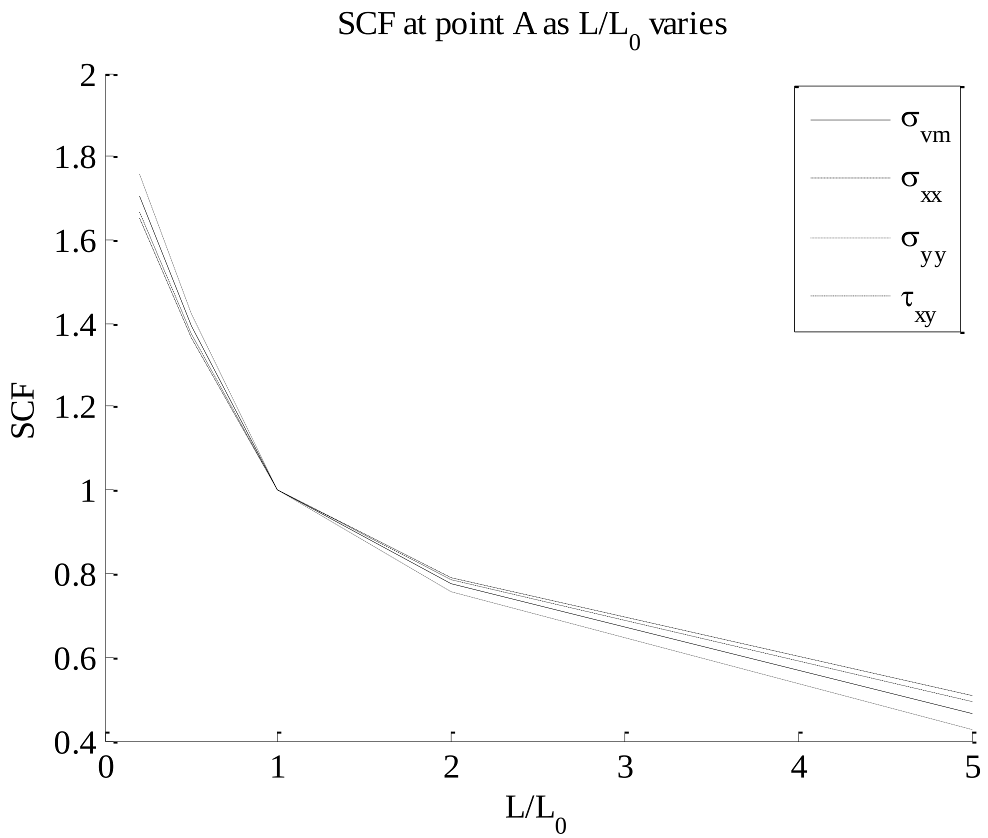

Figure 5.8 SCFs as L/L_0 varies at point *A*

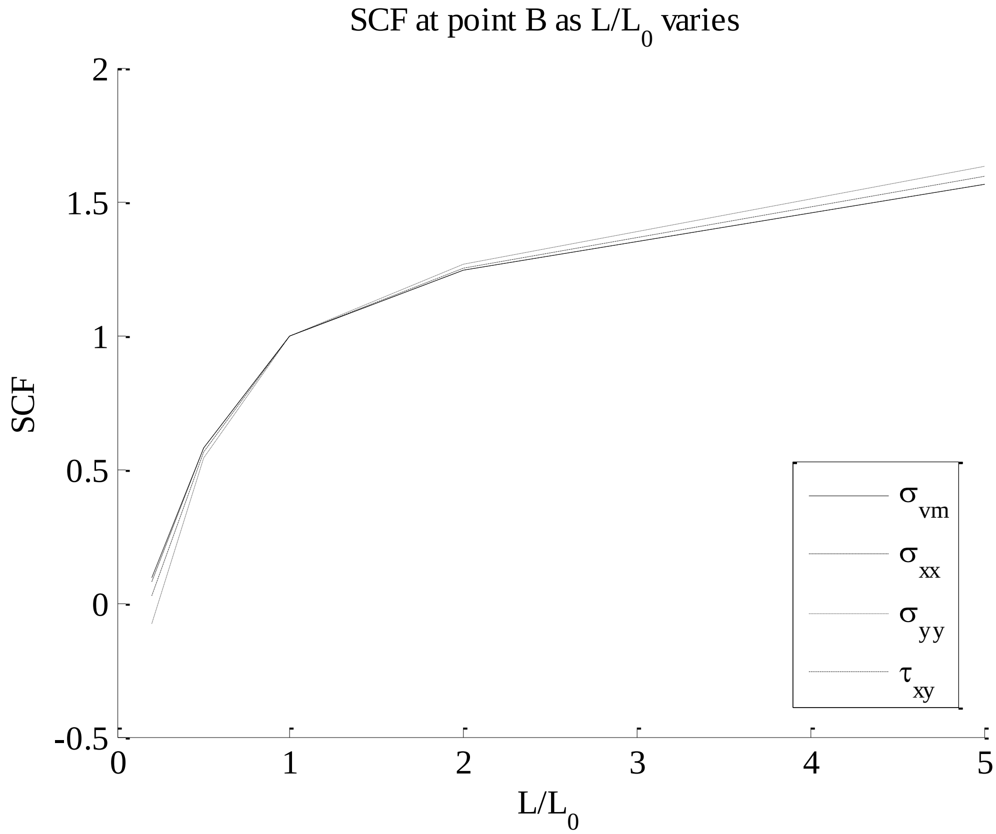

Figure 5.9 SCFs as *L/L_0* varies at point *B*

Under varied free adherend length, SCFs at points *A* and *B* behave with trends opposite that of varied Young's Modulus or thickness. At point *A*, the SCFs decrease with increasing L/L_0, and at point *B*, the SCFs increase. Although the stress' behavior is opposite the varied *E* and *t* cases, one should still attempt to keep the two adherends in a single-lap joint of equal length in order to minimize overall adherend stress in tension.

Free adherend length affects the eccentricity of the load, and therefore the edge moment, which dominates the bonded region's stresses. When the ratio is less than unity, it greatly effects the eccentricity, but larger than unity, it effects it less and less. This is reflected, at both points *A* and *B*, by the large slopes for ratios less than unity, and smaller slopes at the ratio increases past unity. As free adherend length is shortened, point *A*'s stresses become more tensile, and point *B*'s stresses become less tensile. As expected, the opposite trend is observed as free adherend length is increased.

5.4 Varied Bonding Length Under Ideal Bonding and a Tensile Load

Joint bonding length was also varied. Tables 5.7 and 5.8 display the reference stress values and SCFs at points *A* and *B* respectively, and Figures 5.11 and 5.12 display the evolving SCFs graphically. Figure 5.10 highlights the varied parameter and critical points.

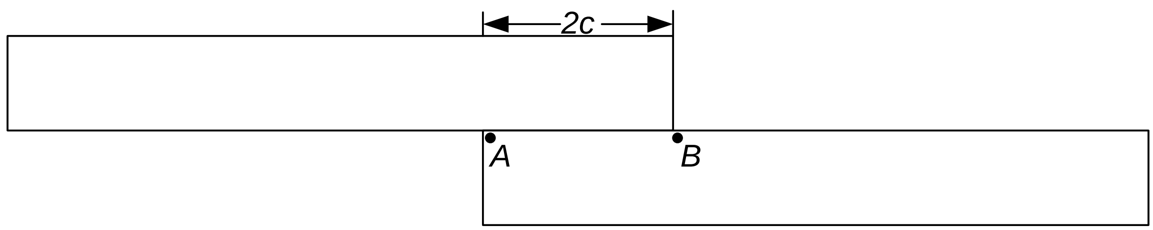

Figure 5.10 Ideally bonded bonding length variation critical points

Table 5.7 Reference stress values and SCFs at point *A* with varying c/c_0

c/c_0	σ_{vm} (SCF)	σ_{xx} (SCF)	σ_{yy} (SCF)	τ_{xy} (SCF)
0.20	5.100 (1.021)	3.337 (1.088)	2.849 (0.726)	-2.347 (1.118)
0.50	4.789 (0.959)	3.083 (1.006)	3.558 (0.906)	-2.089 (0.995)
0.75	5.006 (1.002)	3.087 (1.007)	3.914 (0.997)	-2.112 (1.006)
1.00	4.996 (1.000)	3.066 (1.000)	3.927 (1.000)	-2.099 (1.000)
1.50	4.641 (0.923)	2.856 (0.932)	3.637 (0.926)	-1.954 (0.931)
2.00	4.599 (0.921)	2.841 (0.927)	3.592 (0.915)	-1.942 (0.925)
5.00	3.861 (0.773)	2.425 (0.791)	2.965 (0.755)	-1.649 (0.786)

Table 5.8 Reference stress values and SCFs at point *B* with varying c/c_0

c/c_0	σ_{vm} (SCF)	σ_{xx} (SCF)	σ_{yy} (SCF)	τ_{xy} (SCF)
0.20	8.120 (1.110)	8.251 (1.120)	3.064 (0.813)	-1.808 (0.997)
0.50	7.424 (1.015)	7.514 (1.020)	3.491 (0.926)	-1.760 (0.971)
0.75	7.372 (1.008)	7.427 (1.008)	3.764 (0.999)	-1.820 (1.004)
1.00	7.317 (1.000)	7.368 (1.000)	3.769 (1.000)	-1.813 (1.000)
1.50	6.813 (0.931)	6.861 (0.931)	3.497 (0.928)	-1.687 (0.931)
2.00	6.785 (0.927)	6.837 (0.928)	3.458 (0.918)	-1.672 (0.922)
5.00	5.805 (0.793)	5.860 (0.795)	2.875 (0.763)	-1.409 (0.777)

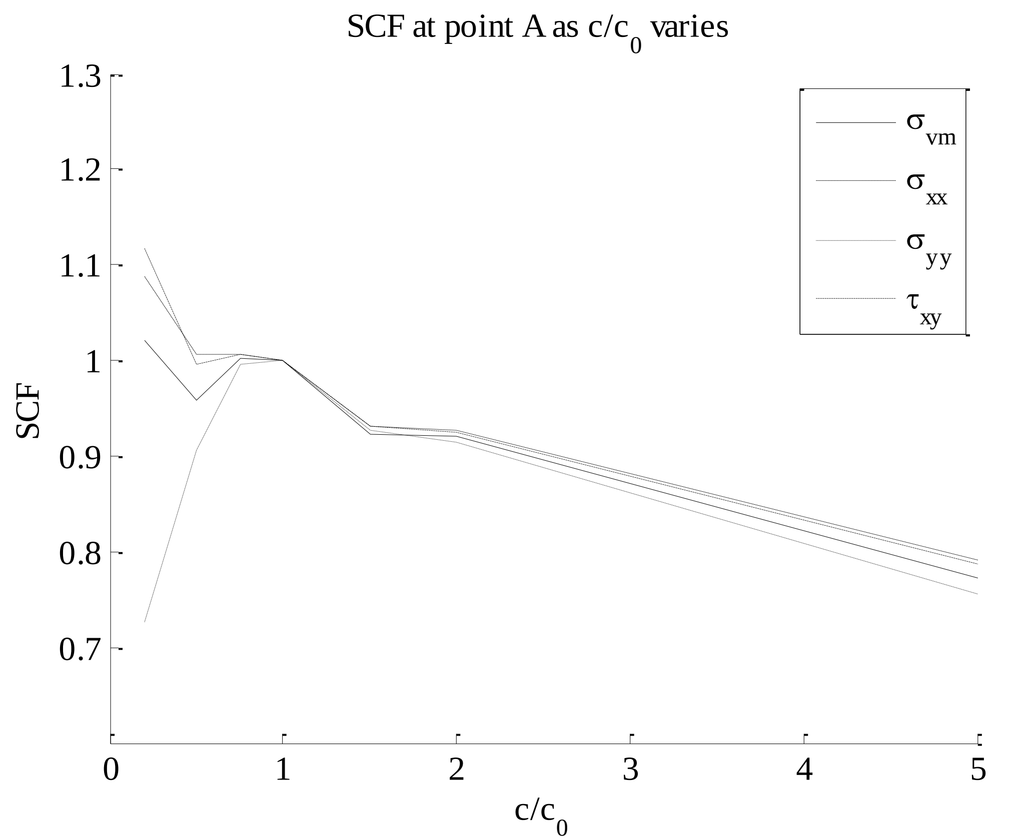

Figure 5.11 SCFs as c/c_0 varies at point *A*

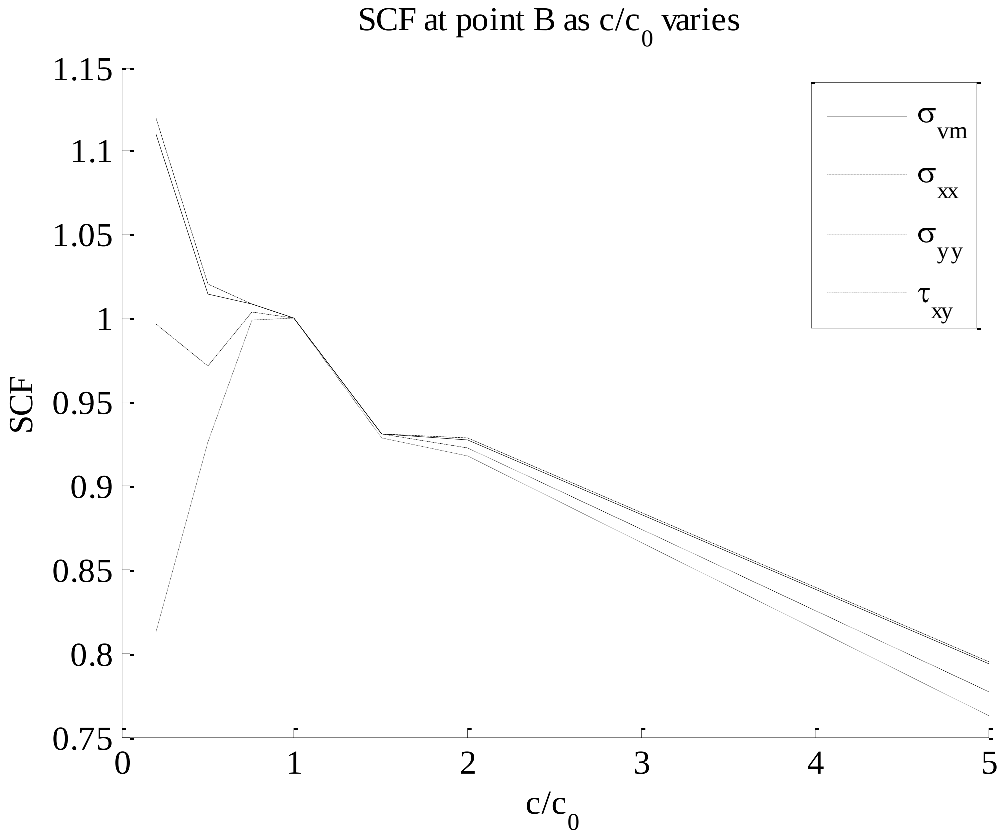

Figure 5.12 SCFs as c/c_0 varies at point *B*

The varied bond length cases behave differently than the previously studied varied parameters. Prior to a ratio of 1.5, they seem erratic. The stresses with the most dramatic variation are X direction stress at point *A* and Y direction stress at point *B*. Following that, however, they seem to universally decrease with increased bond length. Therefore, one should try to maximize bond length in order to minimize overall stress in the single-lap joint.

Bonding length changes effect the SCFs differently than the other varied parameters. For ratios much less than unity, for the geometry used in these simulations, points *A* and *B* begin to affect each other. This is shown in Figures 5.7 and 5.8 by the seemingly strange behavior at ratios less than unity. However, as ratios increase past unity, the two points' stress states become more independent of each other, and stresses universally decrease at each point. This can be attributed to the simple fact that the load is dispersed across a larger amount of material, with a larger cross-sectional area.

5.5 Varied Young's Modulus Under Ideal Bonding and a Three-Point Bending Load

The same important lap joint parameters were also varied under a three-point bending load. Tables 5.9 and 5.10 display the reference stresses and SCFs at points *A* and *B*, while Figures 5.14 and 5.15 graphically present the change in SCF with respect to the ratio of E/E_0. Figure 5.13 highlights the varied parameter and critical points.

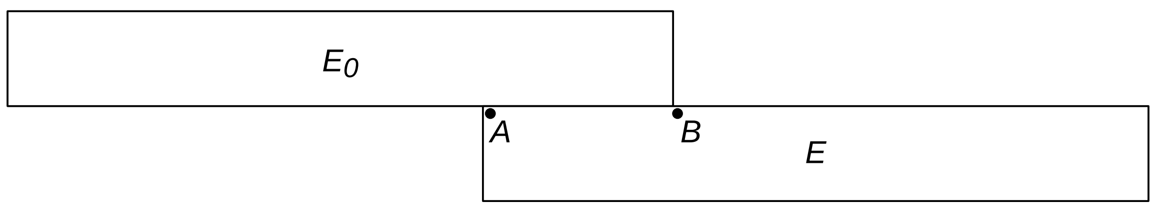

Figure 5.13 Ideally bonded Young's Modulus variation critical points

Table 5.9 Reference stress values and SCFs at point *A* with varying E/E_0

E/E_0	σ_{vm} (SCF)	σ_{xx} (SCF)	σ_{yy} (SCF)	τ_{xy} (SCF)
0.2	17.19 (0.552)	6.057 (0.373)	16.55 (0.605)	-5.352 (0.459)
0.3	20.60 (0.661)	7.95 (0.571)	19.55 (0.714)	-6.579 (0.637)
0.5	25.17 (0.808)	10.99 (0.676)	23.29 (0.851)	-8.486 (0.728)
0.75	28.75 (0.923)	13.92 (0.857)	25.89 (0.946)	-10.33 (0.886)
1.0	31.15 (1.000)	16.25 (1.000)	27.38 (1.000)	-11.66 (1.000)
2.0	36.27 (1.164)	22.56 (1.388)	29.50 (1.077)	-14.68 (1.259)
5.0	42.03 (1.349)	31.29 (1.926)	30.14 (1.101)	-17.77 (1.524)

Table 5.10 Reference stress values and SCFs at point *B* with varying E/E_0

E/E_0	σ_{vm} (SCF)	σ_{xx} (SCF)	σ_{yy} (SCF)	τ_{xy} (SCF)
0.2	126.8 (1.293)	-123.9 (1.263)	-53.98 (0.968)	37.20 (1.451)
0.3	121.35 (1.237)	-118.9 (1.213)	-57.20 (1.026)	34.52 (1.346)
0.5	112.6 (1.148)	-111.0 (1.132)	-59.01 (1.059)	31.49 (1.148)
0.75	104.4 (1.064)	-103.7 (1.058)	-57.94 (1.040)	28.26 (1.102)
1.0	98.10 (1.000)	-98.04 (1.000)	-55.74 (1.000)	25.64 (1.000)
2.0	82.80 (0.844)	-84.24 (0.859)	-46.44 (0.833)	18.86 (0.736)
5.0	66.49 (0.678)	-68.75 (0.701)	-30.79 (0.552)	11.07 (0.432)

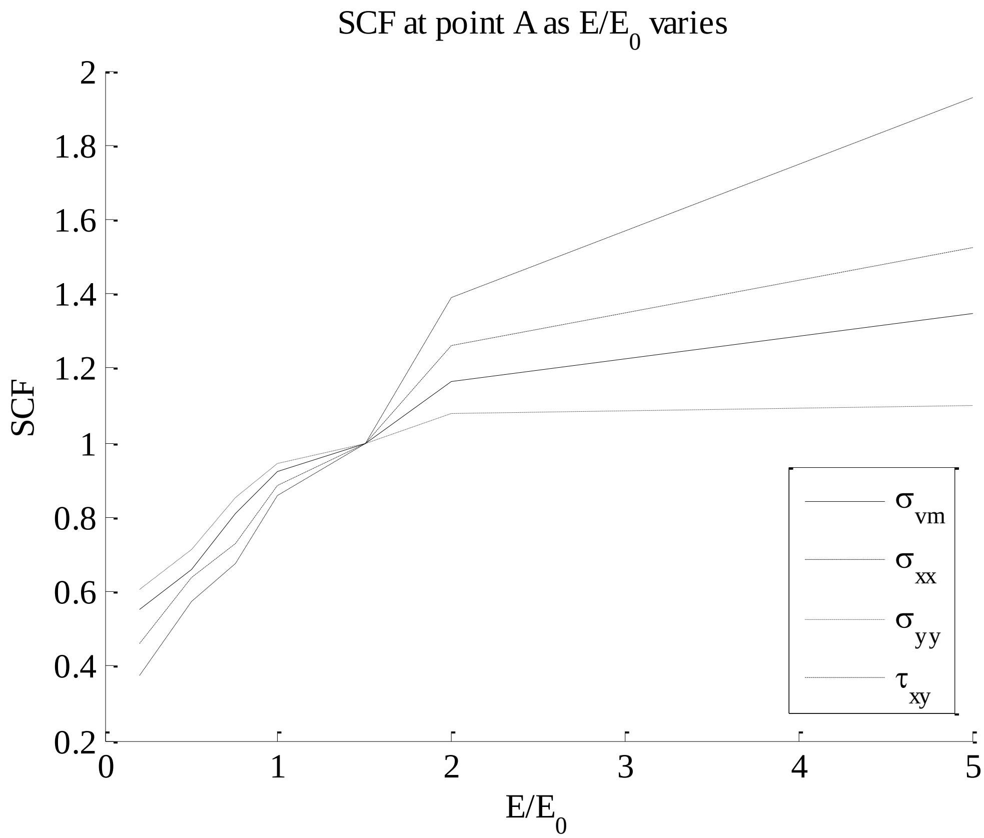

Figure 5.14 SCFs as E/E_0 varies at point *A*

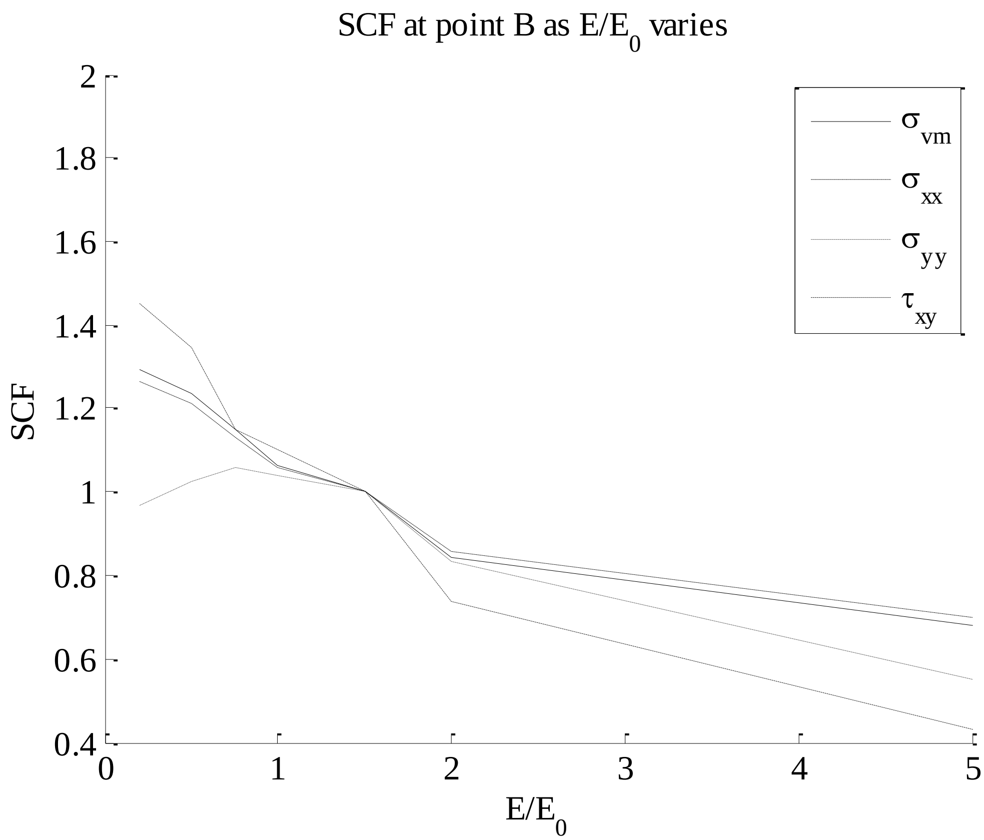

Figure 5.15 SCFs as *E/E₀* varies at point *B*

As can easily be seen, the results from the three-point bending case are very similar in behavior to the tensile case. At point *A*, the SCFs universally increase with an increased ratio of moduli, while at point *B,* they decrease overall. The same conclusion can be drawn as well: one should hold Young's Moduli homogeneous across adherends in order to minimize overall stress.

Under a three-point bending load, the edge moment is much more pronounced. The same Y direction stress phenomena observed under tensile variation of Young's Modulus can be seen in this case at point *B*. And at point *A*, rather than Y direction stress decreasing past unity, it simply levels off. The same logic used to explain stresses under a tensile load can be used here as well, because both three-point bending and tensile loading induce an edge moment on the bond, which has been shown to be the dominant load contributing to stress in single-lap joints.

5.6 Varied Adherend Thickness Under Ideal Bonding and a Three-Point-Bending Load

Tables 5.11 and 5.12 display the reference stress values and associated SCFs for varied t/t_0 and figures 5.17 and 5.18 graphically display the evolving SCFs with respect to varied adherend thickness ratio. Figure 5.16 highlights the varied parameter and critical points.

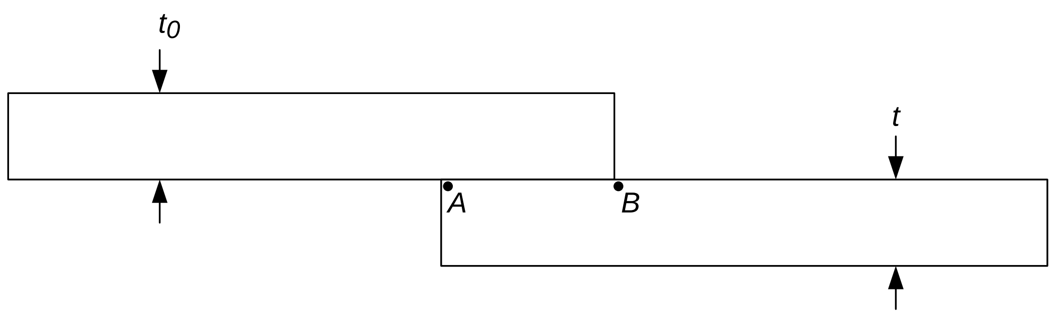

Figure 5.16 Ideally bonded thickness variation critical points

Table 5.11 Reference stress values and SCFs at point *A* with varying t/t_0

t/t_0	σ_{vm} (SCF)	σ_{xx} (SCF)	σ_{yy} (SCF)	τ_{xy} (SCF)
0.2	21.14 (0.679)	-15.25(-0.939)	-11.61(-0.424)	9.331(-0.800)
0.5	22.81 (0.732)	12.53 (0.771)	19.30 (0.705)	-8.956 (0.768)
1.0	31.15 (1.000)	16.25 (1.000)	27.38 (1.000)	-11.66 (1.000)
2.0	24.79 (0.796)	12.07 (0.743)	22.59 (0.825)	-8.752 (0.751)
5.0	10.78 (0.346)	4.764 (0.293)	10.17 (0.371)	-3.527 (0.303)

Table 5.12 Reference stress values and SCFs at point *B* with varying t/t_0

t/t_0	σ_{vm} (SCF)	σ_{xx} (SCF)	σ_{yy} (SCF)	τ_{xy} (SCF)
0.2	1290 (13.150)	-1343 (13.70)	-539.0 (9.670)	242.1 (9.442)
0.5	294.0 (2.997)	-298.0 (3.040)	-154.1 (2.765)	70.65 (2.756)
1.0	98.10 (1.000)	-98.04 (1.000)	-55.74 (1.000)	25.64 (1.000)
2.0	33.39 (0.340)	-33.07 (0.337)	-19.83 (0.356)	9.130 (0.356)
5.0	10.62 (0.123)	-10.32 (0.105)	-7.055 (0.127)	3.151 (0.123)

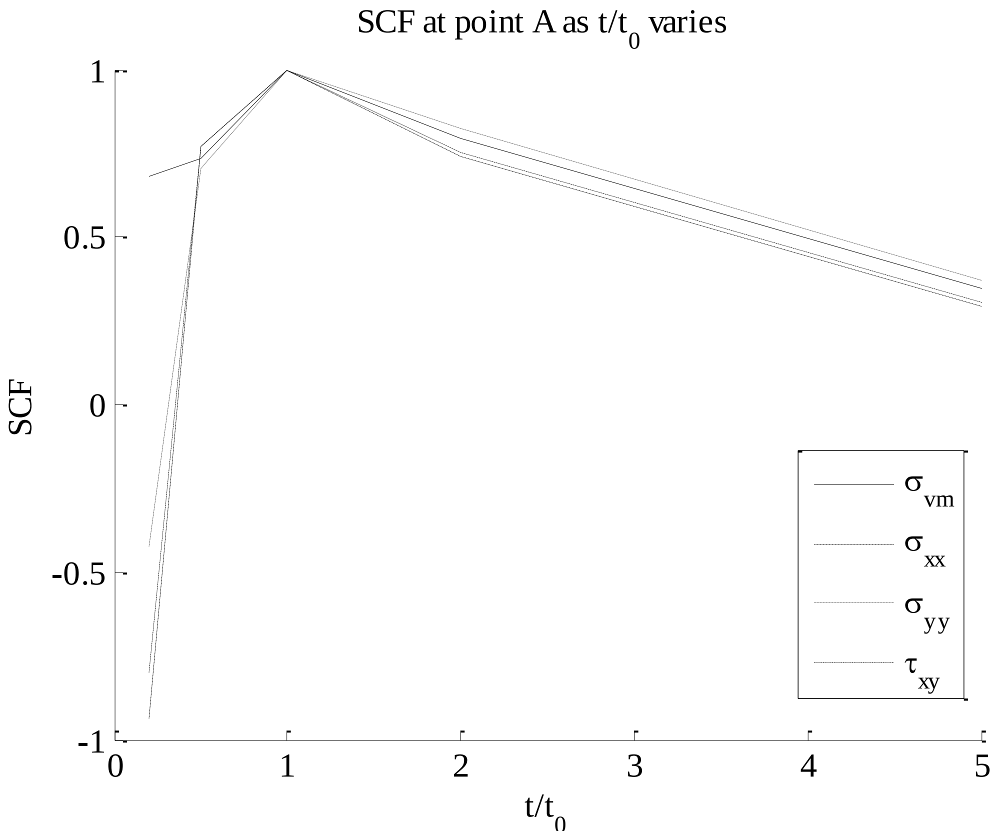

Figure 5.17 SCFs as t/t_0 varies at point *A*

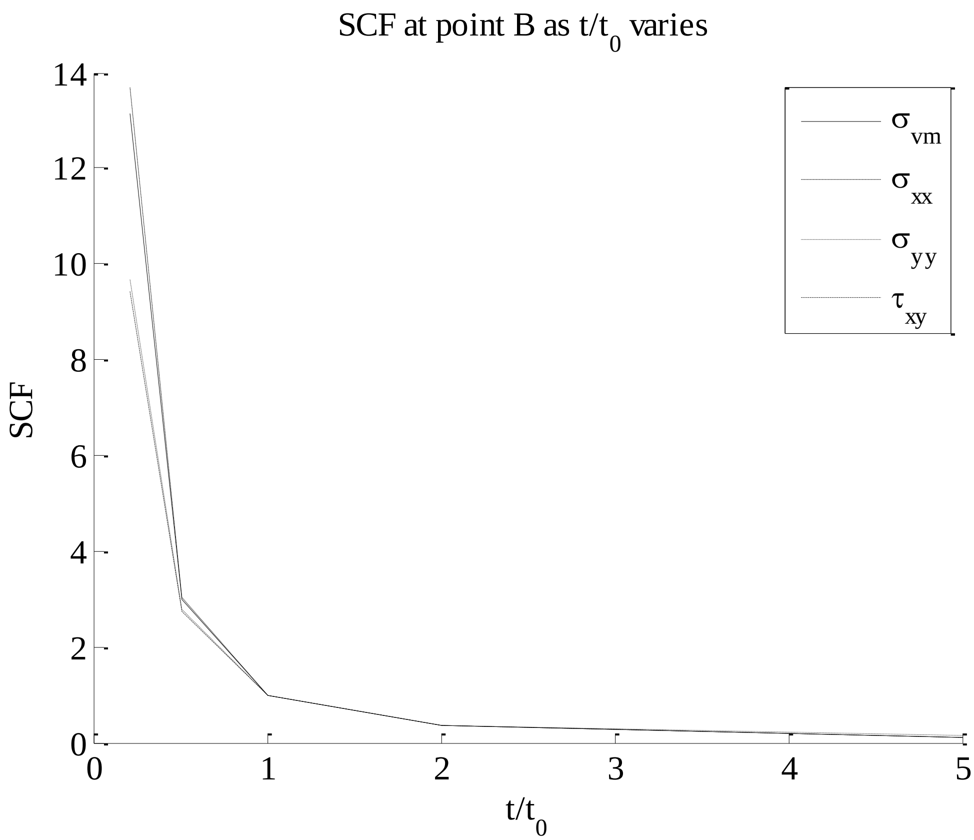

Figure 5.18 SCFs as t/t_0 varies at point *B*

For the three-point bending load cases, varied thickness resulted in different SCF behavior than it did in tension. At point *A*, the SCFs increased up to a ratio of unity, and then decreased, while at point *B*, they universally decreased. However, this does not mean that one should maximize thickness. The SCFs of a ratio of less than unity, at least at point *B*, still suggest one should keep a ratio of unity, as any nonhomogeneity would increase the stress in the adherend with the smallest thickness. Also, the changing thickness greatly changes the stiffness and moment of inertia of the varied adherend, resulting in a much different state of stress at the lower ratios.

The apparent odd behavior of stresses at point *A* can be explained by the fact that stresses simply changed direction as compared to the other cases. This is indicated by the negative SCFs. Von Mises stress, being always positive, shows the general stress behavior regardless of sign, and they fit the general trend at point *A*. Stress there increases up to a ratio of unity, and then decrease. However, it is apparent from the SCFs that stresses at point *B* are much more critical, with SCFs reaching over 13. They decrease as thickness increases because of the increased cross-sectional area and moment of inertia. The behavior of stresses at point *A* for ratios less than unity is quite apparently attributable to a shift from tensile to more compressive stresses. The compressive stresses are still of appreciable magnitude at point *A*, and can be considered to increase in compressive strength, just as point *B* increases in tensile strength, for ratios less than unity.

5.7 Varied Free Adherend Length Under Ideal Bonding and a Three-Point-Bending Load

Varied length was also investigated under three point bending. Tables 5.13 and 5.14 display reference stress values and their associated SCFs, while Figures 5.20 and 5.21 graphically track the changing SCFs with respect to the ratio L/L_0. Figure 5.19 highlights the varied parameter and critical points.

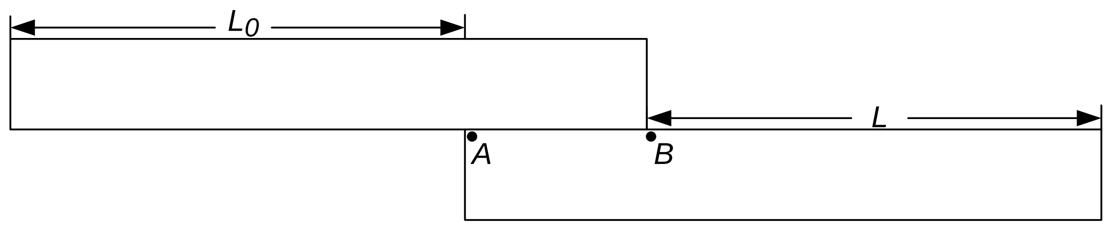

Figure 5.19 Ideally bonded free adherend length variation critical points

Table 5.13 Reference stress values and SCFs at point *A* with varying L/L_0

L/L_0	σ_{vm} (SCF)	σ_{xx} (SCF)	σ_{yy} (SCF)	τ_{xy} (SCF)
0.2	4.171 (0.134)	2.127 (0.131)	3.705 (0.135)	-1.537 (0.132)
0.5	13.12 (0.421)	6.691 (0.412)	11.66 (0.426)	-4.830 (0.414)
1.0	31.15 (1.000)	16.25 (1.000)	27.38 (1.000)	-11.66 (1.000)
2.0	49.88 (1.601)	26.65 (1.640)	43.30 (1.581)	-18.98 (1.628)
5.0	99.47 (3.193)	55.34 (3.406)	84.35 (3.081)	-38.96 (3.341)

Table 5.14 Reference stress values and SCFs at point *B* with varying L/L_0

L/L_0	σ_{vm} (SCF)	σ_{xx} (SCF)	σ_{yy} (SCF)	τ_{xy} (SCF)
0.2	0.069 (7E-4)	-0.024 (2E-4)	0.056 (-0.001)	2E-4 (1E-4)
0.5	38.42 (0.392)	-38.16 (0.389)	-22.80 (0.409)	10.37 (0.404)
1.0	98.10 (1.000)	-98.04 (1.000)	-55.74 (1.000)	25.64 (1.000)
2.0	136.0 (1.386)	-136.0 (1.387)	-76.96 (1.381)	35.39 (1.381)
5.0	174.1 (1.775)	-174.0 (1.775)	-99.59 (1.787)	45.50 (1.775)

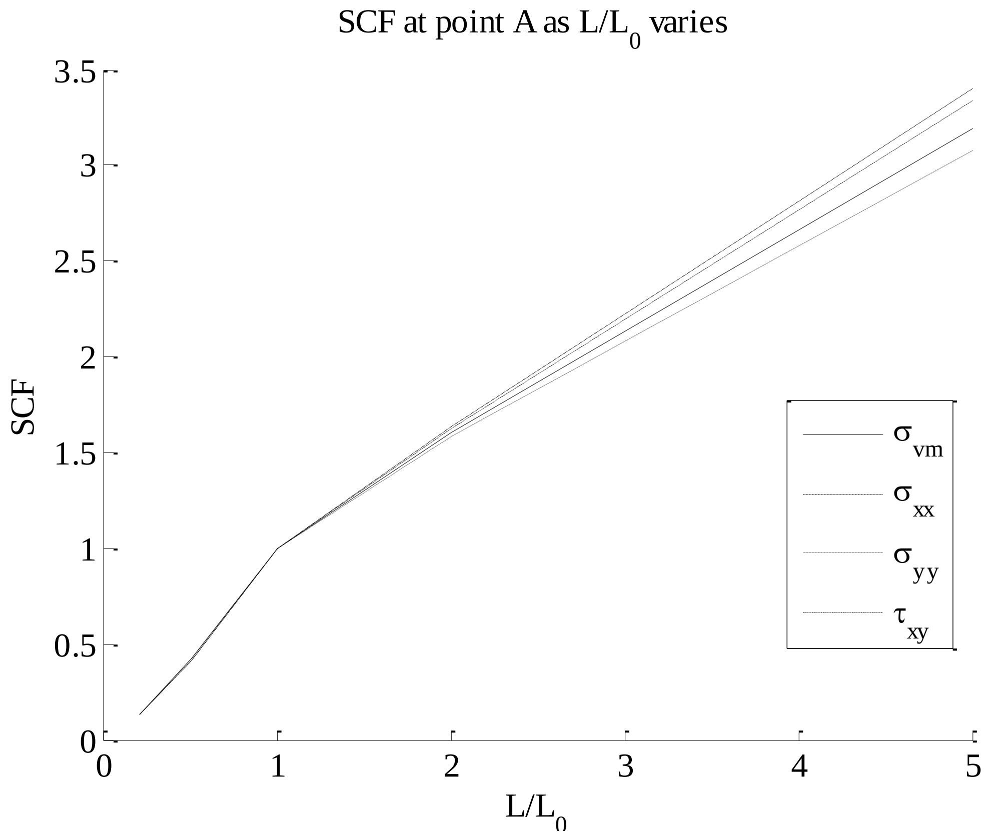

Figure 5.20 SCFs as L/L_0 varies at point *A*

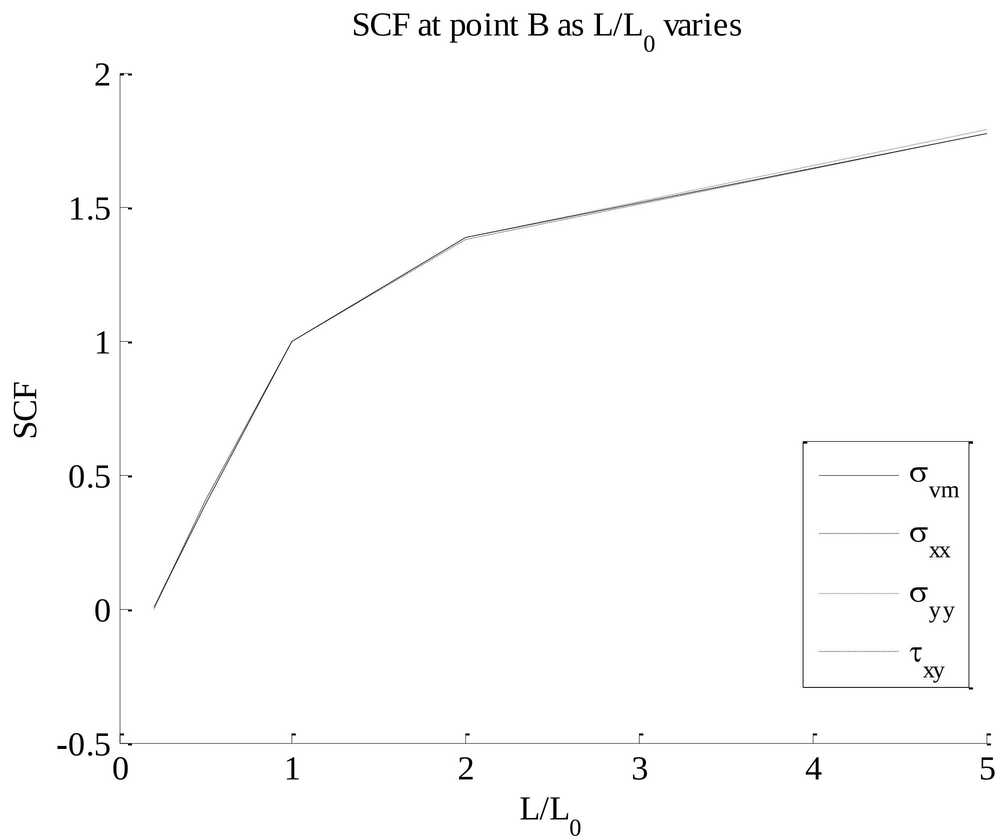

Figure 5.21 SCFs as *L/L_0* varies at point *B*

As is immediately apparent, with increased *L*, all SCFs universally increase. This is an intuitive response as three-point bending induces a large edge moment, and increased length increases the moment arm, therefore increasing the stress.

This behavior is easy to explain. As free adherend length is increased, the moment arm is increased, and therefore stresses at *A* and *B* are increased across the board.

5.8 Varied Bonding Length Under Ideal Bonding and a Three-Point-Bending Load

Bond length was then investigated. Tables 5.15 and 5.16 present reference stress values and SCFs as bond length varies, and figure 5.23 and 5.24 graphically track varying SCFs with varying bond length. Figure 5.22 highlights the varied parameter and critical points.

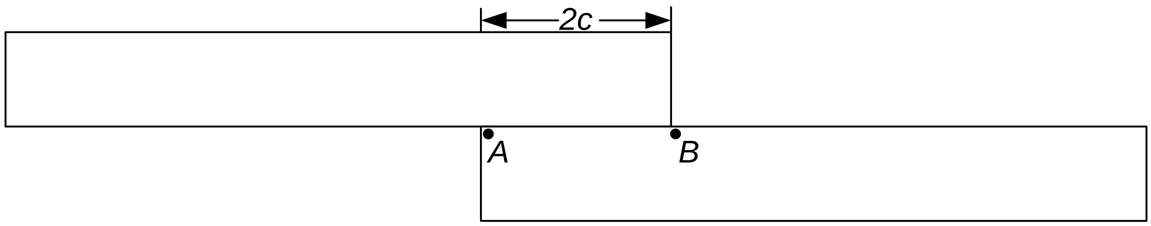

Figure 5.22 Ideally bonded bonding length variation critical points

Table 5.15 Reference stress values and SCFs at point *A* with varying c/c_0

c/c_0	σ_{vm} (SCF)	σ_{xx} (SCF)	σ_{yy} (SCF)	τ_{xy} (SCF)
0.2	151.9 (4.876)	45.27 (2.786)	153.7 (5.614)	-36.87 (3.162)
0.5	43.81 (1.406)	19.80 (1.219)	40.97 (1.496)	-14.64 (1.256)
1.0	31.15 (1.000)	16.25 (1.000)	27.38 (1.000)	-11.66 (1.000)
2.0	29.52 (0.947)	15.37 (0.946)	25.96 (0.948)	-11.03 (0.946)
5.0	31.29 (1.005)	16.18 (0.996)	27.62 (1.009)	-11.64 (0.998)

Table 5.16 Reference stress values and SCFs at point *B* with varying c/c_0

c/c_0	σ_{vm} (SCF)	σ_{xx} (SCF)	σ_{yy} (SCF)	τ_{xy} (SCF)
0.2	182.8 (1.863)	-170.5 (1.739)	-161.1 (2.890)	61.55 (2.401)
0.5	111.9 (1.141)	-111.2 (1.134)	-67.95 (1.219)	30.29 (1.181)
1.0	98.10 (1.000)	-98.04 (1.000)	-55.74 (1.000)	25.64 (1.000)
2.0	89.81 (0.916)	-89.74 (0.915)	-51.13 (0.917)	23.49 (0.916)
5.0	91.81 (0.936)	-91.79 (0.936)	-51.91 (0.931)	23.92 (0.933)

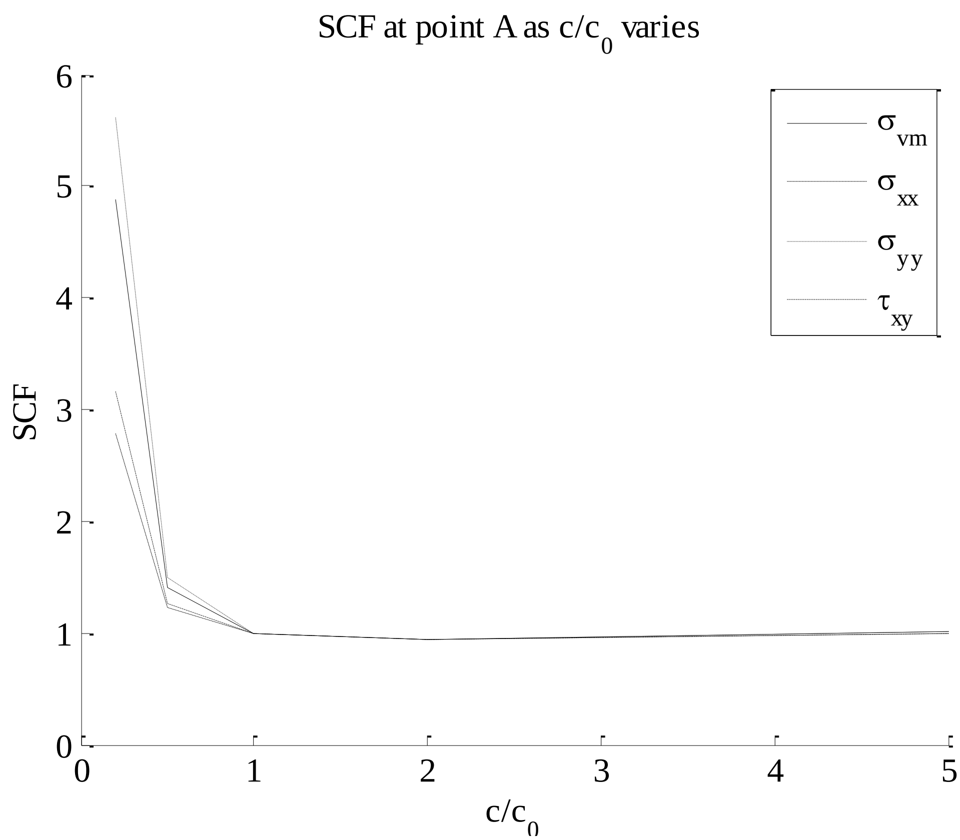

Figure 5.23 SCFs as c/c_0 varies at point *A*

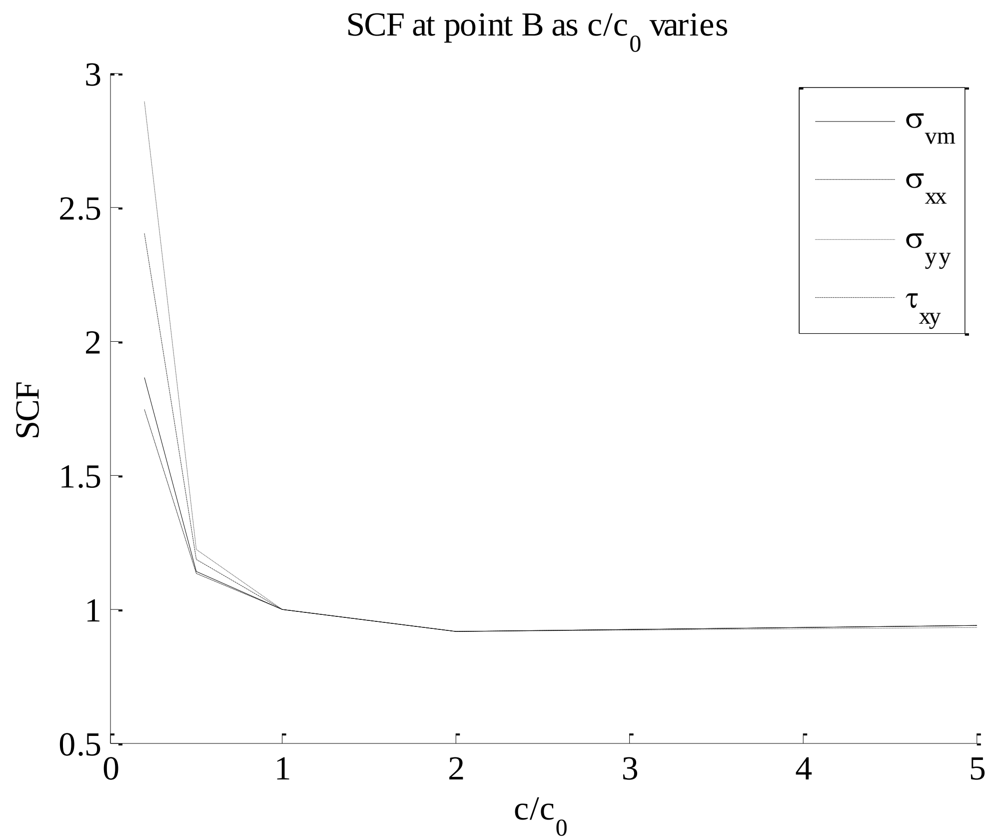

Figure 5.24 SCFs as c/c_0 varies at point *B*

As is immediately apparent an obvious and intuitive, all stresses universally decrease with increasing bond length. Increasing bond length essentially increases the thickness of the central of the single-lap joint, which is most effected by the bending moment imparted by the three point bending load. With a higher thickness, and therefore a higher moment of inertia, the stresses decrease.

Varied bond length stress behavior is also very easy to explain. The cross-sectional area and moment of inertia of the bonded region is increased as bonding length is increased, and therefore, stresses due to the dominant moment are decreased universally.

5.9 Varied Adhesive Thickness Under Adhesive Bonding and a Tensile Load

While ideal bonding cases are important to understand the behavior of the adherends under common loading cases, it is important to understand how the adhesive used in bonding real-world single-lap joints effect the adherends as well. Figure 5.25 displays a diagram of the boundary conditions and additional parameters involved in the adhesively bonded single-lap joint parametric study.

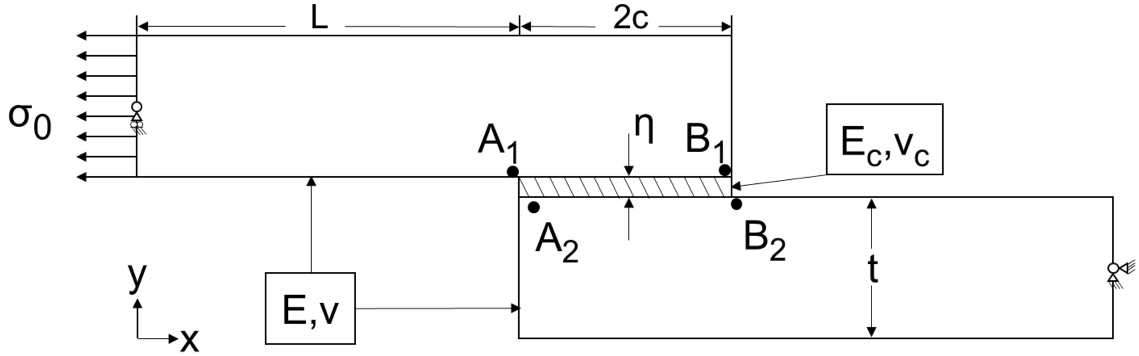

Figure 5.25 Finite element boundary conditions and parameters

First, adhesive thickness was studied using the original tensile basic case's dimensions and properties. Base adhesive thickness was 0.1 m. E_c and v_c were 28 GPa and 0.4 respectively, which is considered a moderately stiff adhesive. Tables 5.17 and 5.18 display the reference stress values and their associated SCFs as adhesive thickness was varied, and Figures 5.27 and 5.28, graphically illustrate the changing SCFs with respect to η/η_0 at points A_1 and B_2, the critical points on each adherend displayed in Figure 5.17.

Points A_2 and B_1 are shown in the following section to always be less critical than those at points A_1 and B_2**.** Figure 5.26 highlights the varied parameter and critical points.

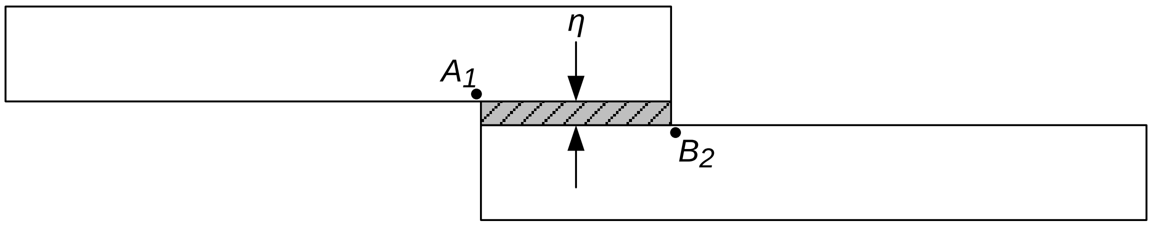

Figure 5.26 Adhesively bonded adhesive thickness variation critical points

Table 5.17 Stress values and SCFs as η/η_0 varies at point A_1

η/η_0	σ_{vm} (SCF)	σ_{xx} (SCF)	σ_{yy} (SCF)	τ_{xy} (SCF)
0.2	7.323 (0.942)	7.370 (0.943)	3.795 (0.932)	-1.819 (0.937)
0.5	7.491 (0.964)	7.538 (0.964)	3.899 (0.958)	-1.866 (0.961)
1.0	7.772 (1.000)	7.817 (1.000)	4.072 (1.000)	-1.942 (1.000)
2.0	8.332 (1.072)	8.374 (1.071)	4.417 (1.085)	-2.095 (1.079)
5.0	10.01 (1.288)	10.04 (1.284)	5.448 (1.338)	-2.552 (1.314)

Table 5.18 Stress values and SCFs as η/η_0 varies at point B_2

η/η_0	σ_{vm} (SCF)	σ_{xx} (SCF)	σ_{yy} (SCF)	τ_{xy} (SCF)
0.2	7.323 (0.942)	7.370 (0.943)	3.795 (0.932)	-1.819 (0.937)
0.5	7.491 (0.964)	7.538 (0.964)	3.899 (0.958)	-1.866 (0.961)
1.0	7.772 (1.000)	7.817 (1.000)	4.072 (1.000)	-1.942 (1.000)
2.0	8.332 (1.072)	8.374 (1.071)	4.417 (1.085)	-2.095 (1.079)
5.0	10.01 (1.288)	10.04 (1.284)	5.448 (1.338)	-2.552 (1.314)

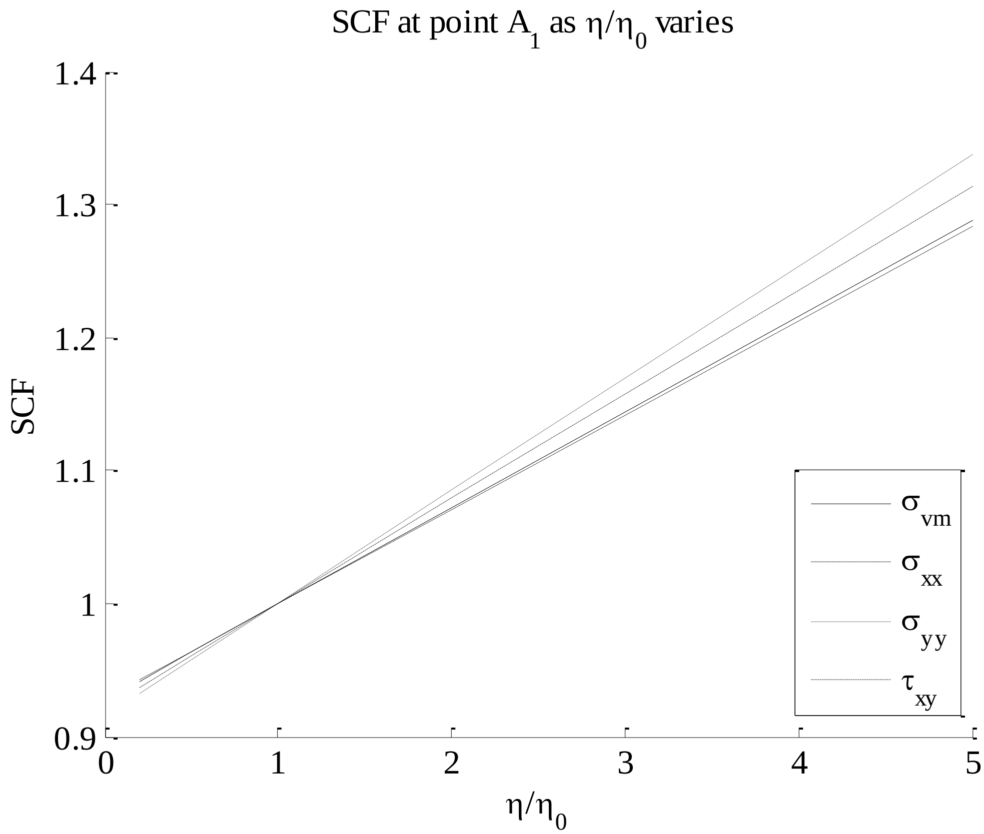

Figure 5.27 SCFs as *η/η_0* varies at point *A_1*

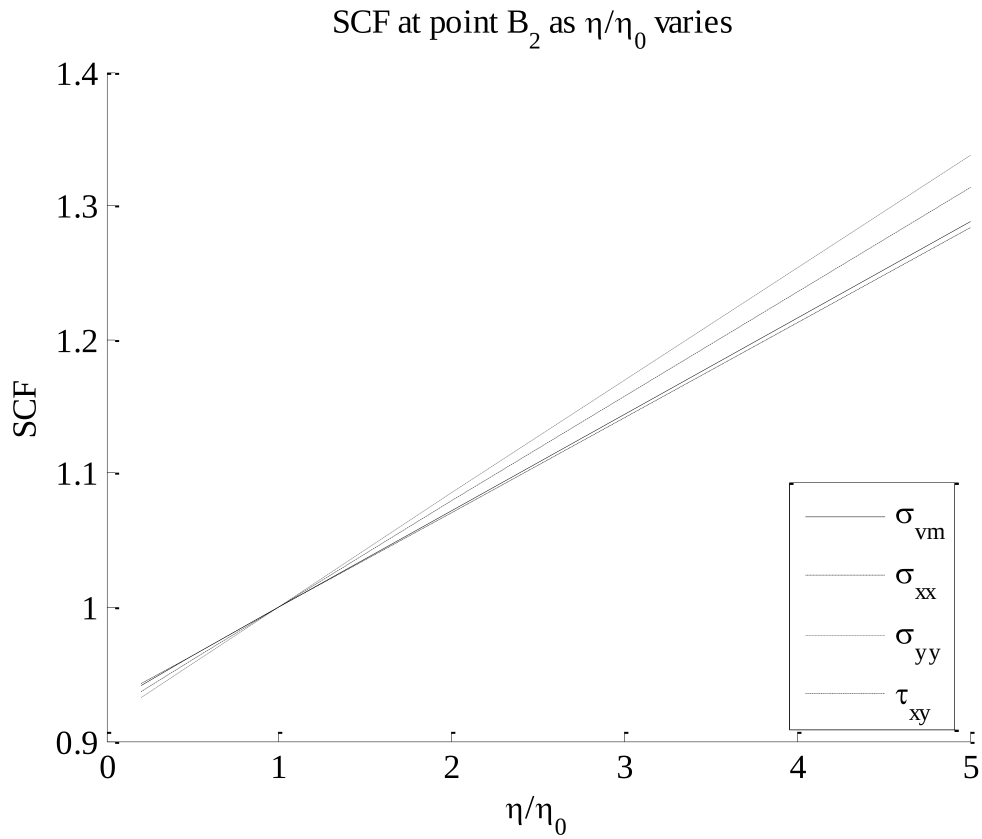

Figure 5.28 SCFs as η/η_0 varies at point B_2

As adhesive thickness increases, the stresses at points A_1 and B_2 universally increase. This is easily explainable, and is attributed to the increased eccentricity of the loading angle, thereby increasing the edge moment force on the bonded region.

5.10 Varied Young's Modulus Under Adhesive Bonding and a Tensile Load

In order to study adhesive effects on a single-lap joint with dimensions similar to that of the experimental analysis in chapter six, the dimensions were changed to 6.35 mm by 155.575 mm adherends with a bonding length of 38.1 mm. The single-lap joints studied prior to this were of a different ratio of length to thickness, and therefore behave slightly differently. Young's Modulus and Poisson's Ratio are still 70 GPa and 0.3 respectively for the adherends, and are still 28 GPa and 0.4 respectively for the adhesive. A unit input stress was also applied, in order to keep the resulting stresses normalized with respect to its input.

For the purpose of comparing this geometry with ideal bonding with that of adhesive bonding, Table 5.21 displays the various stresses at the critical points on each adherend without any adhesive and with ideal bonding, and Table 5.22 displays the various stresses at each of the critical points with the aforementioned adhesive added, and their SCF with respect to the values in Table 5.21.

Table 5.19 Stress values of the basic model without any adhesive

	A_1	B_1	A_2	B_2
σ_{vm}	5.798	4.309	4.310	5.798
σ_{xx}	7.150	2.923	2.923	7.150
σ_{yy}	2.791	3.842	3.842	2.740
σ_{xy}	-2.037	-2.317	-2.317	-2.037

Table 5.20 Stress values of the basic model with adhesive, SCFs compared to table 1

	A_1	B_1	A_2	B_2
σ_{vm} (SCF)	2.712 (0.367)	0.876 (0.203)	0.876 (0.203)	2.712 (0.367)
σ_{xx} (SCF)	3.376 (0.472)	0.561 (0.192)	0.561 (0.192)	3.376 (0.472)
σ_{yy} (SCF)	1.311 (0.470)	0.618 (0.161)	0.618 (0.161)	1.311 (0.470)
σ_{xy} (SCF)	-0.842 (0.413)	-0.473 (0.147)	-0.473 (0.147)	-0.842 (0.413)

As is immediately apparent, the addition of the adhesive increases the stresses across the board, if it changes them at all. Most notably, shear stress is increased significantly at points A_1 and A_2. However, the stresses at points A_1 and B_2 are always much higher than at the other two points. Therefore, only these two critical points will be investigated.

Following this initial comparison, adherend Young's Modulus was once again varied. Tables 5.23, and 5.24 tabulate the stresses and associated SCFs with the variation, and Figures 5.30, and 5.31 plot SCFs at each respective critical point as Young's Modulus is varied. Figure 5.29 highlights the varied parameter and critical points.

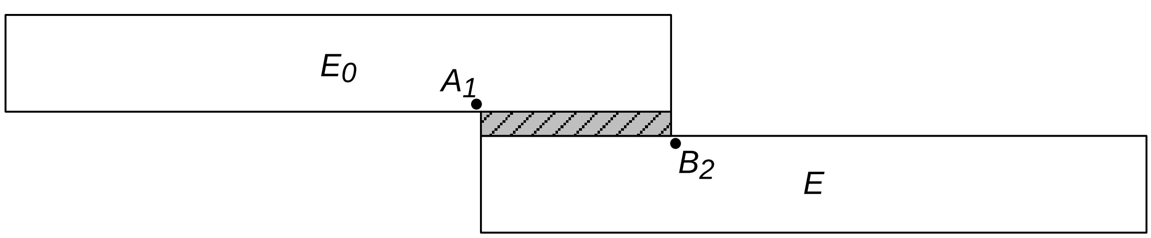

Figure 5.29 Adhesively bonded Young's Modulus variation critical points

Table 5.21 Stresses and SCFS at point A_1 as E/E_0 varies

E/E_0	σ_{vm} (SCF)	σ_{xx} (SCF)	σ_{yy} (SCF)	σ_{xy} (SCF)
0.2	3.919 (0.946)	4.970 (0.948)	1.317 (0.779)	-0.882 (0.803)
0.5	4.044 (0.976)	5.131 (0.979)	1.595 (0.944)	-1.026 (0.934)
1	4.143 (1.000)	5.241 (1.000)	1.689 (1.000)	-1.098 (1.000)
2	4.225 (1.020)	5.324 (1.016)	1.675 (0.992)	-1.133 (1.032)
5	4.303 (1.039)	5.394 (1.029)	1.543 (0.914)	-1.140 (1.038)

Table 5.22 Stresses and SCFS at point B_2 as E/E_0 varies

E/E_0	σ_{vm} (SCF)	σ_{xx} (SCF)	σ_{yy} (SCF)	σ_{xy} (SCF)
0.2	5.049 (1.216)	6.159 (1.171)	1.738 (1.050)	-1.667 (1.492)
0.5	4.560 (1.098)	5.709 (1.086)	1.757 (1.061)	-1.408 (1.261)
1	4.153 (1.000)	5.259 (1.000)	1.656 (1.000)	-1.117 (1.000)
2	3.812 (0.918)	4.820 (0.917)	1.376 (0.831)	-0.822 (0.735)
5	3.515 (0.847)	4.352 (0.827)	0.926 (0.559)	-0.500 (0.448)

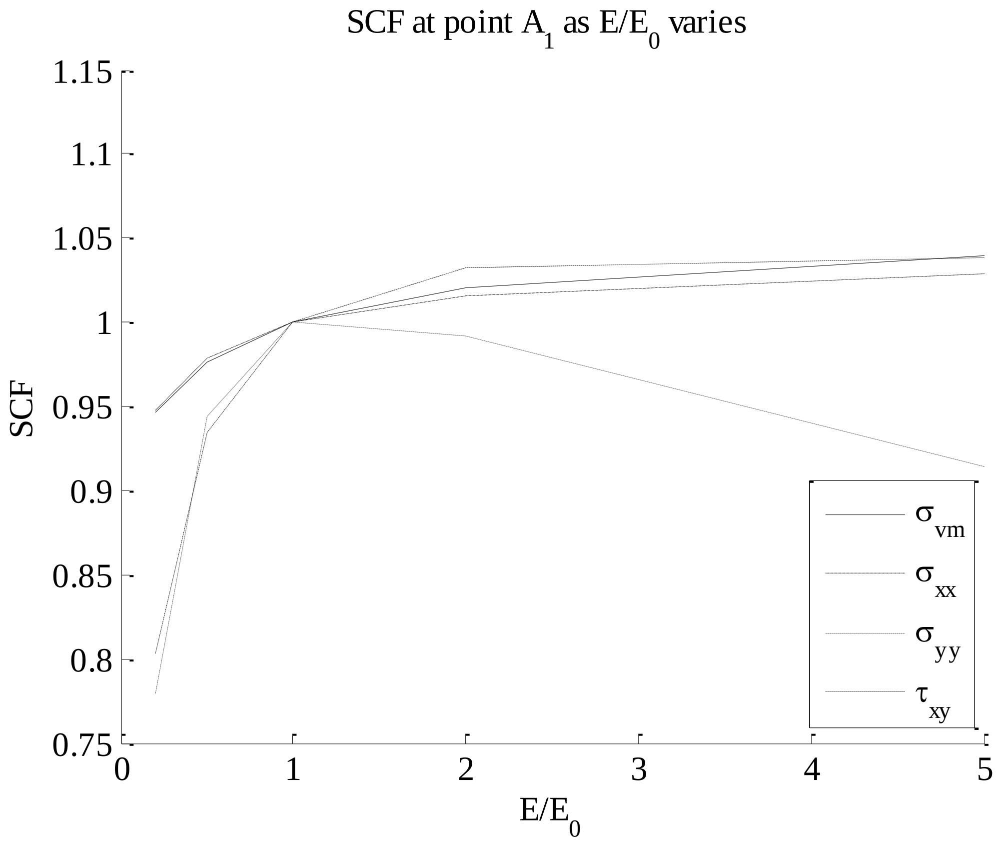

Figure 5.30 SCF at point *A_1* as *E/E_0* varies

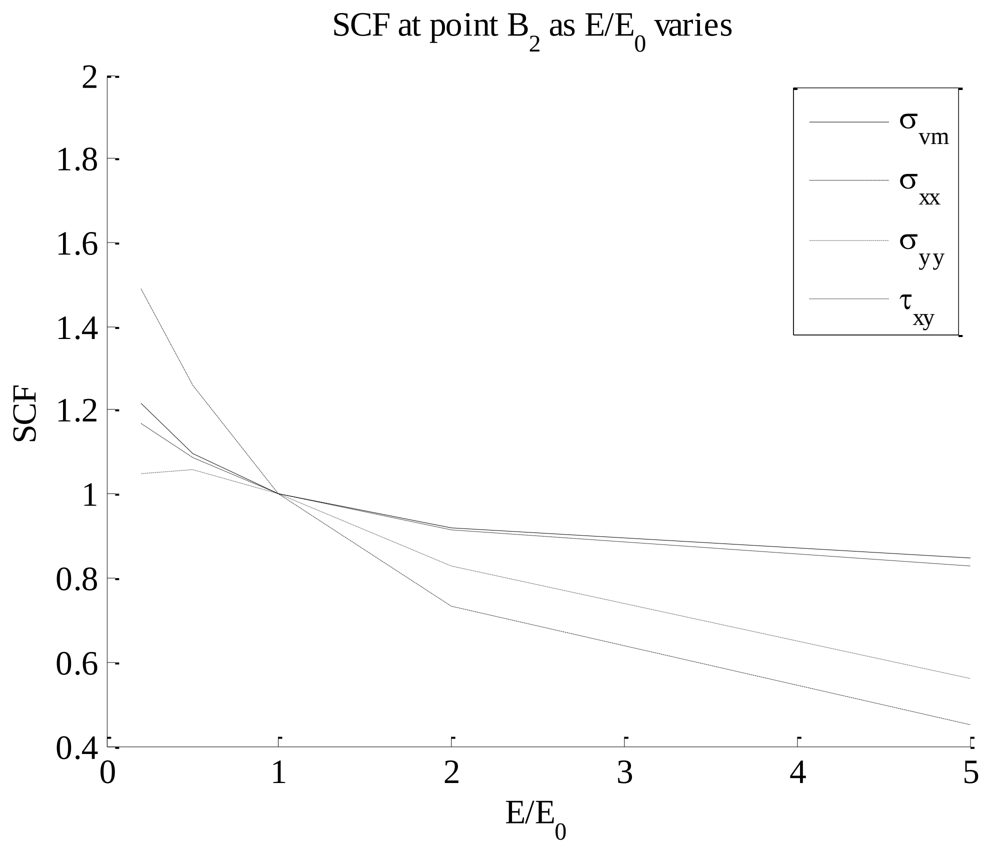

Figure 5.31 SCF at point B_2 as E/E_0 varies

Varying Young's Modulus on this single-lap joint with moderate length adherends has some interesting effects on the stresses at its critical points. Point A_1 follows the same trends in Y direction stress and all other stresses, and point B_2 follows the Y direction stress trend and all other stresses as the case with no adhesive, only with less magnitude. This is due to the addition of the adhesive, and its ability to hold some of the stress that was previously transferred directly from on adherend to the other.

5.11 Varied Adherend Thickness Under Adhesive Bonding and a Tensile Load

Tables 5.27, and 5.28 display the reference stress values and SCFs associated with varied adherend thickness, and Figures 5.33, and 5.34 plot the SCF versus the varying thickness ratio. Figure 5.32 highlights the varied parameter and critical points.

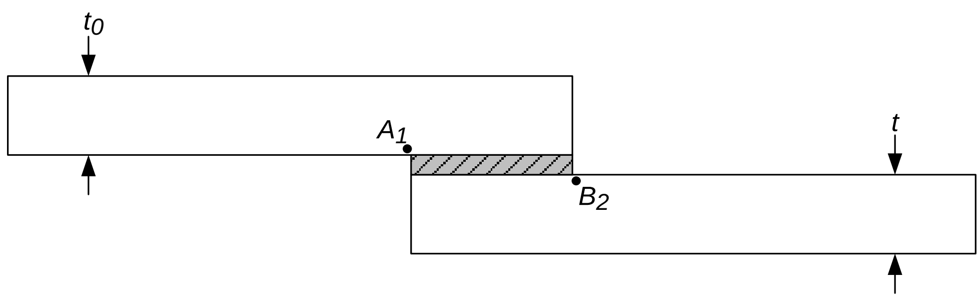

Figure 5.32 Adhesively bonded adherend thickness variation critical points

Table 5.23 Stresses and SCFS at point A_1 as t/t_0 varies

t/t_0	σ_{vm} (SCF)	σ_{xx} (SCF)	σ_{yy} (SCF)	σ_{xy} (SCF)
0.2	3.565 (0.861)	4.488 (0.856)	1.029 (0.609)	-0.771 (0.702)
0.5	3.523 (0.850)	4.449 (0.849)	1.289 (0.763)	-0.880 (0.802)
1	4.143 (1.000)	5.241 (1.000)	1.689 (1.000)	-1.098 (1.000)
2	5.553 (1.340)	7.031 (1.342)	2.450 (1.450)	-1.534 (1.398)
5	9.838 (2.374)	12.46 (2.379)	4.728 (2.799)	-2.847 (2.593)

Table 5.24 Stresses and SCFS at point B_2 as t/t_0 varies

t/t_0	σ_{vm} (SCF)	σ_{xx} (SCF)	σ_{yy} (SCF)	σ_{xy} (SCF)
0.2	19.93 (4.799)	23.68 (4.503)	4.118 (2.487)	-2.531 (2.266)
0.5	8.956 (2.157)	11.47 (2.181)	2.938 (1.773)	-2.022 (1.810)
1	4.153 (1.000)	5.259 (1.000)	1.656 (1.000)	-1.117 (1.000)
2	2.121(0.511)	2.661 (0.506)	0.933 (0.564)	-0.632 (0.566)
5	0.922 (0.222)	1.149 (0.218)	0.420 (0.253)	-0.285 (0.256)

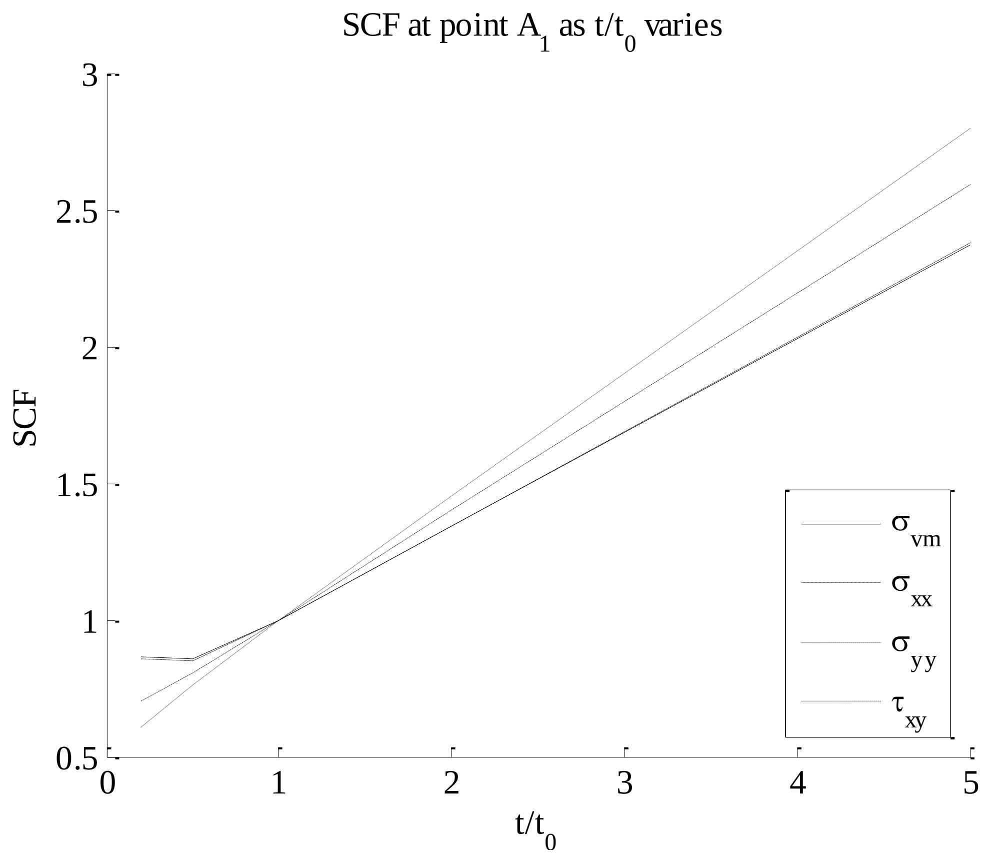

Figure 5.33 SCF at point A_1 as t/t_0 varies

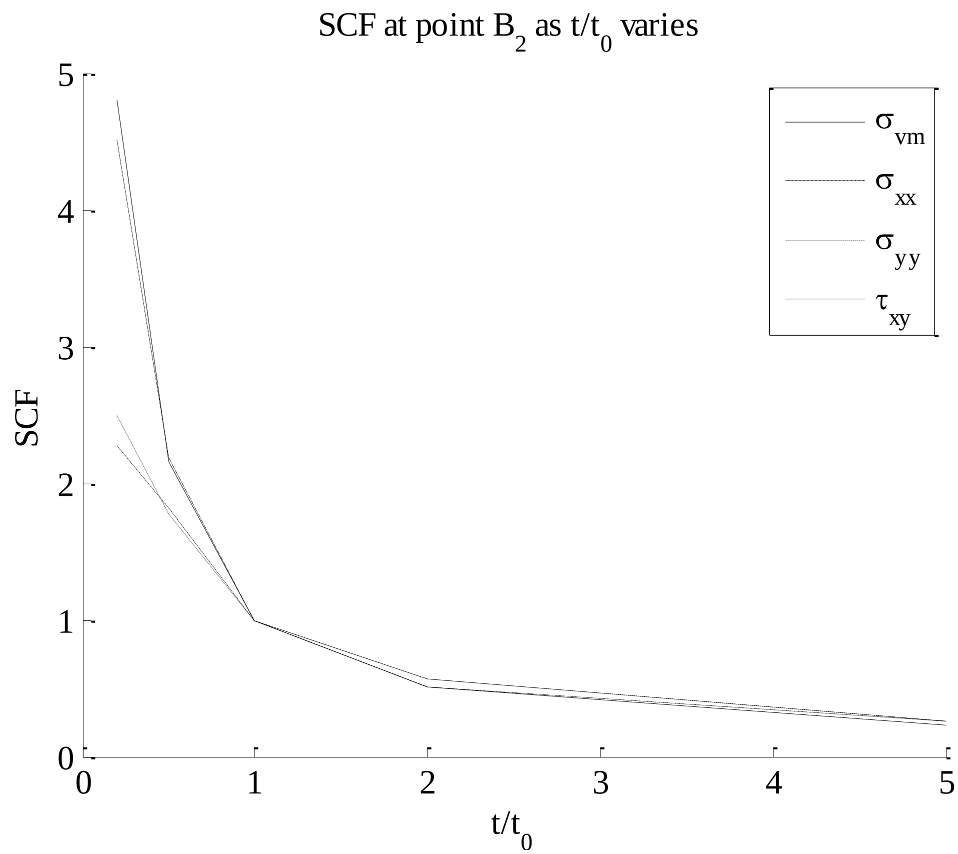

Figure 5.34 SCF at point B_2 as t/t_0 varies

With varied adherend thickness, the SCFs at point A_1 increase and at point B_2 decrease as t/t_0 increases, exhibiting the same behavior as in the ideally bonded case. The same explanation holds.

5.12 Varied Adhesive Young's Modulus Under Adhesive Bonding and a Tensile Load

Tables 5.26, and 5.27display the stresses and SCFs associated with varied adhesive Young's Modulus, and Figures 5.36, and 5.37 plot the changing SCF as adhesive Young's Modulus changes. Figure 5.35 highlights the varied parameter and critical points.

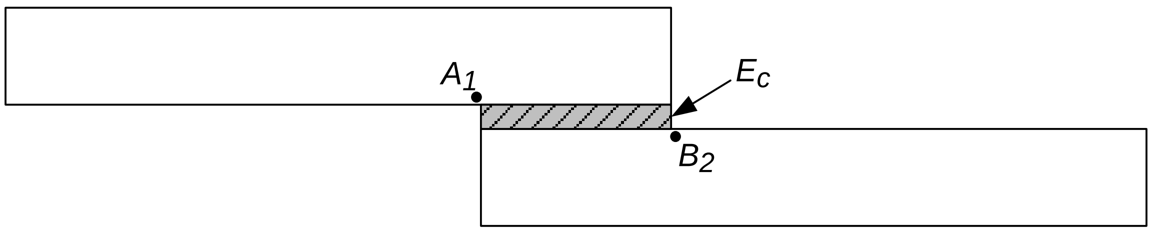

Figure 5.35 Adhesively bonded adhesive Young's Modulus variation critical points

Table 5.25 Stresses and SCFS at point A_1 as E_c/E_{c0} varies

E_c/E_{c0}	σ_{vm} (SCF)	σ_{xx} (SCF)	σ_{yy} (SCF)	σ_{xy} (SCF)
0.2	3.632 (0.877)	4.512 (0.861)	1.104 (0.654)	-0.600 (0.547)
0.5	3.883 (0.937)	4.897 (0.934)	1.463 (0.937)	-0.861 (0.785)
1	4.143 (1.000)	5.241 (1.000)	1.689 (1.000)	-1.098 (1.000)
2	4.467 (1.078)	5.617 (1.072)	1.811 (1.072)	-1.351 (1.231)
5	4.966 (1.199)	6.125 (1.169)	1.831 (1.084)	-1.664 (1.515)

Table 5.26 Stresses and SCFS at point B_2 as E_c/E_{c0} varies

E_c/E_{c0}	σ_{vm} (SCF)	σ_{xx} (SCF)	σ_{yy} (SCF)	σ_{xy} (SCF)
0.2	3.633 (0.875)	4.523 (0.860)	1.086 (0.656)	-0.612 (0.548)
0.5	3.888 (0.936)	4.912 (0.934)	1.437 (0.867)	-0.877 (0.785)
1	4.153 (1.000)	5.259 (1.000)	1.656 (1.000)	-1.117 (1.000)
2	4.480 (1.079)	5.636 (1.071)	1.774 (1.071)	-1.371 (1.228)
5	4.980 (1.199)	6.140 (1.167)	1.852 (1.118)	-1.679 (1.503)

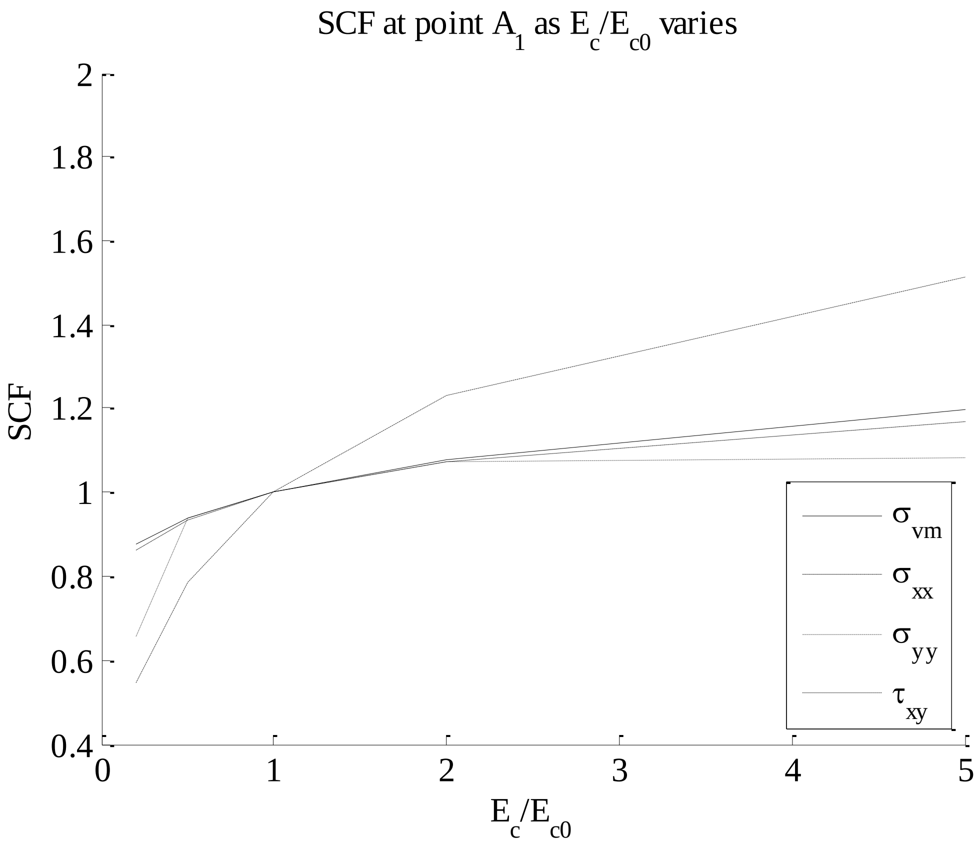

Figure 5.36 SCF at point A_1 as E_c/E_{c0} varies

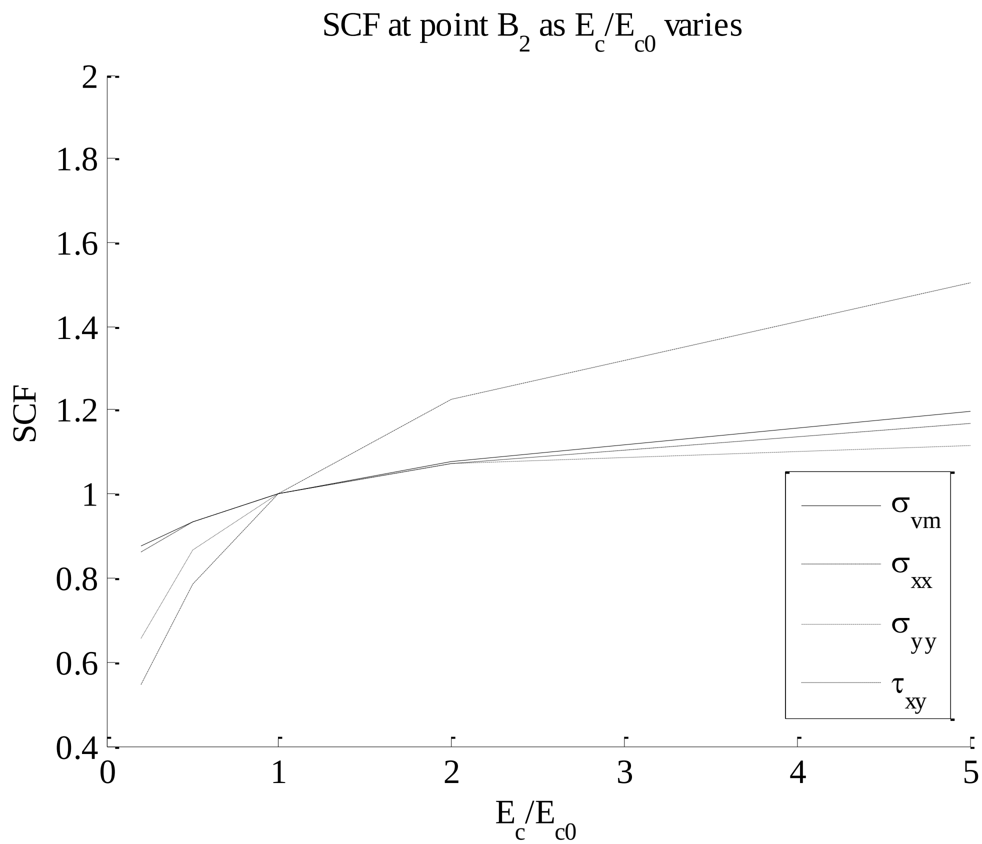

Figure 5.37 SCF at point B_2 as E_c/E_{c0} varies

As far as adherend stress is concerned, it is clear that the smallest adhesive Young's Modulus is best. Stresses at both critical points increase in intensity as the Young's Modulus of the adhesive increases, which is to be expected. A stiffer adhesive causes more deformation and stress in the adherends.

5.13 Design Recommendations via Parametric Study

With a basic understanding of the effect each individual parameter has on the stresses in the single-lap joint, one can develop recommendations concerning single-lap joint design. Of course, the ideally bonded cases shed little light on "real world" lap joints, but the corresponding cases simulated with an adhesive often held similar results, so design recommendations based on the ideally bonded cases would be identical to those based on the adhesively bonded cases.

1. As adhesive thickness increases, the stresses at the critical points A_1 and B_2 universally increase. Therefore, one should minimize the thickness of the adhesive used in single-lap joint design.
2. Inspecting both varied Young's Modulus and adherend thickness with an adhesive bond, one sees that stresses at point A_1 increase with an increase in each parameter, and the stresses at point B_2 decrease with an increase in each parameter. Therefore, in order to keep stresses optimal, it is hypothesized that one should keep the product of Young's Modulus and adherend thickness, more specifically the flexural rigidity, constant across adherends.
3. Concerning adhesive Young's Modulus, as far as adherend stress is concerned, one should minimize the adhesive Young's Modulus, as the stresses at both critical points increased with increasing adhesive Young's Modulus. However, in design, one must also consider the strength of the adhesive.

4. As bonding length increased, the stresses at both critical points decreased. Therefore, it is recommended that one maximizes the bonding length of single-lap joints within reason.
5. Concerning free adherend length, one should keep it constant across adherends. The stress in the longer adherend was always found to be greater than that in the shorter adherend.

6 Experimental Validation

Using an Instron 1321 tensile testing machine and load cells capable of measuring plus or minus 100 kN load, two single-lap joint specimens were constructed of 6061 Aluminum and FM-94 adhesive. One adherend was approximately twice the thickness of the other adherend, as detailed in the measurements presented later. Due to the limited space in the grips of the testing machine, some material was removed from the thicker adherend, resulting in an exacerbated lateral deformation, also discussed later.

Digital Image Correlation (DIC) was used in order to track the full-field displacement of the bonded region throughout tensile testing. A random black and white speckle pattern was painted onto the bonding region which is used to track the movement of assigned squares. The DIC software does this by assigning greyscale values to smaller regions that the software discretizes the area of interest into. Each square contains a specified number of pixels, and the greyscale values assigned to those pixels generates a unique pattern that can be recognized and tracked by the Dantec software from image to image, allowing for the generation of displacement data.

Figure 6.1 diagrams the approximate shape of the adherends, with letters assigned to each side length and dimension in order to tabulate the dimensions of the two specimens in Tables 6.1 and 6.2.

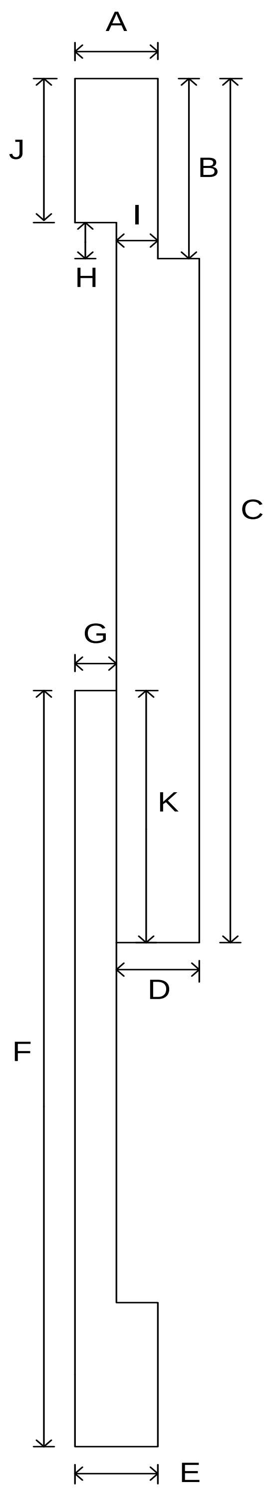

Figure 6.1 Diagram of the dimensions and shapes of the experimental specimens

Table 6.1 Dimensions of specimen 1

A	7.65 mm
B	35.00 mm
C	157.00 mm
D	6.46 mm
E	7.68 mm
F	151.66 mm
G	3.24 mm
H	11.00 mm
I	3.04 mm
J	26.00 mm
K	38.21 mm

Table 6.2 Dimensions of specimen 2

A	7.80 mm
B	28.60 mm
C	151.54 mm
D	6.37 mm
E	7.94 mm
F	147.80 mm
G	3.23 mm
H	2.77 mm
I	3.22 mm
J	25.83 mm
K	38.76 mm

Dimensions were measured to the best estimate possible, but some dimensions, like the adhesive thickness, were so thin that incredible accuracy was impossible. For both specimens, the best estimate possible was 0.003 mm. Several points were compared in Y direction and X direction displacement for each specimen. These comparisons were made at step 120 in DIC recording, with each step equating to 0.5 seconds. In the process of the DIC software discretizing the area of interest, the outter edges of the area are cut off. In order to account for this, points were chosen in reference to the adhesive, which is easy enough to see in the DIC images. In the end, a decent correlation between DIC results and finite element analysis results was possible.

Ideal bonding between adhesive and adherend was assumed, as well as 100% density of both adherend and adhesive. Perfect square edges were also assumed, as well as a perfect square termination of the adhesive. The same 40 element per thickness as verified in previous sections was used, with biquadrilateral quadratic isoparametric plane strain elements, with a measured thickness of 25.55 mm prescribed as the plane strain thickness. The specimen was simulated vertically, as it was placed in the testing machine. Upon inspection of the tested specimens, it was clear that the grips only gripped a portion of the end tabs of the adherends. Therefore, an assumption of 80% tab length was made, and on this length, the movement of the adherends was restricted to vertical movement only. The top adherend's top most corners were pinned. Finally, a central concentrated load, measured by the testing machine's load cell at step 120 was applied to the center of the lower adherend's bottom most face. A linear material model was used, but non-linear geometry was taken into account.

Readily available material data states that the Young's Modulus and Poisson's Ratio of 6061 Aluminum are 68.9 GPa and 0.33, respectively. There is very limited data available concerning the material properties of FM-94 adhesive, but [1] states that the Young's Modulus and Poisson's Ratio of FM-94 are 1.9 GPa and 0.52, respectively. Both materials were treated as elastic.

Curiously, preliminary results showed similar displacement in the Y direction, but were off in the X direction. The only logical conclusion, was that the testing machine's grips were not perfectly centered. The DIC results made this apparent, by the location of a low displacement semi-circle in the displacement magnitude contour plots. Therefore, a lateral shift of 0.35 mm was applied to the bottom grip's simulated boundary conditions. When a lateral displacement was prescribed to the simulated lower grip, the results were much closer to those of the DIC.

Because DIC outputs displacement, X and Y direction displacements were compared for each specimen, at the points detailed in Figure 5.17, the thicker adherend's points denoted by subscript 1, and the thinner adherend's points denoted by subscript 2. Table 6.3 displays the displacement values for specimen 1, and Table 6.4 displays the displacement values for specimen 2. Figures 6.2, 6.3, and 6.4 display the specimen 1 finite element and DIC contours for displacement magnitude, X displacement, and Y displacement respectively. Figures 6.5, 6.6, and 6.7 display the specimen 2 finite element and DIC contours for displacement magnitude, X displacement, and Y displacement respectively.

Table 6.3 Comparison of displacements for specimen 1

	$U_{x,FEA}$ ($U_{x,DIC}$) (mm)	$U_{y,FEA}$ ($U_{y,DIC}$) (mm)	U_x Error	U_y Error
A_1	-0.181 (-0.196)	-0.255 (-0.320)	7.65%	20.31%
B_1	0.811 (1.020)	-0.287 (-0.339)	20.49%	21.53%
A_2	-0.182 (-0.193)	-0.266 (-0.335)	5.70%	20.60%
B_2	0.811 (1.020)	-0.299 (-0.358)	20.49%	16.48%

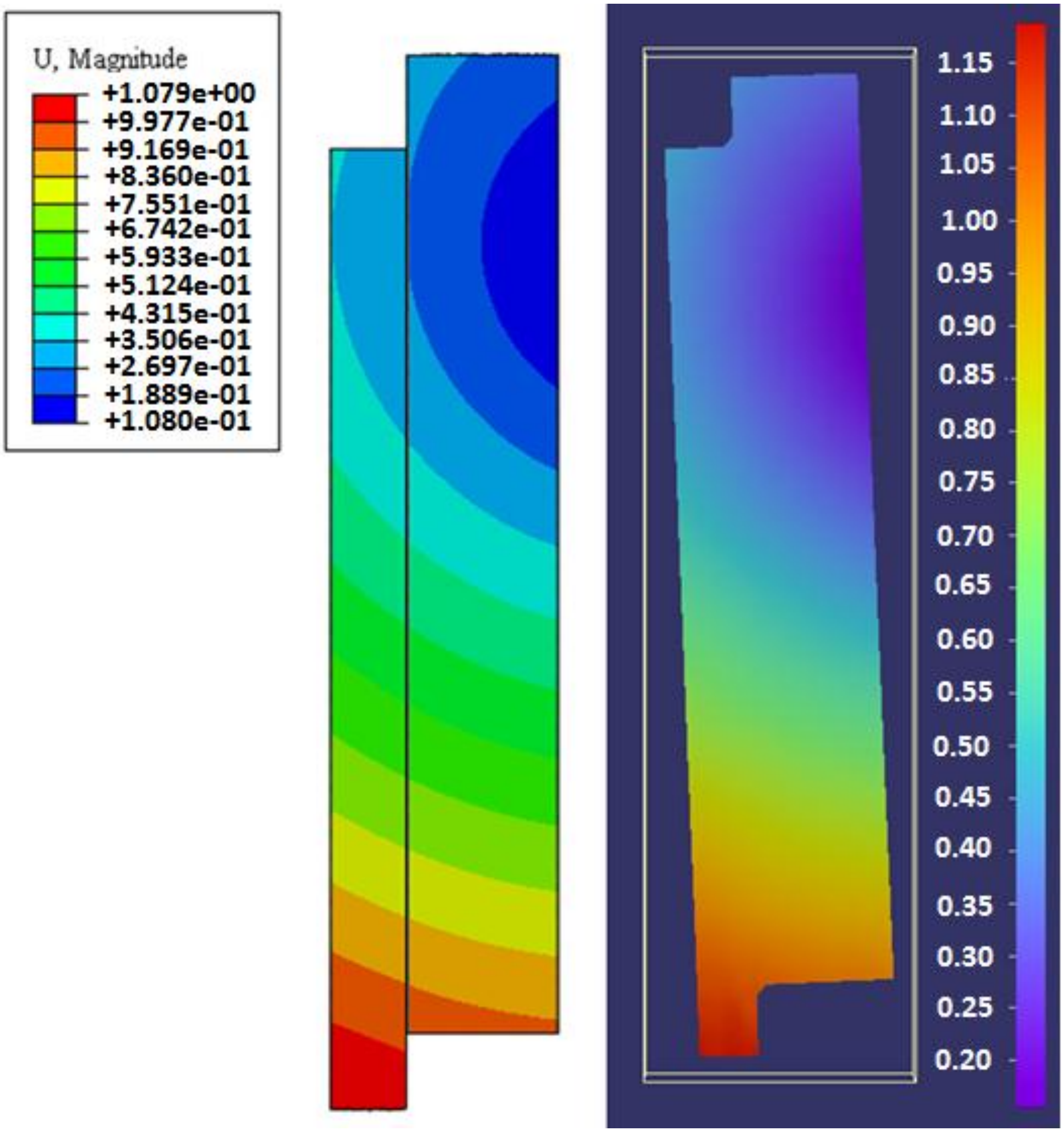

Figure 6.2 Finite element (left) and DIC (right) displacement magnitude specimen 1

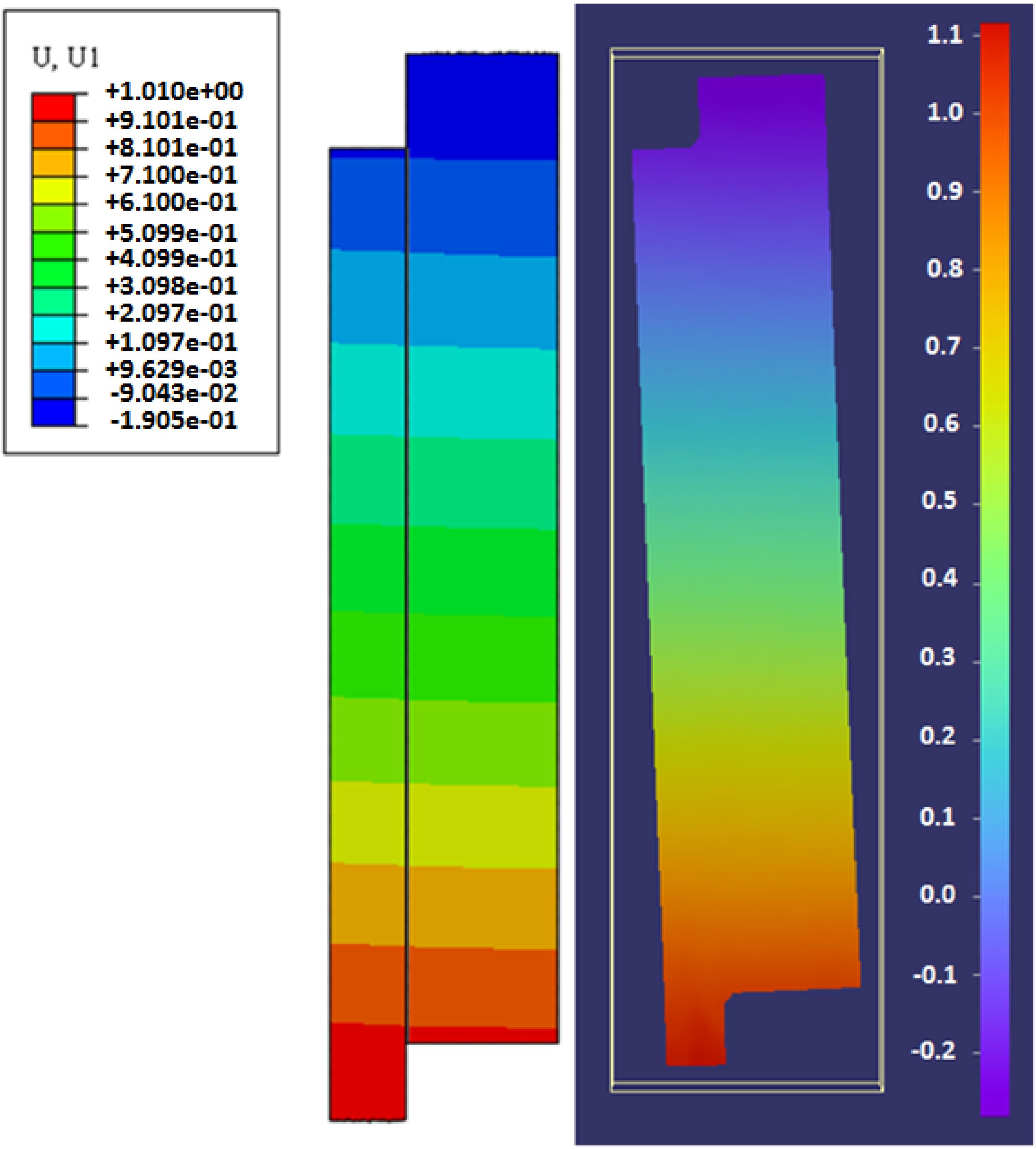

Figure 6.3 Finite element (left) and DIC (right) X direction displacement specimen 1

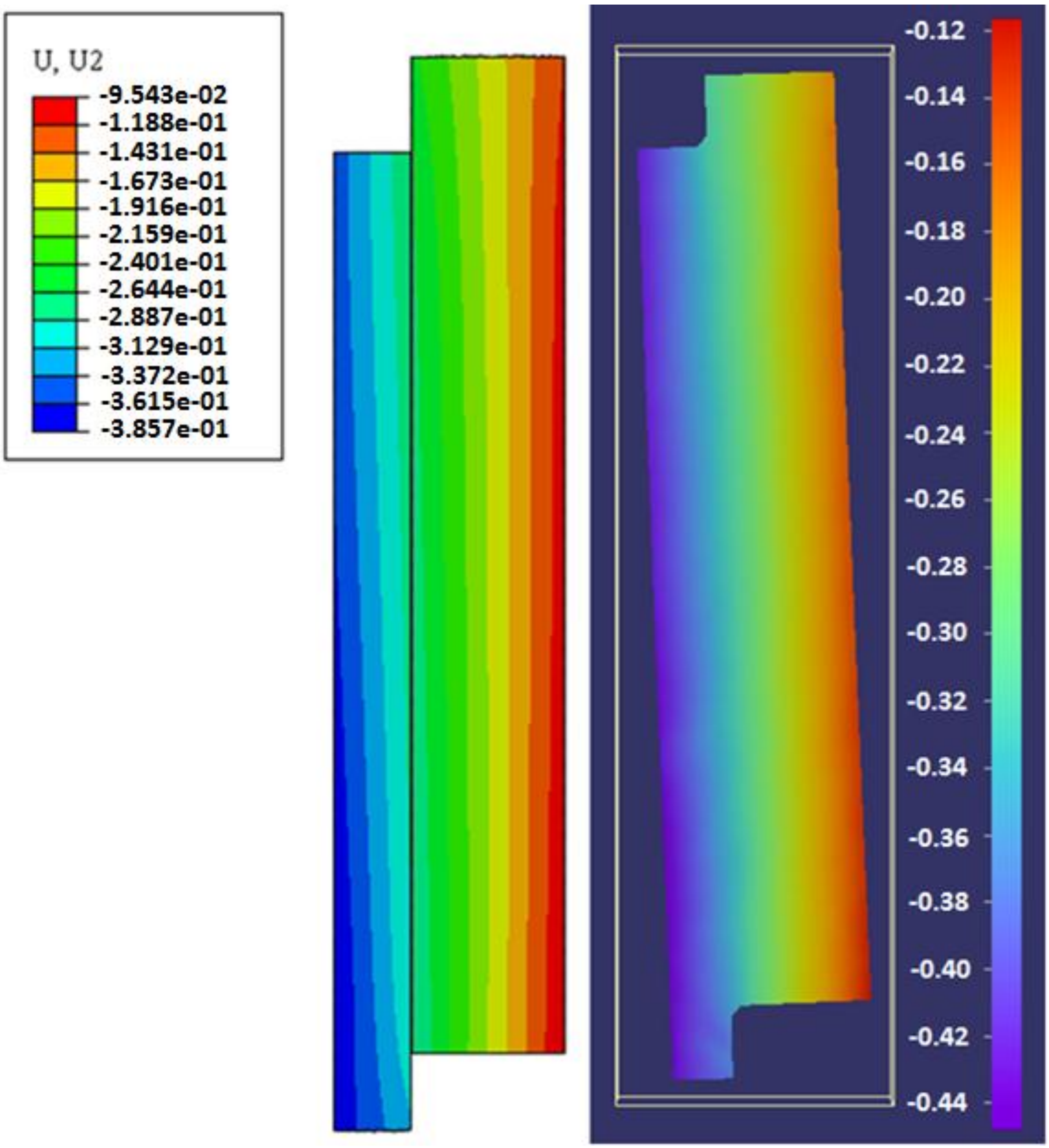

Figure 6.4 Finite element (left) and DIC (right) Y direction displacement specimen 1

Table 6.4 Comparison of displacements for specimen 2

	$U_{x,FEA}$ ($U_{x,DIC}$) (mm)	$U_{y,FEA}$ ($U_{y,DIC}$) (mm)	U_x Error	U_y Error
A_1	0.155 (0.192)	-0.252 (-0.319)	19.27%	21.00%
B_1	-0.842 (-0.964)	-0.286 (-0.466)	12.66%	38.63%
A_2	0.156 (0.194)	-0.263 (-0.339)	19.59%	22.42%
B_2	-0.842 (-0.964)	-0.299 (-0.481)	12.66%	37.84%

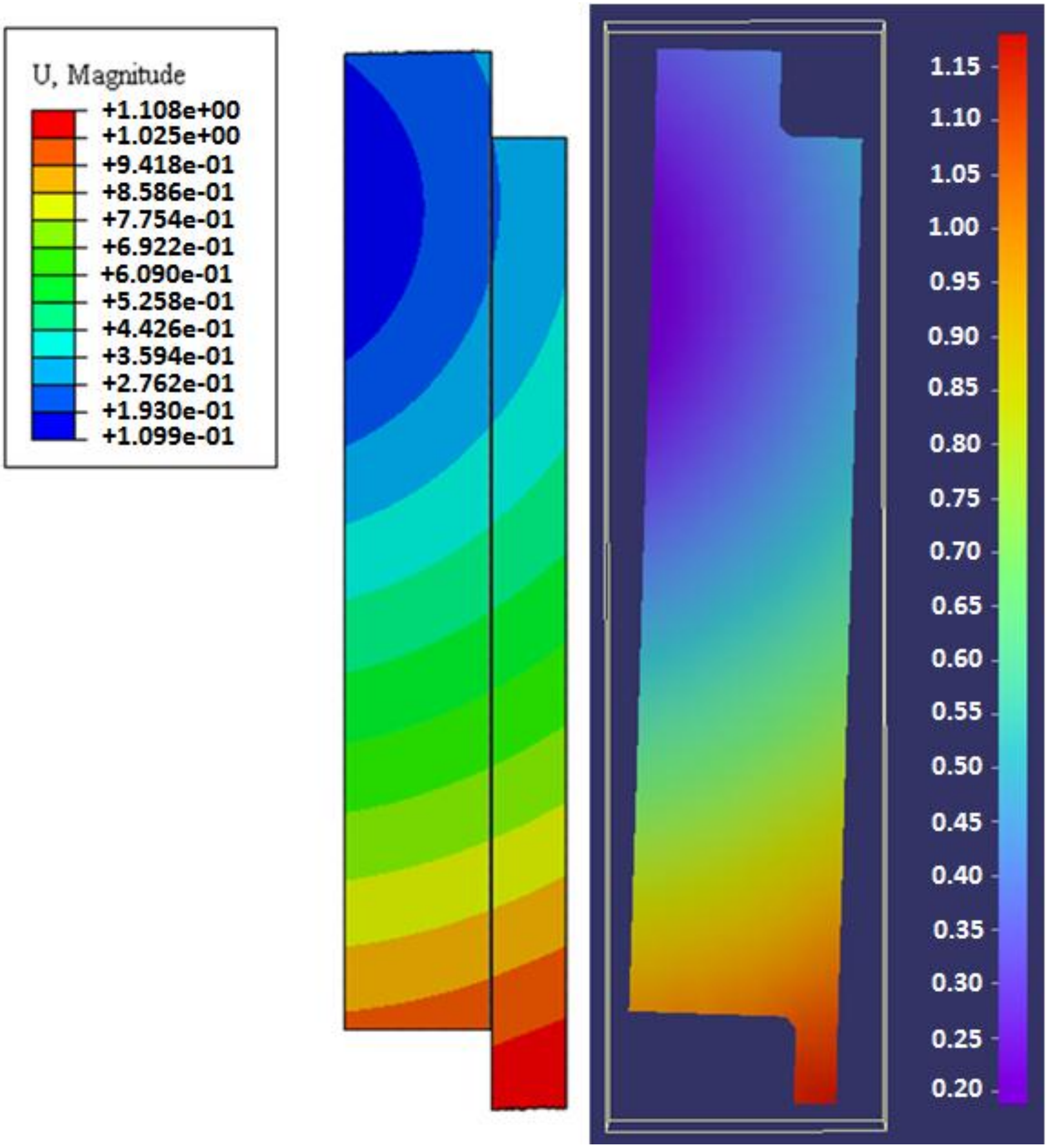

Figure 6.5 Finite element (left) and DIC (right) displacement magnitude specimen 2

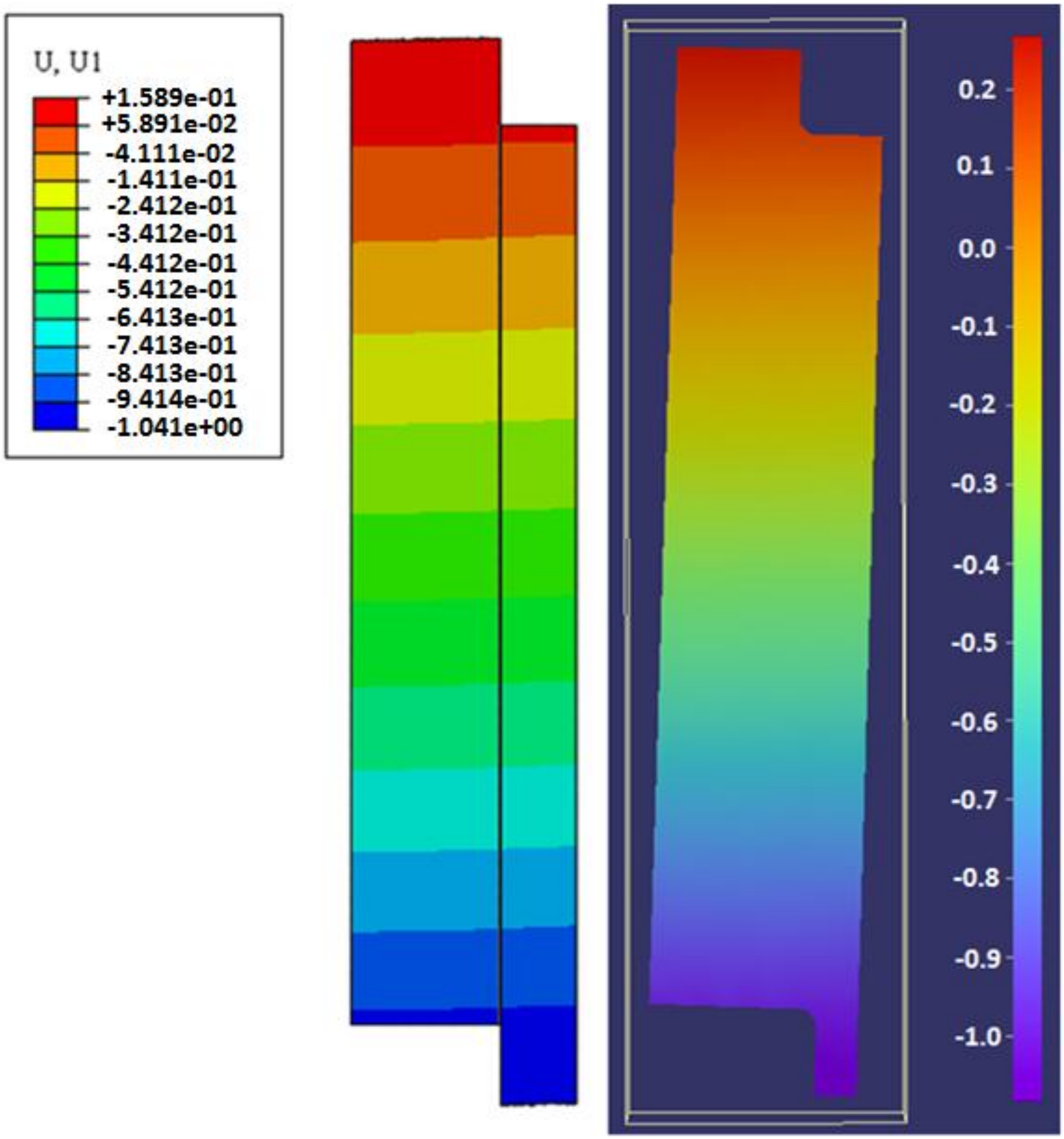

Figure 6.6 Finite element (left) and DIC (right) X direction displacement specimen 2

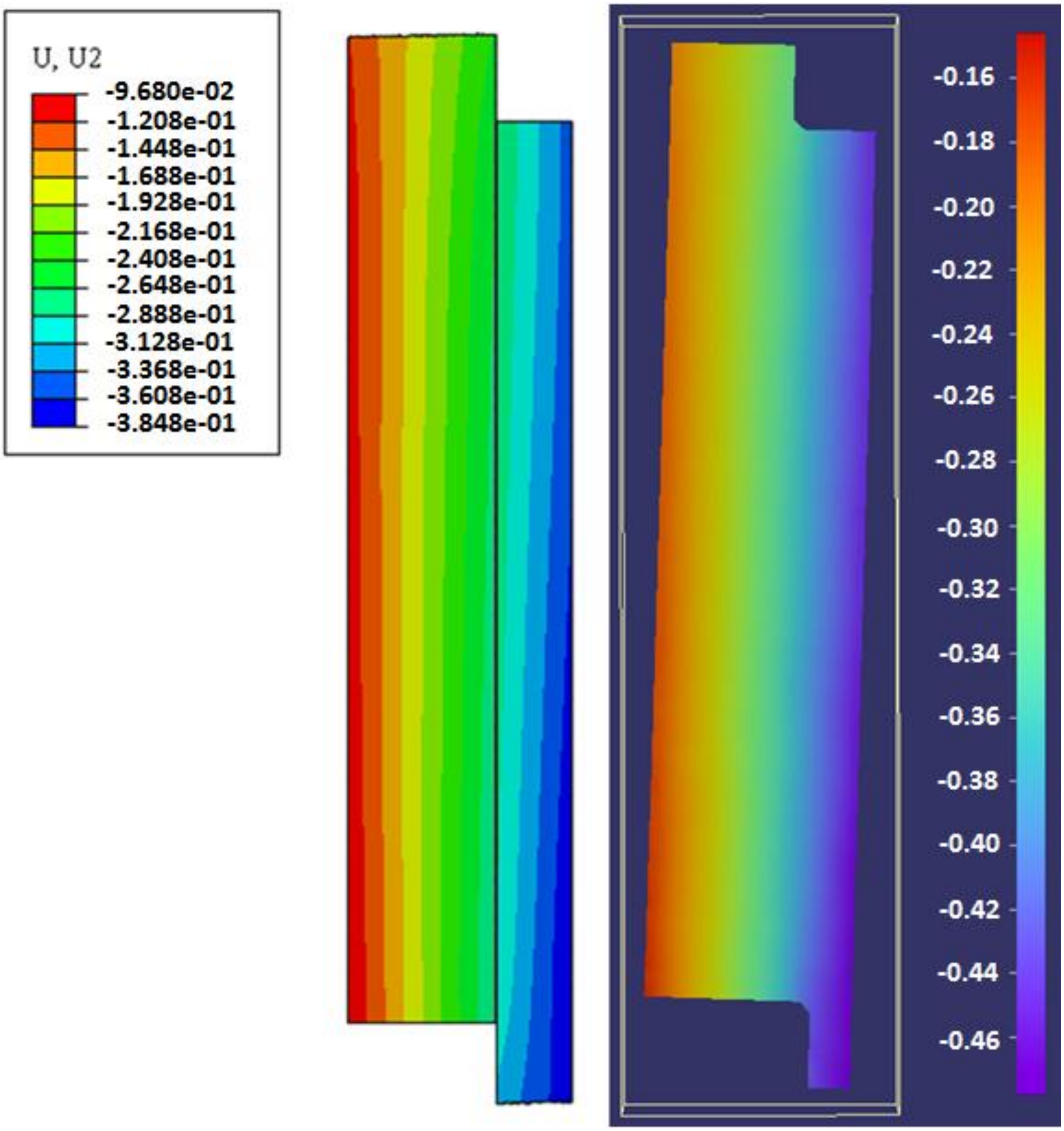

Figure 6.7 Finite element (left) and DIC (right) Y direction displacement specimen 2

As can be seen, under the assumptions made for the finite element models, the quantitative error between finite element and DIC results was about 20% for each specimen, and qualitatively, the colormaps correlated fairly well. However, in specimen 2's case, there were two points near 40% error. The same points, under similar load and identical assumptions, in specimen 1, had an error of about 20%. Looking more at the actual displacement values, the error is often less than 15 tenths of a millimeter. In the case of the two largest percent errors, the difference is about 19 tenths of a millimeter.

These errors can be attributed to a variety of factors. The limited data on FM-94 adhesive leaves the possibility of less than completely accurate material model. The assumption of linear material behavior may be a contributing factor as well, but without time and more samples, a nonlinear material model could not be obtained. In the case of the largest percent errors, under similar loading, the finite element results were similar, but the DIC results were significantly different. This leads one to believe the results obtained for Y direction displacement obtained by DIC may have been affected other factors. For example, the grips may have applied uneven pressure, the adhesive may have been less than 100% dense, or the specimen may have slipped in the grip. A multitude of factors in the experimental setup could have affected the DIC results, and testing more specimens under higher levels of observation would shed light on this. A 100% density assumption on the adhesive, along with the ideal bonding could also slightly effect the results.

DIC also grants some insight into the initiation of specimen failure. Applying the loads associated with specimen failure, 22 kN for specimen 1 and 21.7 kN for specimen 2, the values in Tables 6.4 and 6.5 were obtained at the critical points identified in the parametric studies conducted on adhesively bonded single-lap joints in chapter 5.

Table 6.5 Failure stress predictions for specimen 1

	σ_{vm} (MPa)	σ_{xx} (MPa)	σ_{yy} (MPa)	τ_{xy} (MPa)
A_1	599.143	319.029	711.610	-116.803
B_2	758.960	369.960	916.931	-126.375

Table 6.6 Failure stress predictions for specimen 2

	σ_{vm} (MPa)	σ_{xx} (MPa)	σ_{yy} (MPa)	τ_{xy} (MPa)
A_1	606.161	372.254	723.762	117.287
B_2	792.588	326.845	939.834	130.468

As can be seen, under similar but slightly different geometry and loading, the stresses measured are very similar at each point, with less than 10% difference in all stresses. While reading the DIC images for failure initiation is not obvious or easy, a relatively close estimate can be made, and the failure loads calculated for specimen are very similar. If one were to obtain the failure stress of FM-94 adhesive, the material that fails first during tensile testing with aluminum adherends, and find that this failure stress was close to 900 MPa, one could verify that this simulation in fact accurately simulates the specimen and can be used to predict failure in other simulated specimens.

REFERENCES

REFERENCES

[1] X. Zhang et. al. "Fail-safe design of integral metallic aircraft structures reinforced by bonded crack retarders." *Engineering Fracture Mechanics.* 76. (2009)

7 Conclusions

For each of the following conclusions, the reader is referred to the figures in chapter 5 for the location of the critical points referenced.

1. Varied adherend Young's Modulus, in both ideally bonded and adhesively bonded single-lap joints with a tensile load applied, yielded increasing stress values as Young's Modulus increased at point *A*, and decreasing stress values as Young's Modulus increased at point *B*, except in reference to Y direction stress. Ratios anything different than unity resulted in reduced Y direction stress as one adherend was always stiffer than the other, and this caused the usual central bond rotation to be translated into axial deformation of the less stiff adherend.

2. Varied adherend thickness, in both ideally bonded and adhesively bonded single-lap joints with a tensile load, yielded varied stress values that increased with increasing adherend thickness at point *A*, and stress values that decreased with increasing adherend thickness at point *B*. While variations in adherend thickness varied stiffness in this case as well as the case of varied Young's Modulus, the eccentricity of the load and moment of inertia of the varied adherend were also affected. This caused Y direction stresses to follow the same trends as the other measured stresses, rather than following the phenomena resulting from the varied Young's Modulus case.

3. Free adherend length variation yielded different results than varied thickness or Young's Modulus. With increasing free adherend length, the stresses decreased in

intensity at point *A* and increased in intensity at point *B*. Its variation greatly affects the eccentric loading angle for ratios less than unity, and affect it less and less as ratios increase up past unity, which greatly affects stresses for the former, and less so for the latter, a phenomena that was observable by increasing or decreasing slope in the SCF plots.

4. Varied bonding length exhibited the expected behavior for ratios greater than unity; the stresses at both critical points decreased as the ratio increased. For ratios much less than unity, the stresses at each point began to affect the stresses at the other point, resulting in seemingly strange results in the stresses. For ratios greater than unity, there was a uniform decrease in all measured stresses as bonding length increased.

5. Varied adherend Young's Modulus and bonding length under a three point bending load exhibited the same behavior as under a tensile load. This is to be expected; increasing Young's Modulus yielded an increasing adherend stiffness, and increasing bonding length increased the moment of inertia and general thickness of the member near the application of the bending load, resulting in the same universal reduction in stress intensity observed in the tensile loading case.

6. Varied adherend thickness under a three-point bending load produced much the same results that varied bonding length produces; stresses decrease at both points under increased thickness because there is a greater cross-sectional area and moment of inertia as a result of this increased thickness. The variation in the right hand boundary

condition's location could cause the increasing compressive intensity, rather than tensile intensity, for ratios less than unity at point *A*.

7. Free adherend length variation under a three-point bending load behaved much as was expected; increasing length increases the lateral moment arm of the applied force, and therefore universally increases the stresses at both critical points.

8. The addition of an adhesive over the ideally bonded cases had one most notable effect; it made the stresses at the point formerly designated *B* the most intense, and made those at point *A* small to the point of unimportance.

9. As adhesive thickness increases, the stresses at both critical points increases. This is to be expected, as it increases the eccentricity of load, and therefore the dominant force on the central bonding region of the single-lap joint.

10. Increasing adhesive Young's Modulus increases the stresses at both critical points, as the adhesive increases in stiffness, deforms less, and forces more deformation and stress on the adherends.

11. Using a linear material model and nonlinear geometry, along with approximate but near accurate measurements and boundary condition mimicry and a verified mesh density, one can predict the deformation of a single-lap joint in a tensile test with an

average of 20% error. This error can be reduced by a more accurate material model, more accurate measurements, more accurate testing comparison, and a more ideal testing setup.

12. As one can simulate deformation of an experimental single-lap joint, they can also predict the failure stress with a finite element model reasonable accurately. With accurate indications as to the initiation of adhesive failure and more accurate testing, one can improve the accuracy of this prediction.

8 Suggestions for Future Research

1. In order to more deeply understand the affect varied material and geometric parameters have on the critical points' stresses, one vary more than one parameter at once, to understand how each parameter interacts with the other.

2. One could also more deeply understand single-lap joints if they were to study exceedingly long and exceedingly short lap joints, rather than the joints of intermediate length studied in this thesis.

3. In order to increase the accuracy of the experimental finite element model, one can do several things:
    a. Develop a more accurate strain-dependent material model for both the adherend material and adhesive material.
    b. Take steps to assure that the testing grips apply equal pressure to each clamped region and that they are as perfectly aligned as possible.
    c. Assure that the DIC setup is not disturbed during the experiment's duration, and assure that the camera used is as perfectly aligned as possible.
    d. Ensure that all dimensional measurements are as accurate as possible, and that any machining that is needed is as accurate as possible, and that the gripped regions can be perfectly aligned vertically.